ANALYSIS OF LEAN PREMIXED TURBULENT COMBUSTION USING COHERENT ANTI-STOKES RAMAN SPECTROSCOPY TEMPERATURE MEASUREMENTS

by

Daniel V. Flores

A dissertation submitted to the faculty of

Brigham Young University

In partial fulfillment of the requirements for the degree of

Doctor of Philosophy

Department of Chemical Engineering

Brigham Young University

April 2003

BRIGHAM YOUNG UNIVERSITY

GRADUATE COMMITTEE APPROVAL

Of a dissertation submitted by

Daniel V. Flores

This dissertation has been read by each member of the following graduate committee and by a majority vote has been found satisfactory.

_____	_____
Date	Thomas H. Fletcher, Chair
_____	_____
Date	Paul O. Hedman
_____	_____
Date	Merrill W. Beckstead
_____	_____
Date	William G. Pitt
_____	_____
Date	Kenneth A. Solen

BRIGHAM YOUNG UNIVERSITY

As chair of the candidate's graduate committee, I have read the dissertation of Daniel V. Flores in its final form and have found that (1) its format, citations, and bibliographical style are consistent and acceptable and fulfill university requirements; (2) its illustrative materials including figures, tables, and charts are in place; and (3) the final manuscript is satisfactory to the graduate committee and is ready for submission to the university library.

_____ _____

Date

Thomas H. Fletcher
Chair, Graduate Committee

Accepted for the Department

_____

William G. Pitt
Graduate Coordinator

Accepted for the College

_____

Douglas M. Chabries
Dean, College of Engineering and Technology

ABSTRACT

ANALYSIS OF LEAN PREMIXED TURBULENT COMBUSTION USING COHERENT ANTI-STOKES RAMAN SPECTROSCOPY TEMPERATURE MEASUREMENTS

Daniel V. Flores

Department of Chemical Engineering

Doctor of Philosophy

An existing CARS instrument was modified to use a new dual dye laser that produces simultaneously CARS spectra of N_2, CO, CO_2 and O_2. These CARS spectra yield simultaneous values for the gas temperature from N_2 and concentrations of CO, CO_2 and O_2. The dual-dye laser was generated using a mixture of pyromethene 650 and 597 dyes (both commercially available) dissolved in ethanol. Calibration studies in a tube furnace showed that the modified CARS instrument using the dual dye laser has good accuracy and acceptable precision for gas temperature measurements. However, the modified instrument had limited capabilities in measuring the concentrations of O_2 and CO_2 in the concentration ranges of interest, possibly due to the approximations involved in the CARS reduction algorithm used in this work.

The modified CARS instrument was successfully applied to obtain detailed measurements of instantaneous gas temperature for four lean premixed combustion

conditions, with varying inlet stoichiometry and swirl level, in a Laboratory Scale Gas Turbine Combustor (LSGTC). The temperature data were used to produce iso-contour plots of averaged and normalized standard deviations. Probability Density Function (PDF) plots were also produced at several measurement locations.

Additional insights regarding the flame behavior were obtained by examining the spatial variation in the shape of the PDFs for all the combustion conditions. Several zones were identified in all four cases where the nature of the PDFs seems to be determined by different factors. At lower heights, near the bottom of the combustor, the swirl level seems to be the predominant factor determining the nature of the turbulent fluctuations, whereas near the wall and around z = 50 mm, the equivalence ratio appears to predominate. For the rest of the flame, the combined effect of the equivalence ratio and swirl level seems to determine the nature of the temperature fluctuations.

A preliminary analysis of combined LDA, PLIF and CARS data was presented for the most stable combustion case. The combined analysis made it possible to identify a potential zone of ignition, started by the mixing with the hot gases from both the central and the side recirculation zones.

Analysis of the gas temperature data has revealed new insights into the complex nature of the mixing and reaction processes that take place in lean premixed swirling flames. Comparison with LDA velocities and PLIF OH images suggests that the side recirculation zone may play an important role in the stabilization of the flame, along with the central recirculation zone. In addition, a flow reversal observed in the velocity components suggests the existence of eddies throughout the flame.

For my dad Para mi papá

José Flores A.
1940 - 2002

ACKNOWLEDGEMENTS

I feel deeply indebted to many people, first, to my beloved wife, Susan, and our children who put up with many a "well, I need to go work on my dissertation" from me. Equally as important I am indebted to my dad, whose vision, courage, and encouragement made this possible: gracias papá. Then there is a long list of other good people: Dr. Fletcher and Dr. Hedman for their PATIENCE and guidance; Ken Foster in the machine shop for making himself and his shop available for me to fix broken parts and make others as I needed them; and Stewart Graham and Wayne Timothy, two undergraduate students, for their valuable assistance. Finally, I also thank the Department of Chemical Engineering, the College of Engineering and Technology, and Brigham Young University for providing excellent professors, research assistantships, and scholarships.

TABLE OF CONTENTS

LIST OF FIGURES

LIST OF TABLES

NOMENCLATURE

Acronyms

CARS	Coherent Anti-Stokes Raman Spectroscopy
CRZ	Central Recirculation Zone
FWHM	"Full Width at Half Maximum", i.e., the total width of the line shape at half the value of the maximum intensity
IPDA	Intensified Photo-Diode Array
LDA	Laser Doppler Anemometry
LSGTC	Laboratory-Scale Gas Turbine Combustor
PDF	Probability Density Function
PLIF	Planar Laser Induced Fluorescence
SRZ	Side Recirculation Zone

Symbols and Variables

D	diameter of a beam prior to focusing on the diagnostic volume
d	LSGTC swirl block nozzle diameter
d_h	LSGTC swirl block vane hub diameter
d_s	CARS sampling volume diameter
f_l	focal length of the focusing lens
f, g	convolution functions of the resonant components of $c_{CARS,\ theory}$
HS65	Combustion case of High Swirl ϕ = 0.65
HS80	Combustion case of High Swirl ϕ = 0.80
I	background-free intensity values of a single-shot CARS sample corrected for image persistence from the previous sample
I_{bg}	averaged sample of background noise across the wavelength range of the IPDA

I_{bgFree}	background-free spectral curve
$I_{bgFree,Prev}$	background-free intensity values of the previous single-shot CARS sample
I_{CARS}	estimated actual CARS spectrum
I_{dye}	intensity of the dye laser as a function of wavelength, theoretical
$I_{dyeProfile}$	intensity of the dye laser as a function of wavelength, measured
I_{pump}	intensity of the pump laser
I_{raw}	spectra recorded by the BYU single-Stokes CARS instrument
Iw	light intensity at the frequency w at either side of w_0
Iw_0	light intensity at the actual frequency w_0
ImaPer	residual intensity in a CARS sample due to image persistence from the previous sample
L	CARS sampling volume length
NonLin	the non-linearity of the IPDA used in this work
MS65	Combustion case of Medium Swirl $\phi = 0.65$
MS80	Combustion case of Medium Swirl $\phi = 0.80$
P_i	ith pixel in the IPDA
SN	Swirl Number, the ratio of the tangential momentum to the axial momentum
x_i	mole fractions of the ith species (e.g., N_2, O_2 or CO_2) in the CARS sample mixture
r	radial distance measured from the centerline of the LSGTC
z	vertical height measured from the bottom of the LSGTC chamber
c_{CARS}	experimental CARS susceptibility obtained from I_{CARS}
$c_{CARS,\ theory}$	theoretical CARS susceptibility, fitted to its experimental counterpart c_{CARS}
c_{NR}	total nonresonant susceptibility component of $c_{CARS,\ theory}$
Δw_l	Lorentzian FWHM for the approximated Voigt function, in cm^{-1}.
Δw_R	Raman Shift of a molecular transition
$\Delta w_{R,i}$	Raman Shift in cm^{-1} at the ith pixel

Δw_v	Voigt FWHM for the approximated Voigt function, in cm^{-1}.
ϕ	Fuel equivalence ratio
l	light wavelength
l_i	wavelength of the light reaching the ith IPDA pixel
θ	LSGTC swirl block vane angle measured from the vertical axis
w_1	pump beam frequency
w_2	dye beam frequency
w_3	CARS signal frequency

1. INTRODUCTION

1.1 Background

During the past few years, turbine systems operating on natural gas have been considered as a viable alternative to produce electricity, which is greatly needed by our society. Turbine systems may operate using a wide variety of fuels; however, the large amounts of natural gas available and its relatively clean combustion characteristics make it an attractive fuel as a source of energy (Ecob, et al., 1996; Hay, 1985).

In an effort to improve the technology of gas turbine systems, the U. S. Department of Energy started the Advanced Turbine Systems (ATS) program. The ATS program has the objective of developing and commercializing land-based gas turbine systems that are 1) highly efficient, 2) environmentally superior, and 3) cost competitive. Because of the complexity of the task, several industrial and educational institutions are involved in the ATS program doing research in different key aspects of the performance of gas turbine systems. One of those key aspects is the combustion in the gas turbine, which largely determines both the efficiency and the pollutant emissions of the engine.

An ATS contract (Hedman, et al., 1998) to develop a computer code for modeling combustion in gas turbine systems was granted to the Advanced Combustion Engineering Center (ACERC) at Brigham Young University (BYU). The primary focus of the ATS research at ACERC was the simulation of the turbulent combustion of natural gas premixed with air in gas turbines. However, the ATS research at ACERC also included a

comprehensive experimental program dedicated to the acquisition of reliable experimental data to help in 1) understanding the combustion process in conditions relevant to advanced gas turbine systems; and 2) validating the computer simulations.

This work is one in a series of laser-diagnostics experiments performed as part of the ATS research at ACERC. The other two parts of the study consist of (a) gas velocity measurements (Hedman, et al., 2002b; Murray, 1998), and (b) OH radical imaging (Hedman, et al., 2002a), both obtained using laser diagnostics techniques.

1.2 Objectives

This work had three main objectives. The first objective was the development of a novel variation of a laser diagnostics instrument. The second objective was to apply the new instrumentation to obtain instantaneous gas temperature measurements in a burner configuration relevant to practical gas turbine combustors. The third objective was to use the temperature data to examine the effects of swirl and stoichiometry on the premixed combustion within the fuel-lean range.

It is expected that the data obtained in this work, together with the other two parts of the ATS study, will lead to a better understanding of the complex interactions between turbulence, chemical kinetics, heat transfer, and flow dynamics during lean premixed turbulent combustion. The data will also serve as a benchmark, aiding combustion modelers in the development and evaluation of comprehensive computer models.

1.3 Approach

The combustion of premixed natural gas with air was investigated at four different conditions of stoichiometry and inlet swirl. The experiments were performed in the

Laboratory Scale Gas Turbine Combustor (LSGTC) located in the optics laboratory at BYU. The LSGTC simulates many of the combustion characteristics of industrial gas turbine combustors while providing appropriate optical access for laser diagnostics techniques.

In this work, measurements were carried out using Coherent Anti-Stokes Raman Spectroscopy (CARS), a non-intrusive laser based technique. The CARS instrument developed in this work was based on previous research on a dye laser reported by Haslam and Hedman (1996) that allows simultaneous CARS measurements of N_2, CO, CO_2, and O_2 spectra. These CARS spectra yield simultaneous values for the gas temperature and concentrations of CO, CO_2, and O_2.

Furthermore, a brief comparison of the CARS temperature data with velocity data (Hedman, et al., 2002b; Murray, 1998) and OH data (Hedman, et al., 2002a) was performed. Some interesting insights were gained from this comparison leading to some suggestions for further research.

2. LITERATURE REVIEW

2.1 Combustion Issues in Gas Turbines

The basic operation of gas turbine systems (see Figure 2.1) can be described as follows (Lefebvre, 1983): 1) atmospheric air is compressed to high pressures; 2) practical gas turbine systems mix the high-pressure air and the fuel prior to combustion; 3) the premixed fuel/air mixture is then injected into the combustion chamber at high swirling velocities; 4) the hot gases produced in the burner are then carried into the turbine blades that convert the thermal energy to shaft work, which can be used to generate electricity.

The combustion chamber is a critical component of a gas turbine system since it determines the emission levels of pollutants and plays a determinant role on overall efficiency and turbine durability. Thus, it is important to understand the impact of the combustion process on burner configurations relevant to gas turbine systems.

The gas turbine combustion chamber must be designed to comply with several operational criteria. These criteria arise because of requirements relative to structural stability of the turbine, existing environmental regulations, and overall efficiency of the gas turbine system.

The main design criteria for burner design may be summarized as follows (Cohen, et al., 1996; Melvin, 1988): 1) the temperature of the exit stream gases must be sufficiently low to keep stress on turbine components within specifications; 2) the temperature

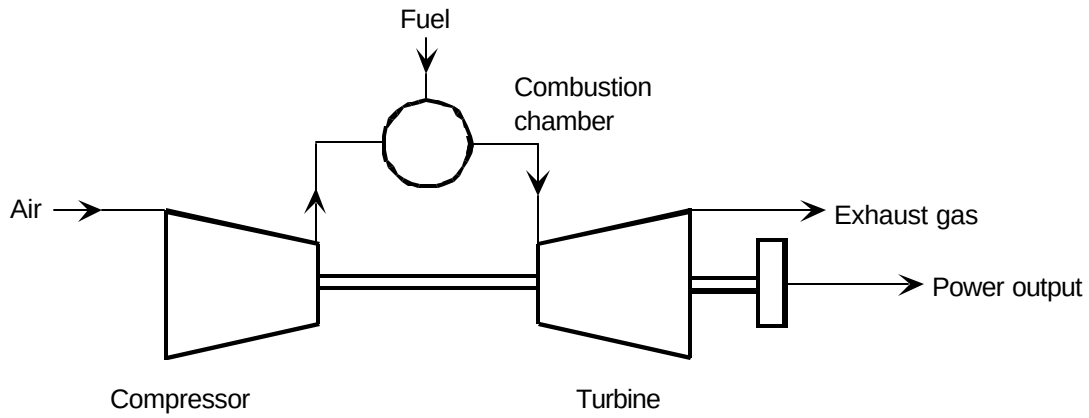

Figure 2.1. Simplified schematic of a gas turbine system.

distribution of the exit stream gases must be known to avoid local overheating on turbine blades; 3) stable combustion must be maintained at high air velocities (30-60 m/s) and over the range of air/fuel ratios that the combustor will experience between full load and idling conditions; 4) the production of soot must be avoided because of particulate emissions restrictions (visual plumes) and the potential of damaging engine components and blocking cool air passages; 5) emission levels of pollutants such as nitrogen oxides (NO_x), carbon monoxide (CO), and unburned hydrocarbons (UHC) must conform to environmental regulations; and 6) high performance and efficiency of the gas turbine system must be maintained.

Designing a burner configuration that offers optimum performance is challenging because conditions favoring one criterion may work against another. For example, increasing the turbine inlet temperature and operating at high pressures increases the efficiency but also increases the production of undesirable NO_x.

Clearly, a good quantitative understanding of turbulent premixed combustion of natural gas and air is required in order to design combustors with optimum performance.

In achieving such understanding, complete experimental studies under conditions relevant to gas turbine systems must be performed. The results of such experimental knowledge can be used to understand fundamental aspects of premixed combustion as well as to validate comprehensive computer codes that will aid in combustor design.

2.2 Laser Diagnostics Techniques

The experimental analysis of clean gaseous flames, such as premixed natural gas flames relevant to gas turbines, can be carried out using a variety of methods. Laser diagnostics techniques are considered the most suitable because they provide a non-intrusive means of analyzing the gas-phase combustion, both spatially and temporally. Existing laser diagnostics techniques allow the measurement of gas velocities, temperatures, and concentrations of chemical species.

Gas velocities can be measured using Laser Doppler Anemometry (LDA), a very well established technique (e.g. Murray, 1998; Schmidt, 1995; Schmidt and Hedman, 1995; Warren and Hedman, 1995; Warren, 1994). LDA is based upon the Mie scattering from particulates crossing a control volume defined at the focusing point of two lasers of the same wavelength (Rudd, 1969; Yeh and Cummins, 1964), usually in the visible range. Because the laser source is generally continuous, the rate of data acquisition depends on the rate that particles cross the control volume. Two components of the velocity field can be obtained simultaneously by focusing two pairs of lasers at the same point, each pair having a different color.

Using the aforementioned two-color technique, Murray (1998) obtained two sets of time-resolved gas velocity measurements on the LSGTC for the same combustion conditions to be investigated in this work. One set of velocity measurements consisted of

simultaneous measurements of axial and radial velocity components whereas the other set was for the axial and tangential velocity components. It must be noted that there are no inherent particles in a premixed natural gas and air system, and, therefore, the flame must be seeded with inert particles that are small enough to follow the flow. A description of the particle type and loading used in the LDA measurements on the LSGTC is given by Murray (1998). This particle seeding may be considered an intrusion to the flow, but its effects on the flow and the combustion are considered minimal because the particles are inert hollow Al_2O_3 spheres with an average diameter of 6 μm.

The most prominent laser spectroscopic techniques for measuring gas temperature and species concentrations (Eckbreth, 1996) are: Rayleigh scattering, Raman scattering, Planar Laser Induced Fluorescence (PLIF), and Coherent Anti-Stokes Raman Spectroscopy (CARS). The first three techniques have the following common features: 1) only one laser is required to generate the signal and 2) they are incoherent in that the signal is scattered in all 4p steradians from each point along the path of the laser, which limits the signal collection to only a fraction of the total. In contrast, CARS requires the use of three lasers to generate a coherent (i.e., laser-like) signal that can be collected in its entirety. CARS is a very well established technique in the study of combustion (Eckbreth, 1996; Tolles, et al., 1977) and is the technique used in this work. Brief descriptions of the other techniques follow. More information on these techniques, and others not mentioned here, may be found elsewhere (Eckbreth, 1996).

Rayleigh scattering results when light quanta interact with molecules in an elastic process, i.e., there is no net energy exchange between the light and the molecules. Thus, the Rayleigh signal has the same frequency as that of the incident light, as shown in

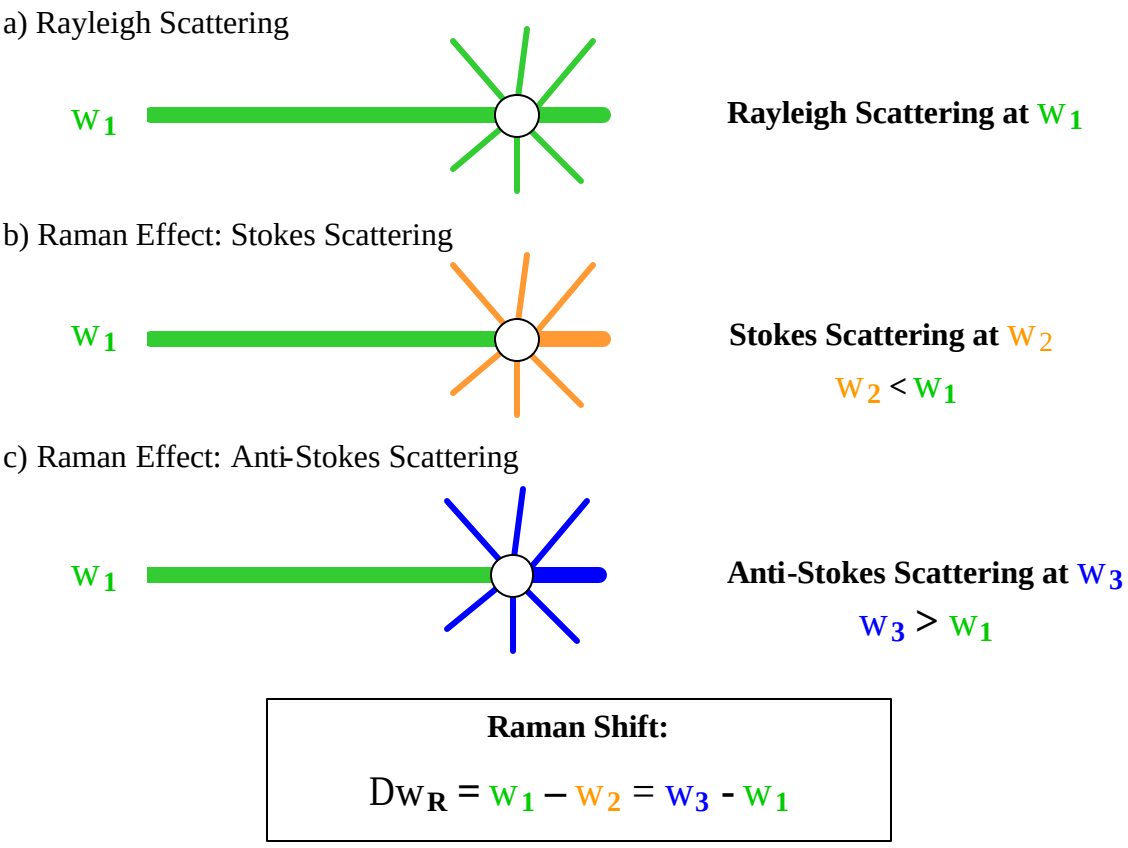

Figure 2.2. Rayleigh and Raman Scattering processes. The circle represents a scattering medium, such as N2 molecules.

Figure 2.2a. Consequently, Rayleigh scattering generally cannot discriminate between chemical species. However, Rayleigh scattering is a powerful tool to determine gas temperatures.

Raman scattering is generated by an inelastic interaction between light quanta and matter. The Raman scattering is called Stokes (see Figure 2.2b) if the signal frequency is less than the frequency of the incident laser. On the other hand, the Raman process is termed anti-Stokes (see Figure 2.2c) if the signal has a greater frequency (i.e., more energy) than the frequency of the incident laser. The net value of the frequency shift $w_1 - w_2$ for Stokes scattering equals the frequency shift $w_3 - w_1$ for anti-Stokes

scattering. This "Raman shift", Δw_R, is a distinctive molecular property and allows the use of Raman scattering to measure temperatures and, in principle, concentrations of any Raman-active species with the use of only one laser. However, Raman scattering is limited in practice by the sensitivity of current detectors because of their low signal-to-noise ratios, which is compounded with the signal being scattered in all directions.

Planar Laser Induced Fluorescence (PLIF) is achieved by exciting the species of interest to a higher electronic state by means of a laser sheet. The excited species then undergoes the process of fluorescence by spontaneously emitting light as it returns to the ground state. Thus, a 2-dimensional image of the species being probed can be collected. PLIF has found great application in the diagnostics of radicals and species whose concentrations are below the 1000 ppm level, where other techniques fail. However, a quantitative interpretation of PLIF images still remains a challenge due to various factors that are beyond the scope of this review (Eckbreth, 1996).

Coherent Anti-Stokes Raman Spectroscopy (CARS) is based on the generation of a Raman induced signal at the anti-stokes frequency of the species being probed. In a sample of molecules of the same species, there are several combinations of rotational and vibrational states, each state having its own CARS signal. This set of CARS signals forms the CARS spectrum, which is specific for a given species and varies with temperature. The CARS signal is generated by aligning three laser beams of appropriate frequencies in any geometrical arrangement that complies with the "phase matching" condition (Eckbreth, 1996).

Figure 2.3 shows the geometrical arrangement commonly known as BOXCARS that is used at the BYU optics laboratory. This arrangement focuses the three beams onto a

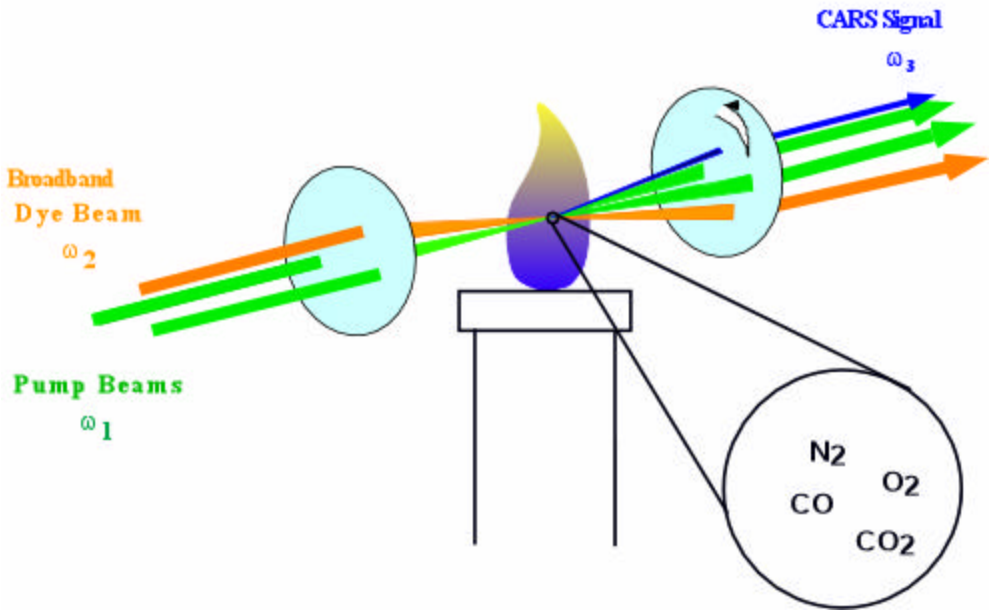

Figure 2.3. BOXCARS configuration to produce a CARS signal

diagnostic volume about 1 mm long and 20 µm in diameter. In general, two of the lasers will be at the same frequency (ω_1); these lasers are commonly called "pump" beams.

The third laser of frequency ω_2 is commonly referred to as the "Stokes" laser because it must be "Stokes-shifted" from frequency ω_1 to generate one of the possible CARS signals of a species. This means that ω_2 must equal the frequency the "pump" beams minus the Raman shift of the species being probed. The CARS signal is then generated at the frequency ω_3, the anti-Stokes Raman transition relative to the pump beams. For time-resolved diagnostics, as in this research, all of the CARS signals (i.e., the CARS spectrum) of each of the species of interest must be obtained simultaneously. This requires the spectral energy distribution of the Stokes beam to cover all the Stokes Raman

transitions of one or more species, which requirement can be achieved by the use of broadband dye lasers.

A more detailed explanation of the theory of CARS is beyond the scope of this dissertation; however, there are several sources available in the literature (Eckbreth, 1996; Druet and Taran, 1981; Eesley, 1981; Tolles and Harvey, 1981; Tolles, et al., 1977; Armstrong, et al., 1962). CARS has been shown to be particularly useful in thermometry and in the detection of major species (i.e., species whose molar percentage is greater than 1%) in a broad range of combustion environments. The CARS signal is several orders of magnitude greater than the spontaneous Raman signal, with a much better signal-to-noise ratio as well. A brief review of the development and applications of CARS is given below.

2.3 Development and Applications of the CARS Technique

The application of the CARS technique to combustion and gas phase diagnostics was pioneered by Taran and co-workers (e.g., Moya, et al., 1975; Regnier and Taran, 1973) at the Office National d'Etudes et de Recherches Aerospatiales (ONERA) France. Interest in the technique grew very quickly in the scientific community with many advances having been made over the last two decades. Eckbreth (1996) summarizes in detail many of the major improvements on CARS technology, which include instrument modifications as well as code development for CARS signal interpretation. At present, CARS is a well-established technique in the study of combustion. Some industrially-relevant combustion systems where the CARS technique has been used (Eckbreth, 1996) include premixed gaseous flames, diffusion flames (gaseous and liquid), internal combustion engines, sooting flames, coal flames, solid propellant rocket flames,

supersonic flows, jet engine exhausts, and model gas turbine combustors. A summary of a few CARS studies performed on turbine combustors is presented in the next section.

2.4 CARS Measurements in Gas Turbine Combustors

An early application of CARS to a model gas turbine combustor was made by Switzer, et al. (1982) at the Aero Propulsion Laboratory of the Wright-Patterson Air Force Base. The combustor was a bluff-body stabilized, non-premixed system with the fuel injected at the center of a cylindrical duct and the air flowing through an annulus between the duct and the bluff-body. Three different fuels were investigated (gaseous propane, JP-4 and JP-8) over a wide range of equivalence ratios, all at atmospheric pressure. CARS measurements were made at different axial positions throughout the flame, yielding gas temperatures and concentrations of N_2 and O_2. Furthermore, the CARS results and those of other sampling techniques were compared in order to establish the reliability of the CARS technique. Their work demonstrated the applicability of CARS to make measurements in practical combustion systems.

Bedue and co-workers (1984) made CARS measurements in a combustor designed to closely simulate a “real jet engine." The combustor operated on kerosene and could be pressurized up to 6 bar with outlet temperatures in the 1500-2000 K range. The combustion chamber was rectangular with three fuel injectors in the back wall. Secondary combustion air and dilution air for cooling were provided through air ports that were also used for optical access. Radial profiles of gas temperature were obtained at various positions in the flame. The uncertainty on the measurements was estimated to be ±50 K. This work also demonstrated the viability of CARS as a measurement technique in a hostile combustion environment.

Zhu, et al. (1993) reported CARS temperature measurements, averaged and root mean squared, in a liquid-fuel spray combustor operating at atmospheric pressure. The combustor consisted of a stainless-steel cylindrical chamber with a spray injector centered on swirling vanes for air injection at the inlet. In addition, secondary and dilution streams of air were introduced into the chamber. The fuel used in their experiment was JP-4. Zhu and co-workers reported that the use of CARS was successful, in spite of the challenge of droplet-induced breakdown near the injector.

Hedman and co-workers (1995) did very extensive experimental work on a combustor using a Pratt & Whitney injector from a military jet engine. The combustion chamber was designed to closely simulate the main flow and reaction characteristics of real jet engine combustors (Sturgess, et al., 1992). The combustor operated at atmospheric pressure burning non-premixed propane and air. The measurements included video imaging of the flame, LDA gas velocities, PLIF images of OH radical, and CARS temperatures. The gas temperature measurements were made at an air flow rate of 500 standard liters per minute (slpm) and four different inlet equivalence ratios (0.75, 1.00, 1.25, and 1.50). By analyzing the CARS temperature values, these researchers identified the pattern and degree of mixing achieved throughout the combustor, thus characterizing the practical injector.

Schmidt and Hedman (1995) reported CARS temperatures and LDA velocity measurements for the same combustor just mentioned above, but using a generic premixed swirling injector. The combustor was run using premixed propane and air at a fuel equivalence ratio of 0.75 for three different fuel injectors. The highest peak temperatures occurred in the highest swirl case, suggesting higher combustion efficiency.

It is clear from the previous examples that CARS is a reliable, proven technique in combustion processes. For this reason it was chosen to examine the turbulent, chemical and heat transfer features of a swirling fuel-lean premixed natural gas burner in this research project.

2.5 Previous Experimental Studies on Premixed Natural Gas/Air Combustion

The experimental study of premixed natural gas combustion in gas turbine combustors is relatively new with only a few published works found on the subject. A summary of the experimental studies found in the literature is presented in Table 2.1. In one of the earliest studies, El Banhawy and co-workers (1983) published a study on turbulent combustion of premixed natural gas (94% CH_4) and air stabilized by a sudden expansion in a rectangular cross-section duct. Three equivalence ratios were investigated: 0.77, 0.90, and 0.95. Also, the effects of the step sizes and wall temperature were investigated. The measurements performed were: 1) gas temperatures (mean and rms) by means of thermocouples; 2) axial velocity data (means and rms) obtained with LDA; and 3) mean concentrations of CO_2, CO and unburned hydrocarbons (UHC) by means of probes. The experiments showed an increase of the maximum temperature with equivalence ratio, and an increase of UHC with lower wall temperature.

Anand and Gouldin (1985) reported work on a combustor consisting of two co-axial swirling jets. The inner jet carried a premixed air-fuel mixture while the outer jet carried air only. This type of configuration is not common on most gas turbine can combustors. The fuels used in the experiments were propane and methane. Test conditions included variations on: 1) overall equivalence ratios (0.218 and 0.213 for methane); 2) co-swirl vs. counter-swirl of the two jets; and 3) inlet swirl levels (vain angles of 30° and 55°). All

Table 2.1. Summary of experimental studies on turbulent combustion of premixed natural gas and air reported in the literature.

				Effects Studied		
Reference	**Burner Configuration**	**Acquired Data**	**Sampling Technique**	**Equivalence Ratio**	**Inlet Turbulence**	**Inlet Swirl**
El Banhawy, et al. (1983)	Sudden expansion	Local mean and rms of gas temperatures and axial velocities. Mean species concentrations	Thermocouples LDA Probes	Yes	No	No
Anand and Gouldin (1985)	Coaxial swirling jets	Exit radial profiles of mean gas temperature, axial velocity, composition and combustion efficiency	Gas sampling probes	No	Yes	Yes
Magre, et al. (1988)	Sudden expansion Parallel flow of hot gases	Time-resolved Gas temperatures, gas velocities, CH_4 and CO concentrations	Thermocouples and CARS, LDA, shadowgraphs and probes	No	Yes	No
Roberts, et al. (1993)	Laminar flame impinging on toroidal vortex	Centerline gas temperatures, OH concentrations, axial and radial gas velocities	Thin film pyrometry, LIF and LDA	Yes	Yes	No
Nguyen, et al. (1995)	Sudden expansion	CO concentrations and gas temperatures at the exit	Tunable diode laser, CO line-pair thermometry and probes	Yes	No	No
Buschman, et al. (1996)	Bunsen burner (H_2-stabilized)	Gas axial velocities, temperatures and OH concentrations	UV-Rayleigh thermometry, PLIF and LDA	Yes	Yes	No
Pan and Ballal (1992)	Bluff-body	Time-resolved gas temperatures and axial and radial velocities	CARS and LDA	Yes	Yes	N/A
Nandula, et al. (1996)	Bluff-body	Time-resolved gas temperatures and species concentrations	Rayleigh thermometry, spontaneous Raman scattering and LIF	No	No	N/A

measurements were taken at the exit plane of the combustor. The measurements were radial profiles of mean temperature, gas composition, and velocity at the combustor exit as well as overall combustion efficiency. Sampling was carried out using probes, but the velocity probe was calibrated based on LDA measurements.

In addition, a qualitative explanation was given on the observed effect of flow conditions on combustion efficiency for the burner configuration used in the study. The researchers proposed that the reaction occurs in a thin sheet anchored on the combustion centerline prior to the recirculation zone and conveyed downstream with the flow. The combustion efficiency was proposed to depend on the radial propagation of the reaction sheet across mean flow stream tubes.

In another study, Magre and co-workers (1988) investigated the premixed turbulent combustion of air and methane in two systems: 1) a combustor stabilized by a parallel flow of hot gases; and 2) a combustor stabilized by a sudden expansion. The experiments were run at various equivalence ratios and inlet jet velocities. The measurements taken were: 1) gas temperatures using both thermocouples and CARS; 2) velocity data obtained with LDA; 3) shadowgraphs to visualize turbulence; and 4) species concentrations by means of probes. This study had the advantage of obtaining instantaneous temperature measurements (through CARS), giving information on the turbulent fluctuations. Based on these measurements, the investigators inferred that the characteristic reaction time is finite and that the recirculation zone cannot be considered to be perfectly stirred.

Roberts and co-workers (1993) studied the turbulent combustion for various fuel-air air mixtures generated by impinging a laminar, premixed flame on a laminar toroidal vortex. The fuels studied were methane, ethane, and propane. These researchers aimed

at quantifying regimes of turbulence by measuring the quenching of the flame. This was done by using Planar Laser Induced Fluorescence (PLIF) images of OH and thin film pyrometry. Their work showed, among other things, that small vortices do not quench as effectively as previously believed. In addition they established a criterion to estimate a vortex size below which all vortices can be neglected in modeling flame-turbulence interactions.

Nguyen and co-workers (1995) measured gas temperature and CO concentrations at the exit of a non-swirling reactor burning premixed natural gas and air at atmospheric pressure. Various equivalence ratios were investigated. Their study focused on the comparison of tunable diode laser in-situ measurements and probe measurements. They found CO concentrations measured by probes to be lower than the laser-based concentrations by an order of magnitude, the discrepancy increasing at temperatures above 1000 K.

The temperature measurements were made using both CO line-pair thermometry and a thermocouple and were found to be in good agreement with each other. In addition, measurements were compared with numerical computations simulating their reactor as: 1) a perfectly stirred reactor (PSR), 2) a plug-flow reactor (PFR), and 3) assuming chemical equilibrium at the exit temperature. The CO concentrations calculated from the PSR and PFR simulations were in satisfactory agreement with those measured using the tunable diode laser.

Buschman and co-workers (1996) studied premixed natural gas-air combustion in a non-swirling turbulent Bunsen burner stabilized by an H_2-pilot flame. Their work focused on simultaneous measurements of gas temperature via Planar Rayleigh

Thermometry, and OH radical concentrations using PLIF. Equivalence ratios of 0.8, 0.59 and 0.56 were studied each with unique flow rates. Their work showed the strong effects of turbulence intensity on the flame structure.

Pan and Ballal (1992) reported measurements of gas temperatures (using CARS) and velocities (using LDA) on a non-swirling bluff-body stabilized reactor burning premixed methane and air. No species concentrations were reported. Conditions investigated included: 1) four equivalence ratios (0.56, 0.65, 0.8, and 0.9); 2) two different blockage ratios; and 3) two different turbulence intensity levels at the inlet. During combustion in this burner configuration, two symmetric vortices are formed on top of the flat side of the bluff body. The size of these recirculation zones was found to decrease with increasing equivalence ratio and with increasing turbulence intensity at the inlet. Furthermore, Pan and Ballal described some specific structural characteristics of the flame and how finite-chemistry and inlet turbulence intensity affect such characteristics.

Nandula and co-workers (1996) obtained an extensive set of species concentration and temperature measurements of premixed methane-air combustion in a burner identical to that used by Pan and Ballal. No gas velocity measurements were performed. Nandula and co-workers obtained spatial and temporal measurements of: 1) simultaneous concentrations of CH_4, O_2, N_2, H_2, H_2O, CO_2 and CO using spontaneous Raman scattering; 2) gas temperature determined by Rayleigh scattering, and 3) NO and OH concentrations using Laser Induced Fluorescence (LIF). The three sets of measurements were obtained by using one technique after the other every 100 ns at every location. In addition, gas sampling probe measurements were performed at the exit plane of the combustor. They found that there is complete combustion in the recirculation zones as

evidenced by the fact that the temperature and species concentrations at the exit plane were in adiabatic equilibrium. The shear layer was identified from OH measurements and it was found that the maximum CO concentrations were in the shear layer. In addition, structural characteristics of the flame were pointed out based on the data, but no further analysis was presented.

All the pioneering work reviewed has provided insights on general structural characteristics of premixed natural gas combustion as well as how the reaction proceeds in specific configurations. It must be noted that none of the reviewed works presented complete measurement maps throughout the combustor of gas temperatures, species concentrations, and gas velocities. In addition, inlet swirl effects were examined in only one burner configuration (Anand and Gouldin, 1985), which was not a common gas turbine configuration. Therefore, further work is warranted to obtain more detailed information on burner configurations relevant to practical gas turbine combustors.

In this research, detailed gas temperature measurements were taken in a Laboratory-Scale Gas Turbine Combustor for four different lean premixed combustion conditions where the fuel stoichiometry and inlet swirl were varied.

The lean premixed, swirling conditions were chosen to be relevant to practical gas turbine systems. First, they yield low emission levels of NO_x due to low gas temperatures, and low emission levels of CO and UHC due to excess O_2. The main reason for this is that the amount of oxidizer available (e.g., air) in lean mixtures will be sufficient to consume all the fuel and will absorb part of the heat released by the combustion (see Figure 2.4). Second, the chosen conditions included varying degrees of flame stability (i.e., self-sustainability) from a nearly unstable case to a very stable one.

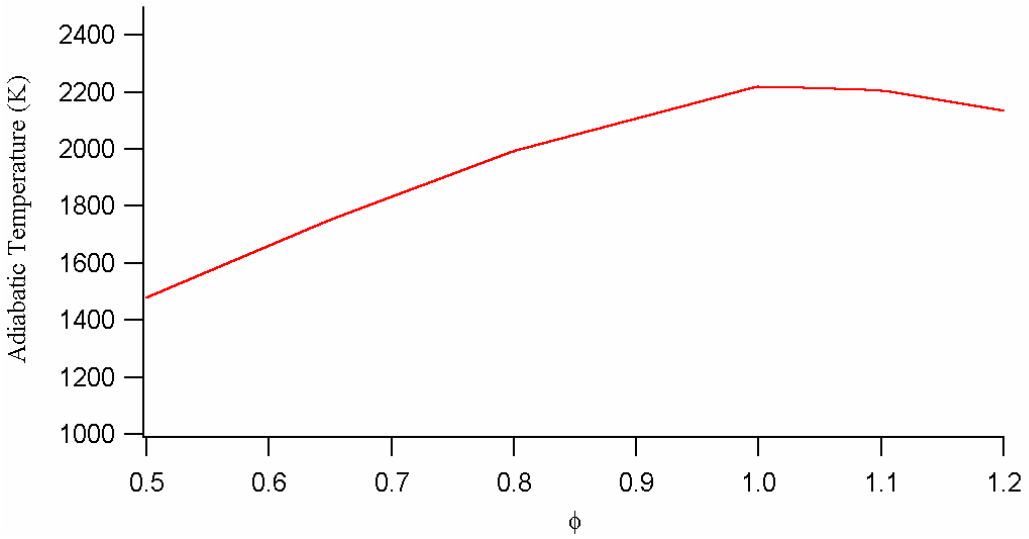

Figure 2.4. Variation of adiabatic temperature with f.

The knowledge derived from this work adds new information to the field of turbulent premixed combustion.

2.6 Previous Premixed Combustion Studies Related to This Work

Prior to this work, two studies were conducted on the same combustion conditions and in the same experimental combustor as in this work: PLIF OH data (Hedman, et al., 2000a), and LDA velocity data (Murray, 1998; Hedman, et al., 2000b). The PLIF OH data gave qualitative measurements of the concentrations of OH, an important reaction intermediate in the combustion process of natural gas, and of hydrocarbons in general. The LDA data show how the gases move within the combustor.

Based on LDA data, Hedman and coworkers (2002b) showed the existence of a vortex surrounded by two recirculation zones in the LSGTC for the each of the combustion cases studied in this work (see Figure 2.5). The vortex is generated by the tangentially swirling inlet stream (see the heavy-dotted line in Figure 2.5). The "side

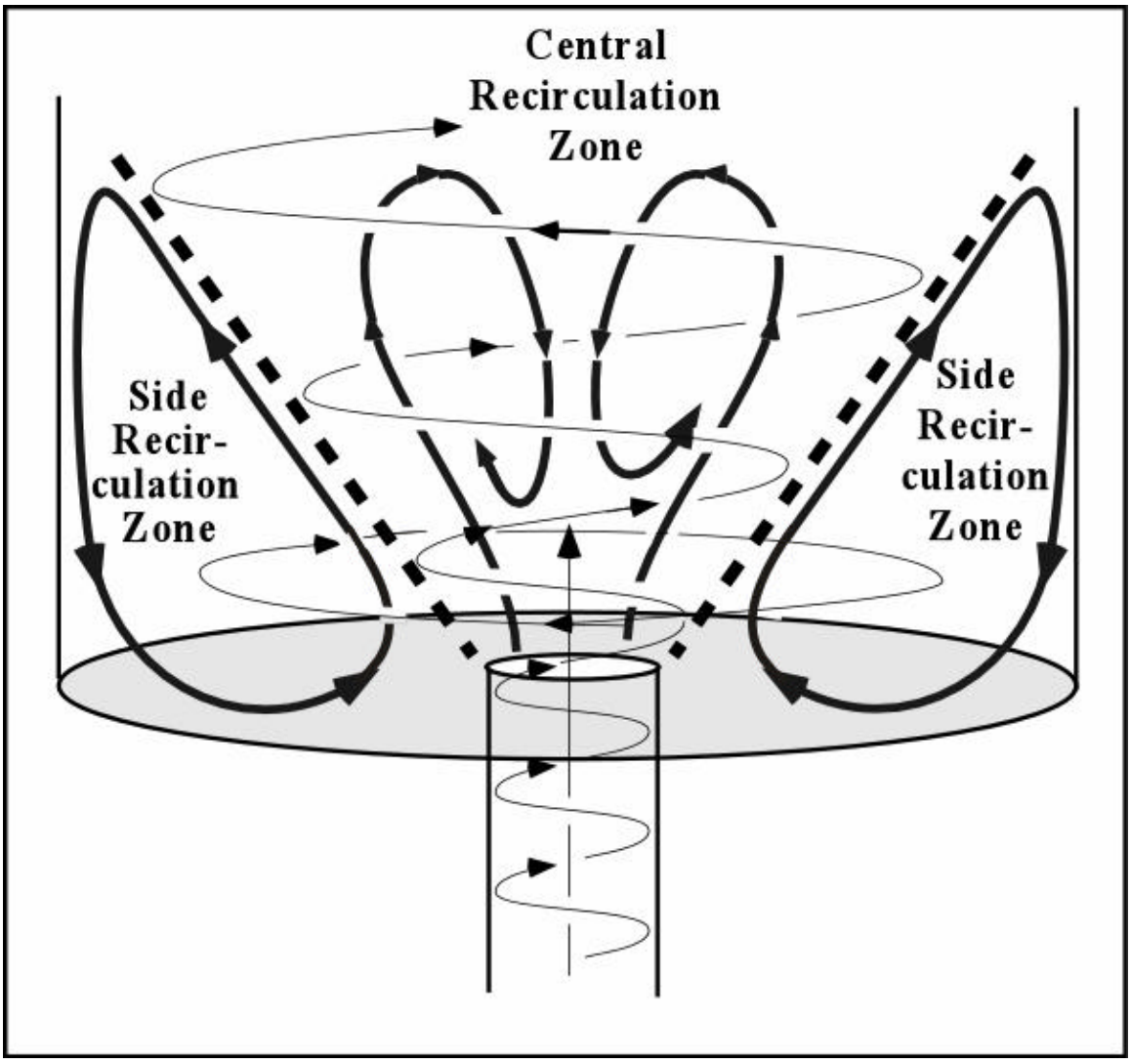

Figure 2.5. Recirculation patterns in the LSGTC, adapted from Hedman, et al., (2002b).

recirculation" zone (SRZ) exists outside the vortex and is a current at the bottom corners moving towards the centerline and bringing reacted gases down from the flame zone towards the inlet. The "central recirculation" zone (CRZ) exists inside the vortex and is a flow at the center of the combustor that travels down from the top of the flame towards the inlet.

3. THE BYU DUAL DYE SINGLE STOKES CARS INSTRUMENT

3.1 CARS Instrument Description

The BYU dual dye single Stokes CARS instrument consists of one laser source and a collection of several optical and electronic components. The instrument can be partitioned into three groups as shown in Figure 3.1: A) main laser source; B) CARS signal generation; and C) CARS signal reception. Each component of the CARS instrument is described briefly in Table 3.1.

In the main laser source section of the instrument (Figure 3.1A), an Nd:YAG laser from Quanta-Ray produces an infrared (IR) beam, with a gaussian spatial distribution and at a wavelength of 1064 nm, which powers all lasers needed to generate the CARS signal. The Nd:YAG laser was set to operate with the Q-switch turned on at 60 J/pulse on the oscillator and 50 J/pulse on the amplifier. This IR laser goes through a harmonic generator (HG) to generate a linearly p-polarized green laser at a wavelength of 532 nm.

A pellin broca prism is then used to separate the superimposed green and unconverted IR beams coming out from the HG. After being separated, the green laser energy is 290 mJ/pulse whereas the IR beam energy is 212 mJ/pulse. This green laser, from here on referred to as the primary beam, is then redirected towards a Galilean telescope by two right-angle prisms which are separated by a distance that synchronizes the arrival of the all the lasers at the sampling location. The Galilean telescope (-50 / +200 mm focal length lenses) enlarges the primary beam diameter to become the collimated beam B-1.

A) Main laser source

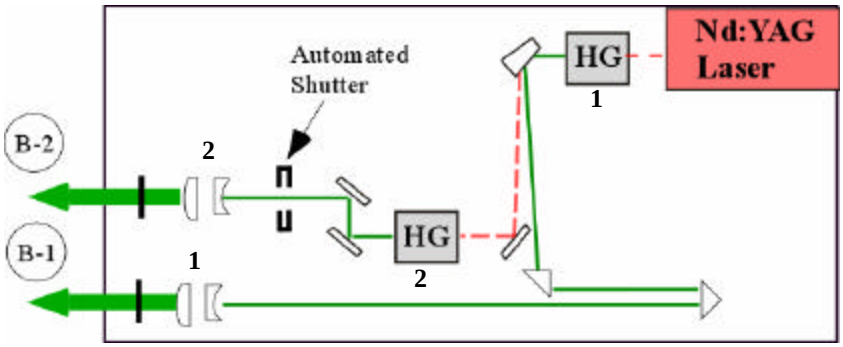

B) CARS Signal Generation:
Dye laser and phase-matching

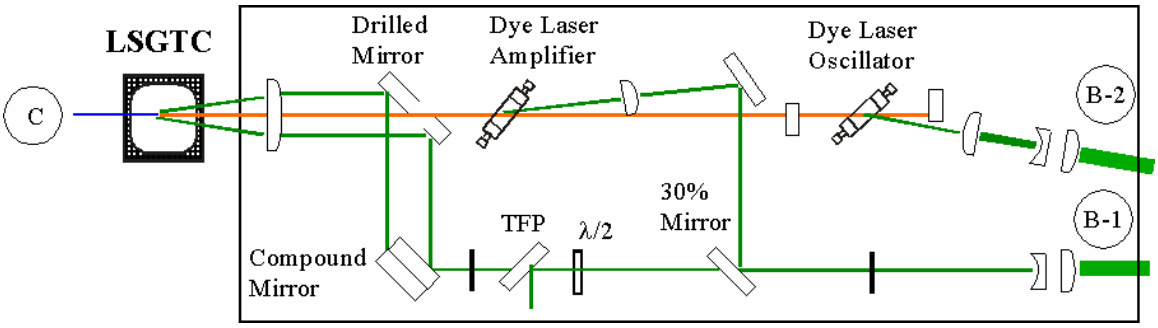

C) CARS Signal Reception:
Collection, detection and storage

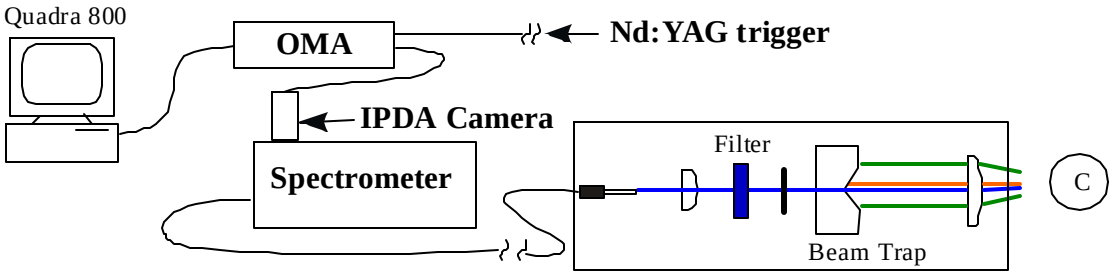

D) Legend

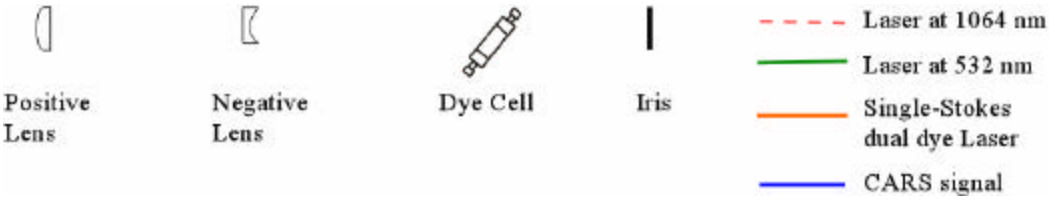

Figure 3.1. Schematic of the BYU dual dye single Stokes CARS instrument.

Table 3.1. Purpose of CARS instrument components (see Figure 3.1).

Component	Purpose
A) Main laser source	
Nd:YAG Laser	Generate infrared laser beam at 1064Generate infrared laser beam at 1064 nm
HG 1	Generate pump beam, B-1 at 532 nm
Pellin Broca Prism	Separate pump beam from residual infrared beam
Right angle prisms	Set pump beam trajectory
Galilean 1	Increase pump beam diameter to minimize Rayleigh scattering losses and to ensure
HG 2	Generate secondary beam, B-2 at 532 nm, used downstream to generate dual dye laser.
Shutter	Automatically block secondary beam to measure background intensity
Galilean 2	Increase pump beam diameter to minimize Rayleigh scattering losses and to ensure
B) CARS Signal Generation	
Galilean B-1	Reduce pump beam B-1 diameter. This diameter will determine the diameter of the pump beams at the sample volume
Partially reflecting mirror	Reflect part 30% of the pump beam to amplify the dual dye laser energy
Half-wave plate and TFP	Regulate the pump beam energy downstream
Compound Mirror	Split the pump beam into two beams
Galilean B-2	Reduce pump beam B-2 diameter. This diameter will determine the diameter of the dual dye laser beam at the sample volume
Positive lens	Send secondary laser through the dye cell of the Dye Laser Oscillator
Dye Laser Oscillator	Generate the dual dye laser
Mirror and Positive Lens	Send amplifying beam taken from pump beams to the Dye Laser Amplifier
Dye Laser Amplifier	Increase the energy of the dual dye laser
Drilled Mirror	Send the two pump beams and the dual dye laser to the focusing field lens
Focusing field lens	Focus the pump and dye beams into the sampling volume for CARS signal generation
C) CARS Signal Reception	
Collimating field lens	Collimate the CARS, dual dye and pump beams
Beam trap	Separate the CARS signal from the dye and pump beams
Iris and Filter	Remove light that is not the CARS beam through
Spectrometer, IPDA camera, OMA and computer	Record the spectra in the CARS beam

The residual IR laser coming of the pellin broca prism is reflected by a mirror into a second HG to produce another linearly p-polarized green laser, the secondary beam, which is used as the energy source for the dye laser oscillator. The secondary beam is then redirected towards a secondary Galilean telescope by two mirrors coated for optimal reflection of 532 nm light—the residual IR light passing through the mirrors being collected into copper beam traps (not shown).

The shutter before the secondary Galilean telescope is used to automate the acquisition of background noise (see the "Spectra Preprocessing" section in Chapter 4). The shutter, which is activated by the instrument computer (see Figure 3.1C), acts as a switch for the dye laser—when closed, the shutter blocks the secondary green laser and consequently turns off the dye laser. The Galilean telescope (-50 / +120 mm) enlarges the secondary beam diameter to become the collimated beam B-2 with 25 mJ/pulse of energy. Enlarging the primary and secondary beams into B-1 and B-2 minimizes energy losses due to Rayleigh scattering, while collimating the beams keeps them from diverging as they travel about 23 feet towards two periscopes (not shown) at the beginning of the signal generation table (see Figure 3.1B). Each periscope is made of two large right-angle prisms and raises each beam to the height of the signal generation table.

At the signal generation table (Figure 3.1B), the primary beam B-1 is reduced in size by a Galilean telescope (+200 / -125 mm) and then taken to a partially-reflecting mirror, where 30% of the primary beam energy is reflected at a right angle in order to be used on the dye laser amplifier. The rest of the primary beam continues towards an "optical throttle", made up of a half waveplate ($\lambda/2$) and a thin film plate (TFP) polarizer, newly added in this work because it can handle the extra power in the laser (140 mJ/pulse in 10

nanoseconds). This optical throttle is used to regulate the amount of energy in the outgoing primary beam by rejecting varying amounts of energy of the incoming primary beam.

The energy regulation is accomplished by introducing a degree of s-polarization in the primary beam by rotating a half waveplate and by using the TFP to reflect away the s-polarized component of the primary beam towards a beam trap (not shown). Only the p-polarized component of the primary beam goes through the TFP. Its energy is determined mainly by how much energy was rejected because it was allocated in the s-polarized component. The degree of s-polarization introduced in the primary beam is two times as much as the rotation of the waveplate. For example, a waveplate rotation of 45^{o} rotates the p-polarized primary beam by 90^{o}, completely s-polarizing the beam.

After the throttle, the primary beam goes towards a compound mirror (as used by Boyack, 1990), which splits the primary beam into two parallel beams and directs them towards the drilled mirror. These two parallel beams are now the "pump beams" used to generate the CARS signal, and their centers are about 1.5 cm apart.

At the beginning of optical table B, the secondary beam B-2 is aimed at an angle towards the oscillator dye cell, and, on its way, is first reduced in size by a Galilean telescope (+150 / -50 mm) and then focused past the oscillator dye cell by a positive lens (+300 mm). About 15 cm after the focusing lens, the secondary beam passes through the oscillator dye cell, generating the broadband dye laser. The cell is tilted near the Brewster's angle relative to the dye laser in order to maximize p-polarized laser output. The dye laser cavity is enclosed by two flat mirrors coated for reflection of broadband light centered at 589 nm—a fully-reflecting mirror and a 50% reflecting mirror, each

about 10.8 cm apart from the dye cell. The residual secondary beam laser is contained in a copper trap, whereas the dye laser is directed towards the amplifier cell which is also tilted at near the Brewster's angle.

At the amplifier cell, the dye laser power is increased from 8 to 45 mJ/pulse energy by nearly superimposing it with the amplifying green laser (78 mJ/pulse) that was split at the 30% mirror, redirected by a full mirror and focused past the amplifying cell with a +700 mm focal length lens. The residual green laser is trapped (not shown), whereas the amplified dye laser is then enlarged in diameter by a Galilean telescope (-100 / + 177 mm) and passes through the drilled mirror hole (drilled at a 45^{o} angle). The position of the positive lens of the Galilean can be adjusted in all three directions at right angles, which is useful for the fine adjustments required for phase-matching the CARS signal.

At the drilled mirror, the pump lasers are reflected to be in a plane below and parallel to the dye laser. The centers of the pump lasers are 4.5 cm below the dye laser center to ensure phase matching for the N_2, CO, O_2 and CO_2. Before the focusing field lens, the dye beam has 45 mJ/pulse of energy whereas the pump beams maximum available energies are 52 and 67 mJ/pulse. The three beams then go through the field lens (+300 mm), which focuses them on the sampling diagnostic volume.

The time resolution of the instrument is dictated by the pulse duration and frequency of the Nd:YAG laser, which in this work were respectively about 10 nanoseconds and 10 Hz. On the other hand, the spatial resolution of the CARS instrument is determined by the diameter (D) of the beams prior to focusing on the diagnostic volume, the focal length f_l of the focusing lens, and the wavelength l of the beams. The sampling volume can be approximated as a cylinder of diameter d and length L, both calculated

according to Regnier (1974):

$$f = \frac{4lf}{pD} \tag{3.1}$$

$$L = \frac{3pd^2}{l} \tag{3.2}$$

The approximate diameters of the beams right before the field lens are 10 mm for the dye beam and 13 mm for the pump beams. According to these values, the minimum dimensions of the diagnostic volume are estimated to be 20 μm in diameter and 1 mm long.

One significant practical challenge was to minimize the heat transmitted from the flame to the optics near the burner. Such heat may deform the shape of the lenses and mirrors of the instrument to the point of misaligning the lasers, and may even damage these optical components. In this work, two metal heat shields (not shown) were mounted at the ends of the optical tables near the LSGTC. Each metal shield had one 0.75 in diameter hole to allow passage of the laser beams. Additional cooling for each field lens was provided by one fan that circulated cool air from the lab into the optical table B and another fan right next to the field lens.

After the diagnostic volume, the three original beams and the generated CARS signal beams pass through another positive lens (+350 mm), where they are collimated. A copper beam trap downstream collects the dye and pump beams, while the CARS signals pass through an iris that partly blocks scattered green and dye laser light. Any remaining scattered green and dye laser light is filtered out using a custom made filter (Warren, 1994) that has maximum throughput centered at 475 nm and a bandwidth of 50 ±10 nm at Full Width Half-Maximum (FWHM). The CARS signals are focused by a positive lens

(+100 mm) onto a custom-made fiber optic that has a 250 μm inlet diameter that tapers down to 50 μm. The fiber optic conducts the CARS signals into the spectrometer (see Boyack, 1990) where they are optically manipulated for detection and recording.

The CARS signal detection and recording equipment used in this work is the same previously used by Warren (1994). The spectrometer spreads and focuses the CARS signal onto the Intensified Photo-Diode Array (IPDA) of a PARC 1421B camera. This IPDA has 1024 photo-diodes (pixels) evenly distributed over a one-inch long array. Each pixel measures light intensity in "detector counts".

The IPDA camera is controlled by an EG & G Optical Multi-channel Analyzer (OMA) through a 1461 interface (Boyack, 1990). By scanning the IPDA, the OMA obtains the detector counts detected by each of the 1024 pixels and stores them in arrays of 1024 elements in its built-in memory, which can hold up to 1000 full IPDA scans. The IPDA scans are then transferred from the OMA to the computer where they are stored in a hard drive in ASCII format.

The IPDA was operated at a temperature of $-5^{o}C$ to reduce the amount of background noise due to thermal excitation of the photo-diodes. For single-shot measurements, the OMA was set to combine into a single measurement the addition of two consecutive IPDA scans. This approach, which has previously been validated (see Boyack, 1990; Anderson, et al., 1986), is warranted because of limitations in the synchronization capabilities between the OMA and the trigger signal from the Nd:YAG laser output console.

The OMA has a variety of operational modes and capabilities, including signal triggering, such as the one used to control the dye laser shutter (see Figure 3.1A). The

shutter is activated and controlled via interfacing software in a Quadra 800 Macintosh computer that communicates with the OMA through a General Purpose Interface Board (Warren, 1994). Warren integrated the interfacing software into Igor (Wavemetrics, Inc.), a comprehensive graphics and data analysis software with programming capabilities, providing a very flexible and convenient interface for data acquisition.

The original Igor Macros used by Warren were significantly modified to meet the needs of this research (see Appendix A). Two main modifications were made: 1) the OMA and IPDA camera were operated the same way as outlined by Boyack for each data acquisition task (see CARS sampling section in the Experimental Program chapter); and 2) an automated procedure was implemented to name the experimental files according to a convention designed for the data collected in this work.

3.2 The Dual Dye Single Stokes Laser

3.2.1 Development

As part of this dissertation work, development was completed for the broadband dye laser that was first introduced by Haslam and Hedman (1996). This new dye laser is based on a mixture of two dyes. The spectral energy distribution of the resulting Stokes allows simultaneous CARS measurements of N_2, CO, O_2 and CO_2. Haslam and Hedman used two new Pyromethene dyes, P567 and P650, both available from Exciton, Inc., dissolved in ethanol. The resulting broadband laser exhibited a bimodal spectral energy distribution spanning from about 560 nm to 620 nm—covering completely all Stokes frequencies for N_2, CO, O_2 and CO_2 (see Figure 3.2) relative to a pump beam of 532 nm.

Haslam and Hedman noted that the dye laser degraded within a few hours of use, an issue that required further investigation. This degradation resulted not only in the decay

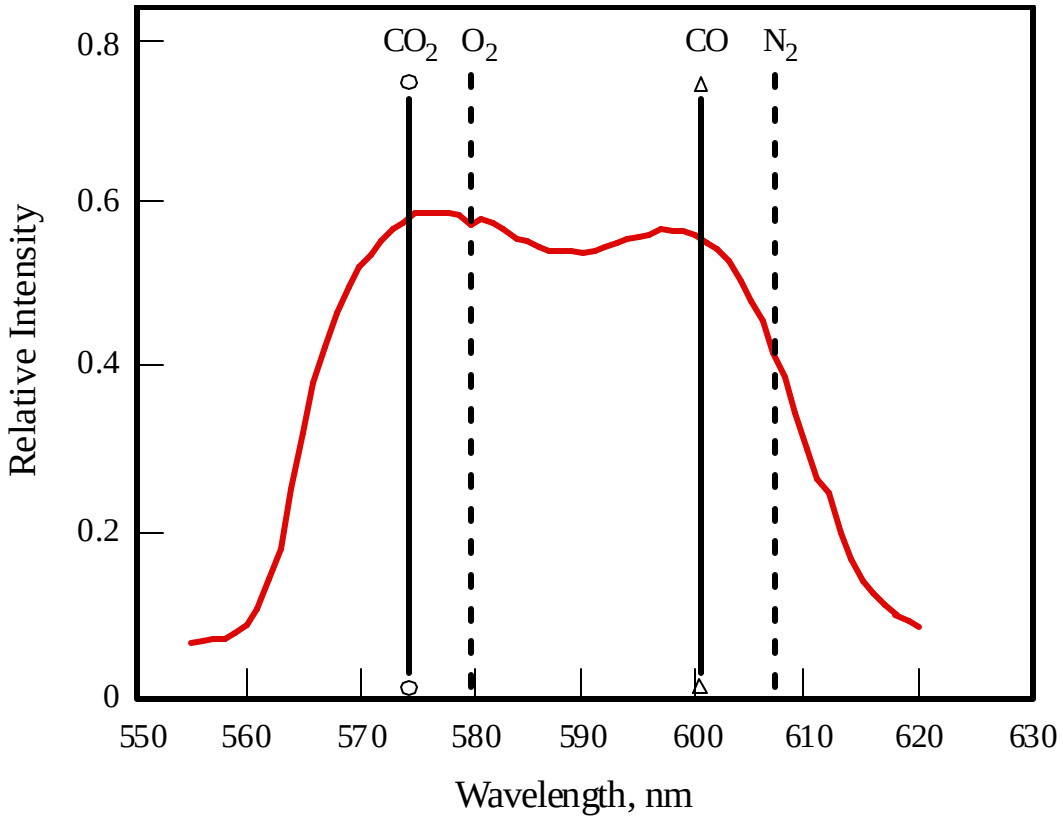

Figure 3.2. Spectral profile of the dual dye single Stokes laser showing the Raman Stokes wavelengths relative to 532 nm for N_2, CO, O_2 and CO_2. Adapted from Haslam and Hedman (1996)

of dye laser power, but also in noticeable time changes of the dye spectral profile—an essential piece of information needed to accurately interpret the CARS spectra. Given the instrumentation available at the laboratory, accounting for this degradation could only have been performed in an approximate manner, perhaps by stopping the combustion experiments at short time intervals to measure intermediate dye profiles, and then postulating some sort of time variation (e.g., linear) to obtain intermediate dye profiles. Besides increasing the uncertainty of the measurements, this approach would also have required a significant amount of extra time. It takes at least four hours every time to cool down the LSGTC, make the dye profile measurements, and then restart and stabilize the LSCTC.

In the course of this research, it was discovered that the rapid decay on the dye laser was accompanied by degradation in the PVC tubing used to circulate the dye mixture through the dye cells. It was later found out from tubing manufacturer specifications that PVC tubing is quickly degraded by ethanol, which explains why the PVC tubing became noticeably colored within a few hours after replacement. The problem was solved by using polyethylene tubing instead of PVC tubing. When using the polyethylene tubing, both the dye laser power and spectral distribution over the areas of interest remained practically constant throughout 3 to 4 days of continuous dye laser operation of 8 to 12 hours a day.

Another practical issue that needed to be addressed was how to moderate the high power output of this new broadband dye laser. Too much power in the dye laser can prevent the acquisition of meaningful measurements. In the BYU CARS instrument, dye laser powers as high as 100 mJ/pulse have been achieved. This is powerful enough to damage the quartz windows of the LSCTC and to ionize the air molecules at low temperatures when focused. In addition, even if there is no ionization, high electric field intensities can distort the CARS spectra via the Stark effect (Eckbreth, 1996).

In an attempt to lower the dye laser power (Haslam, 1996), changes were made to the green laser beam used to drive the dye laser oscillator, also referred to as the secondary beam (see Figure 3.1B, in the CARS Instrument Description section). The changes made included (a) lowering the secondary beam power with the harmonic generator, and (b) rotating the polarization of the secondary beam to lower the dye oscillator power conversion. However, during the course of this work, it was discovered that the rotation of the secondary beam's polarization resulted in an elliptically polarized dye laser,

generating CARS spectra that cannot be interpreted correctly by available software (Farrow, 1995). One important requirement of the CARS modeling in the CARS interpreting software used in this work is that all laser beams in the instrument are linearly polarized.

In this research, a different approach was taken to control the dye laser power while keeping the laser linearly polarized. The dye laser power was reduced to about 45 mJ/pulse by lowering the power output of the Nd:YAG laser, while maximizing the conversion in the secondary beam's harmonic generator and leaving the secondary beam p-polarized. The Nd:YAG oscillator gain was set to 60 Joules/pulse while its amplifier gain was set to 50 Joules/pulse with the Q-switch on.

Using the new laser power control scheme, the dye laser spectral profile for the mixtures suggested by Haslam and Hedman (see Table 3.2) changed dramatically towards the red side of the light spectrum; i.e., more of the beam energy was now found in wavelengths greater than 600 nm. At room temperature, this dye laser spectral profile generated an almost negligible O_2 CARS signal, while increasing the CARS signal for N_2 by almost an order of magnitude—which was unacceptable for the purposes of this research. In order to balance the CARS signal strengths of all four species of interest, new dye concentrations were developed for this work (see Table 3.2).

The new dye concentrations are the same for both the oscillator and amplifier dye cells, in contrast to using different concentrations, as reported by Haslam and Hedman. The mixtures require careful preparation because the spectral profile of this laser is very sensitive to changes in the concentration of P650 and the amounts involved of P650 are small. For example, a change of 0.1 mg of P650 (about 5% change in a mixture) causes

Table 3.2. Changes in pyromethene dye concentrations in ethanol during the development of the dual dye single Stokes laser.

Mixture / Dye lasing section	Haslam and Hedman (1996)		This work	
	P597 (mg/l)	P650 (mg/l)	P597 (mg/l)	P650 (mg/l)
Oscillator	53.40	3.30	51.77	2.01
Amplifier	45.60	3.20		

appreciable and undesirable changes in the ratio of N_2 and O_2 CARS signal strength at room temperature.

In this work, the solutions were prepared by first mixing 1.7 mg of P650 and 51.77 mg of P597 in ethanol, followed by incremental additions of one or two ml of a 0.05 mg/l P650 solution via a syringe into the dye circulation systems for both the dye laser oscillator and amplifier. In between additions of P650, the ambient air CARS signals of N_2 and O_2 were allowed to stabilize at their new levels (approximately 5 minutes). The additions continued until the ratio of CARS signals of N_2 and O_2 was approximately 2:1.

3.2.2 Advantages and Limitations

The main advantage of the dual dye single Stokes laser is that it significantly reduces the optical components needed to set up the CARS instrument. The consequent decrease in required space makes it possible to deploy the instrument in circumstances where optical table space is limited, such as the case when other equipment must be located near the burner. In addition, it is generally easier and faster to set up the dual dye single Stokes CARS instrument than when two dye lasers are involved.

At first, it would appear that the higher power available in the dual dye single Stokes laser would be a definite advantage. However, the fact that the dye laser power is

distributed over such a large spectral range is a limitation in itself because only a small portion of the laser's energy is actually used in generating the desired CARS signals. In addition, the total dye laser power can only be raised so much before risking the introduction of the Stark effect (Eckbreth, 1996).

The dual dye single Stokes laser is also limited by the very fact that it is only one beam—it cannot be optimally aligned for each of the four species, thus requiring a trade-off in alignment. As stated earlier in the background section of this dissertation, in order to generate the CARS signal, it is essential to align the Stokes and pump beams so their wave vectors satisfy the phase-matching condition. The importance of phase matching is illustrated by the fact that when maximizing the CARS signals for N_2 and CO, the signal intensities for O_2 and CO_2 become unacceptably smaller. This alignment trade-off introduces two limitations: it does not allow taking full advantage of all the energy available to excite each species, and it restricts where the CARS signals can be focused at the fiber optic entrance. The latter limitation means that one can be focusing the CARS signals for N_2 and CO near the center of the fiber optic while the CARS signals for O_2 and CO_2 are closer to the edge of the fiber optic, which may be a problem when beam steering is present (as explained below).

The limitations introduced by the alignment trade-off required by the dual dye single Stokes laser presented a practical problem during the acquisition of the combustion data in the LSGTC. As mentioned earlier, throughout the course of the experiments, the heat released by the LSCTC, particularly at the hottest locations near the walls, caused small thermal deformations on the field lenses. This was sufficient to misalign the single Stokes beam to a degree that warranted realignment during testing.

In addition, changes in local density gradients due to flame turbulence seemed to be causing beam steering, i.e., deviating the path traveled by the CARS signals and consequently whether they reached the fiber optics entrance. Several CARS spectra had neither O_2 nor CO_2 signals. In a premixed natural gas/air system, this is a strong indication that their CARS signals were steered outside the fiber optic entrance. The effects of beam steering could be minimized if it were possible to aim both the O_2/CO_2 signals as well as the N_2/CO signals near to the center of the fiber optic entrance.

In conclusion, it is recommended that the performance of the single Stokes instrument be evaluated in the future against the performance a dual Stokes instrument such as the one used by Boyack (1990). In particular, if new dyes are identified that offer higher conversion efficiencies, and therefore more power concentrated in the N_2/CO and O_2/CO_2 spectral ranges, it is possible that a dual Stokes system will perform better than the single Stokes system. Such a dual Stokes system would deliver more of the Stokes laser energy into the CARS generation process and it would be possible to maximize all signal strengths by aligning the N_2/CO side independently of the O_2/CO_2. This alignment independence would also allow focusing all CARS signals near to the center of the fiber optic, helping to mitigate (in principle) the effects of beam steering and of lens deformations due to heating.

4. CARS SPECTRA INTERPRETATION

Extracting the temperature and species concentrations of each CARS sample obtained in this work is a complex task. This chapter provides: 1) a description of the numerical processing performed to prepare each spectrum for interpretation; 2) a brief explanation of the interpretation procedures used to obtain gas temperature and species concentrations; and 3) a description of the software developed in order to accomplish the task of interpreting the large collection of data obtained in this work.

4.1 Spectra Preprocessing

4.1.1 Obtaining the CARS Spectrum from Recorded Spectra

The spectra recorded by the BYU single Stokes CARS instrument, I_{raw}, need to be preprocessed (i.e., numerically manipulated) before they are ready for interpretation. Note that I_{raw} stands for all the intensity values in the range of light wavelengths of the CARS sample. This wavelength dependency is not stated explicitly—a convention of the field of spectroscopy because the wavelength dependency is "implied" by the nature of the quantity itself. For clarity, however, the light wavelength dependency of a quantity will be pointed out whenever the quantity is introduced for the first time in this dissertation.

Consider the single-shot CARS sample (see Figure 4.1a) obtained in one of the combustion experiments of this work using the BYU dual dye single Stokes CARS

a) Raw spectra and background noise

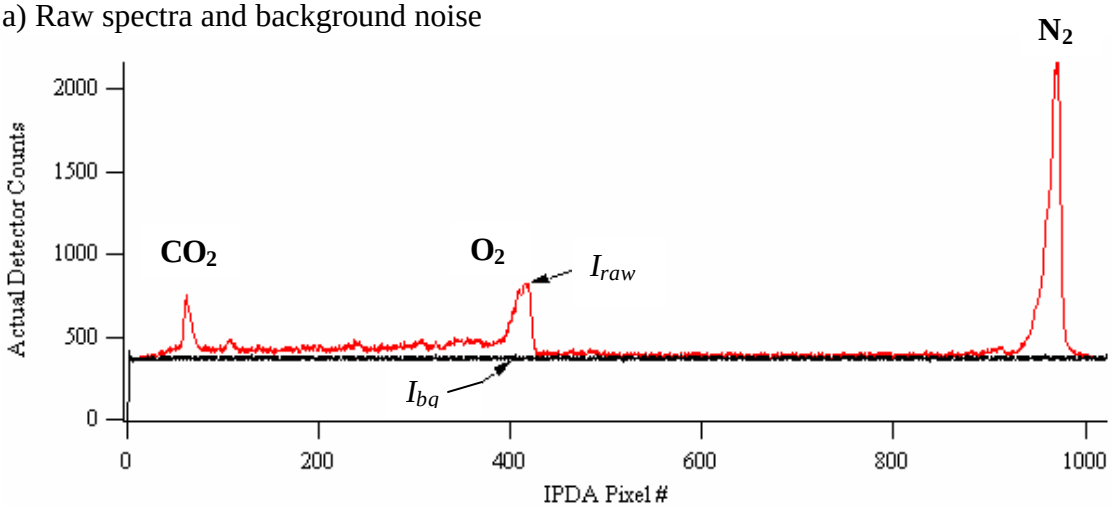

b) Background-subtracted spectra

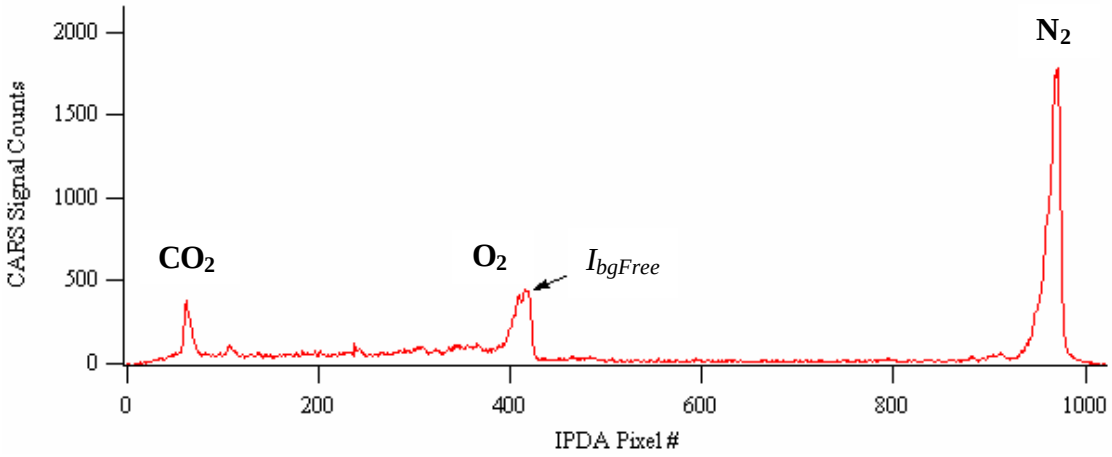

Figure 4.1. A raw multi-species CARS measurement and its corresponding background-subtracted spectrum.

instrument. Each spectrum in Figure 4.1 consists of 1024 intensity values (measured in IPDA detector counts) plotted against their corresponding wavelength, which is represented by the IPDA pixel number (see the Spectral Dispersion section below). The three highest peaks, from left to right, correspond to the CARS spectra for CO_2, O_2, and N_2, respectively. This sample has certain instrumental dependencies, due to limitations of the IPDA camera, that need to be taken into account in order to obtain the "true" CARS spectra, I_{CARS}. There are three IPDA camera dependencies taken into account in

this work: background noise, image persistence, and detector non-linearity. Background noise and detector non-linearity are relevant to both single-shot and average samples, whereas image persistence is only relevant to single-shot samples.

Background noise originates mainly from the IPDA's dark current and from any extraneous light that may arrive on the detector. Dark current arises from charge carriers produced by heat generated as the IPDA is operated, and thus it exists even in the absence of light. Although the dark current noise cannot be eliminated, it may be reduced by operating the IPDA at low temperatures. Thus, in this work, the IPDA was operated at –5 ^{o}C. Other background noise from extraneous light may arrive through the fiber optic from such sources as scattered laser light from the pump and dye beams, flame luminosity, or from ambient laboratory light entering the spectrometer.

In the BYU single Stokes CARS instrument, the background noise consists almost exclusively of the IPDA dark current because practically all extraneous light was kept from reaching the IPDA. Figure 4.1a shows an averaged sample of background noise I_{bg} across the wavelength range of the IPDA. This noise exhibits a flat baseline of about 370 detector counts just below the raw CARS signal. The background noise is properly accounted for by subtracting its intensity values from CARS signal values of corresponding IPDA pixel as follows

$$I_{bgFree} = I_{raw} - I_{bg} \tag{4.1}$$

The result is a background-free spectral curve I_{bgFree}, as shown in Figure 4.1b.

4.1.1.1 IPDA Image Persistence

Image persistence is an effect that arises from the limitations of the IPDA and is only relevant for single-shot samples taken in very short time intervals. Image persistence

occurs when a fraction of the light intensity reading in each IPDA pixel for a sample is a residue from the intensity of a previous sample. The IPDA measures light intensity in "detector counts", which are a function of the electric charges generated in each pixel by the light. After scanning the IPDA to obtain the detector counts in each pixel, the OMA proceeds to clear the IPDA from the charges. For the time intervals (0.1 seconds) between each single-shot used in this research, the OMA can only perform seven clearing scans in between consecutive CARS samples, which are not always enough to completely clear the charges in each IPDA pixel. Thus, each single-shot sample must be corrected for the residual intensity left over by the IPDA image persistence.

Boyack (1990) developed the following empirical correlation to estimate the residual intensity *ImaPer* in a sample due to image persistence from the previous sample in the IPDA and OMA system used in this work:

$$ImaPer(I_{bgFree,Prev}) = 0.030095 \times I_{bgFree,Prev}^{0.80575} \quad \textbf{(4.2)}$$

where $I_{bgFree,Prev}$ stands for the background-free intensity values of the previous single-shot sample recorded in a given IPDA pixel by the previous sample. The functional notation $ImaPer(I_{bgFree,Prev})$ implies that this correlation is to be used for each of the 1024 intensity readings that make up $I_{bgFree,Prev}$. The convenience of this notation will become apparent later as the use of *ImaPer* is described.

Boyack's correlation, Equation 4.2, corrects for the image persistence effect in the right direction because it subtracts from the current signal a small fraction of the previous one. It must be noted that the correction is only approximate and somewhat simplistic, as it cannot account for possible contributions from more than one previous sample. However, it is considered sufficient because the errors introduced by image persistence

are generally small. According to Boyack, the errors in temperature from this effect are normally less than 50 K, although in extreme cases can reach up to 400 K, while errors introduced in the species concentrations can be up to 10%.

The degree that image persistence affects a sample depends on the strength of the intensity of the previous sample relative to the new sample. When the signal intensity of a previous sample is less than or about the same as the new sample, the residual intensity will be no more than 1% of the new signal. When the previous signal intensity is significantly larger, e.g. 5 to 10 times, image persistence effects can account for as much as 5 to 10% of the new signal. This scenario is particularly possible in turbulent combustion experiments, where the turbulent variation of gas temperatures can introduce significant differences in the relative CARS signal strengths of consecutive samples. In such cases, significant variations of signal strength will occur, because, at low pressures, the CARS signal strength varies with the square of the sample density (Eckbreth, 1996), which translates into an inverse variation with the square of the temperature in a gas.

For example, if a sample of a hot gas at 900 K were preceded by a sample of a colder gas at 400 K, image persistence from the hot gas CARS sample could account by as much as 6% of the intensity in the cold gas CARS sample. In this case, the expected error introduced in the temperature could be about 50 K unless the correction factor was used (Boyack, 1990).

4.1.1.2 IPDA Detector Non-Linearity

Detector non-linearity is another limitation in the capability of the IPDA to quantify the intensity of the light being measured. The light intensity counts reported by a pixel in the IPDA are just a fraction of the actual light intensity received, and this fraction varies

logarithmically with the intensity of the light being measured, hence the term non-linearity. This limiting behavior is believed to be common to P-20 phosphor based detectors (Snelling, et al., 1989) such as the one used in this work.

Equation 4.3 shows a correlation developed by Boyack (1990) quantifying *NonLin*, the non-linearity of the IPDA used in this work:

$$NonLin(I) = \frac{I}{0.60432 + 0.04765\ln(I)} \qquad \textbf{(4.3)}$$

where I stands for all the background-free intensity values of a single-shot sample corrected for image persistence from the previous sample as follows:

$$I = I_{bgFree} - ImaPer(I_{bgFree,Prev}) \qquad \textbf{(4.4)}$$

Consistent with the definition of Equation 4.2,the functional notation in Equation 4.3 implies that these correlations are to be used for each of the 1024 intensity values in I. Similarly, Equation 4.4 implies that the image persistence from the previous single-shot sample measurement in each of the 1024 pixels is subtracted from corresponding pixel values in the current sample I_{bgFree}. According to this equation, when a pixel measures 20 counts and below, it is actually detecting only about 70% of the actual light intensity. This percentage increases logarithmically with detected counts, and at about 4000 counts, the detector measurement is practically the same as the actual amount of light received by the pixel.

Detector non-linearity must be accounted for because it has been shown to introduce significant errors in interpreting CARS spectra unless the spectra are corrected for this effect. It has been estimated (Boyack, 1990) that errors in temperature values due to non-linearity vary from 7% at room temperature to 2% at 2000 K, while errors in species

concentrations are of the order of 2% or less. These errors are more significant at low temperatures where peak counts of the CARS spectrum are high. In this case, the detector non-linearity effects vary significantly throughout the CARS spectrum, being more noticeable at the wings than at the peak, and the detector non-linearity shrinks the curve more appreciably. On the other hand, for high temperatures, the peak counts are usually not much higher than the wing counts, and the detector non-linearity is more or less even throughout the spectrum, hardly changing the spectrum shape and therefore introducing only a small amount of error.

The estimated actual CARS spectrum I_{CARS} is obtained from the accumulated manipulation of the IPDA pixel intensities described by Equations 3.1 through 3.4, leading to

$$I_{CARS} = NonLin(I) \tag{4.5}$$

4.1.2 Obtaining the CARS Susceptibility From the CARS Spectrum

After obtaining I_{CARS}, further preprocessing is still required in order to interpret the CARS measurements. The CARS interpreting software takes as input the CARS susceptibility, c_{CARS}, which is essentially a property of the substance being probed. The susceptibility is embedded in the actual CARS spectra, I_{CARS}, according to the following relationship (Eckbreth, 1996):

$$I_{CARS} \propto I_{pump}^2 I_{dye} \left| c_{CARS} \right|^2 \tag{4.6}$$

where I_{pump} and I_{dye} are the intensities of the pump and dye lasers, respectively. The variation with wavelength of I_{pump} and I_{dye} is a measurable property of the lasers used in the experiments and is relatively straightforward to determine. On the other hand,

determining the variation of c_{CARS} with wavelength is not straightforward. First, c_{CARS} depends on $w_1 - w_2$, i.e., the difference between the frequencies of the pump and dye beams, respectively. c_{CARS} has nonzero values only when $w_1 - w_2$ equals a Raman Shift frequency, Δw_R, of the molecule of interest. It should also be noted that I_{CARS} intensities have nonzero values only at frequencies w_3 that equal $w_1 + \Delta w_R$. Second, c_{CARS} values are different for different Raman transitions of the molecule of interest and vary with temperature and concentration. Indeed, the measured c_{CARS} values are the basis by which the CARS technique can be used to determine temperature and species concentrations.

In order to extract the CARS susceptibility a dye profile is needed. The dye profile is the intensity distribution as a function of wavelength of the Stokes laser, in particular over the spectral range of the CARS spectra of interest. The dye profile is obtained by taking CARS measurements in a non-resonant gas, i.e., a gas that does not have CARS transitions where the spectra of the species of interest have. Propane was used as the non-resonant gas in this work.

Figure 4.2 shows a typical dye profile of the single Stokes dual dye laser. In order to account for shot-to-shot variations, the dye profile is averaged over several samples. For this reason, the dye profile is not treated for image persistence but only for background noise and detector non-linearity, as follows:

$$I_{dyeProfile} = NonLin(I_{rawDye} - I_{bg}) \qquad \textbf{(4.7)}$$

The CARS susceptibility is then obtained from the CARS spectrum by dividing the dye profile into the CARS spectra and taking the square root of the result as in the

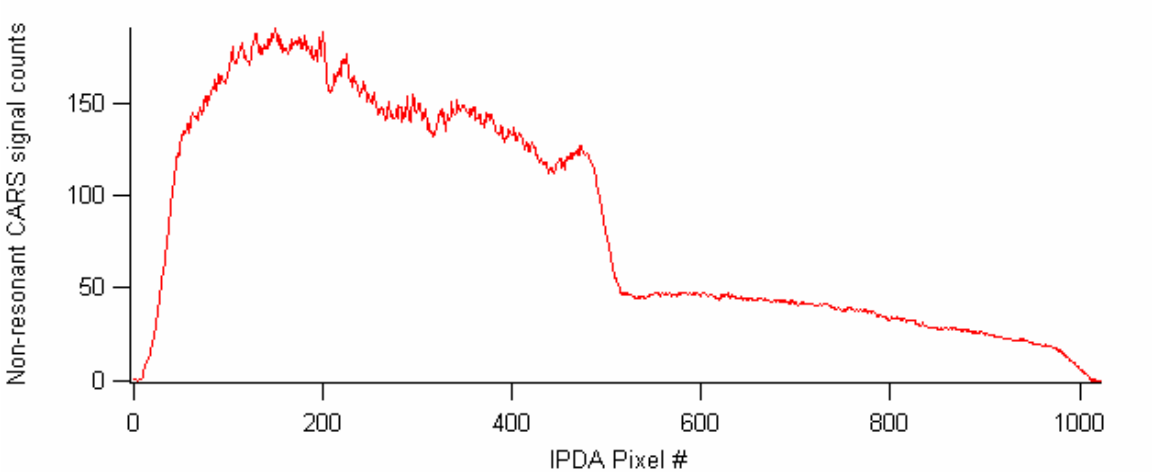

Figure 4.2. A sample dye profile from the BYU single Stokes dual dye CARS instrument.

following equation:

$$c_{CARS} \propto \sqrt{I_{CARS} / I_{dyeProfile}} \tag{4.8}$$

Equation 4.8 assumes that I_{pump} is exactly monochromatic and therefore a constant. In reality, however, lasers do have a finite but very narrow spectral width, which is usually accounted for in the theoretical calculations to obtain accurate CARS spectra interpretations (see the "Pump Laser Dependency"). However, even in this case, Equation 4.8 still represents the final numerical manipulation to be performed on the experimental spectra prior to computational analysis to obtain the temperature and concentration information from the CARS measurement.

4.2 Accounting for Other Instrumental Dependencies

A CARS spectrum is composed of several peaks of varying intensity at different wavelengths that originate from each of the rotational and vibrational quantum states that are populated in the molecule at the time of measurement. Figure 4.3a shows the

theoretical CARS spectrum of the N_2 at ambient conditions (295 K, 0.85 atm) calculated using the program CARSFT (Palmer, 1989). On the other hand, the spectra recorded by the BYU CARS instrument do not show the level of detail of a theoretical spectrum; instead, each species spectrum is smoothed out into a continuous curve as shown in the measured N_2 CARS spectrum in Figure 4.3b. The spectrum is smoothed out due to a quantifiable convolution that depends on the specific characteristics of both the spectrometer and the pump laser, as described in this section.

4.2.1 Spectrometer Dependencies

Two spectrometer characteristics need to be factored into the analysis of the CARS spectra: the spectral dispersion over the IPDA and the instrument function. Both characteristics are closely related to each other and are key factors in the final shape a CARS spectra will have when recorded.

4.2.1.1 Spectral Dispersion

The spectral dispersion is the distribution of light wavelengths focused over the IPDA pixels and consequently is a measure of the spectrometer resolution. The spectral dispersion is determined by the holographic grating inside the spectrometer. The spectral dispersion varies linearly with the distance across the IPDA. Because the pixel centers are equidistant throughout the IPDA, the distance can be expressed directly in terms of pixel numbers. Thus, the following expression was used to obtain the spectral dispersion in terms of wavelength:

$$l_i = \left(\frac{l_2 - l_1}{P_2 - P_1} \right) (P_i - P_1) + l_1 \qquad \textbf{(4.9)}$$

where l_i is the wavelength in nm reaching the ith IPDA pixel P_i (ranging from 1 to

a) Theoretical N_2 CARS spectrum

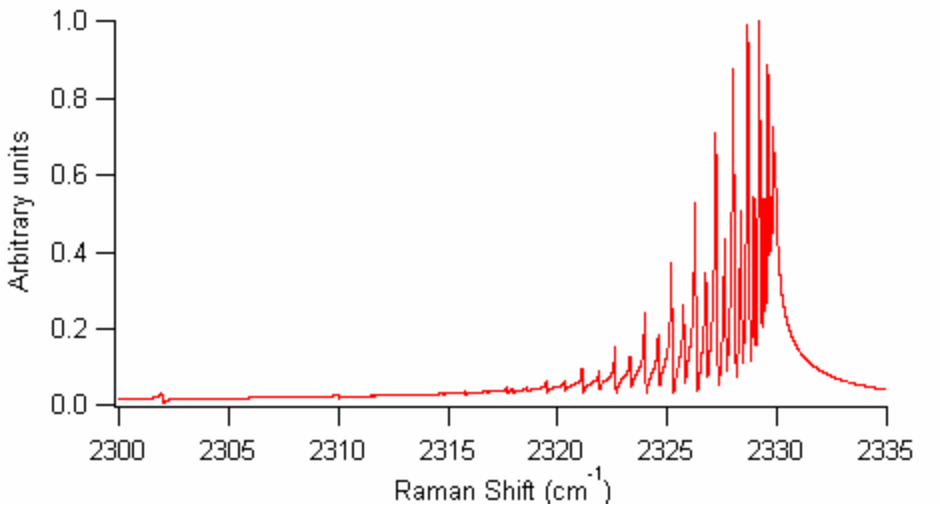

b) An experimental N_2 CARS spectrum

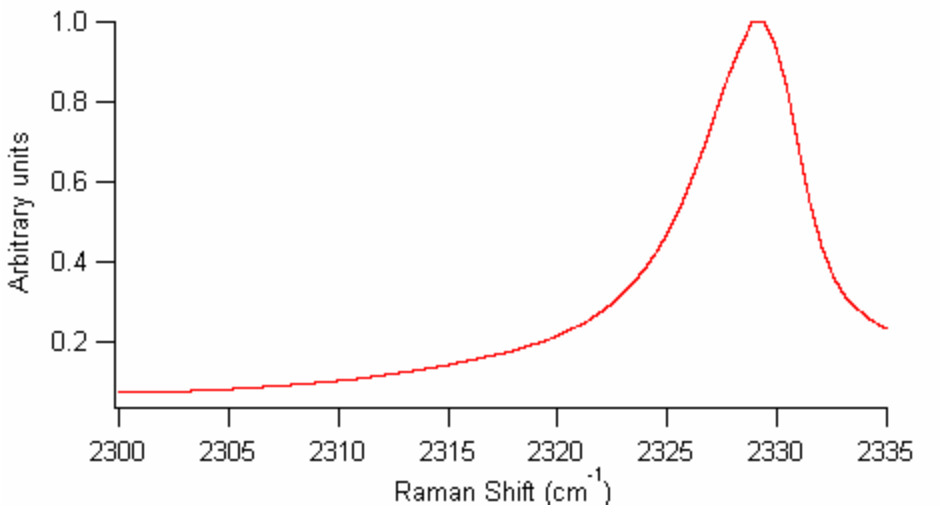

Figure 4.3. A comparison of theoretical and experimental CARS spectra.

1024). P_1 and P_2 are the pixel numbers receiving light at two known wavelength values, l_1 and l_2. These four parameters need to be obtained experimentally.

The spectrometer used in this work was set up to capture two separate wavelength regions. The spectral range for the CARS signals of O_2/CO_2 is focused over one half of

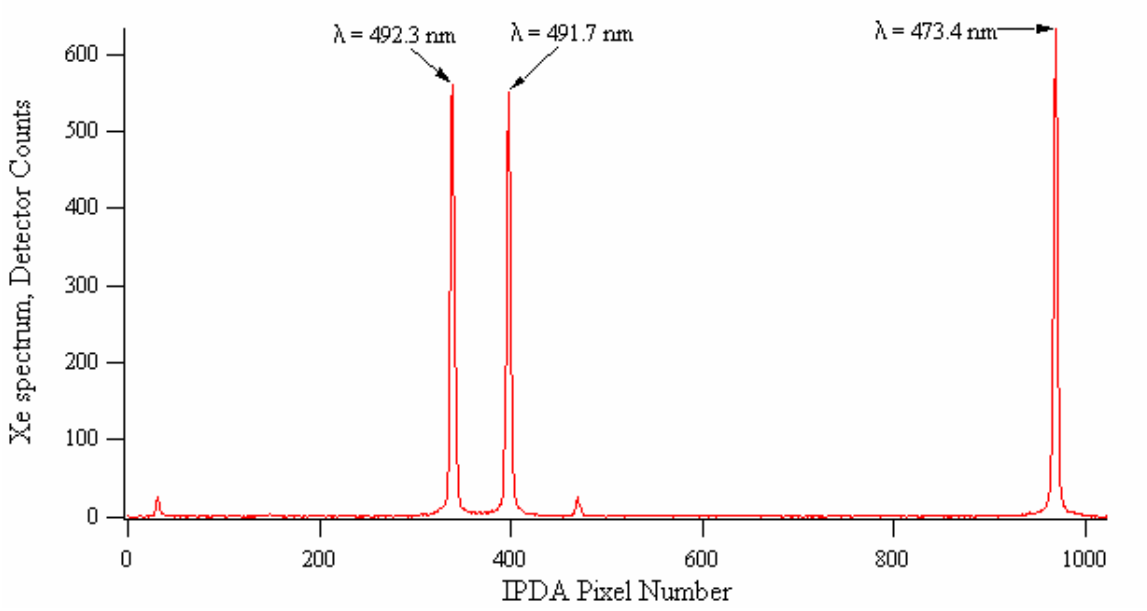

Figure 4.4. Xenon spectrum obtained by the spectrometer used in this research.

the IPDA whereas that for N_2/CO is focused over the other half of the IPDA. Therefore, two spectral dispersions are needed to characterize both sides of the IPDA.

In this work, these spectral dispersions were obtained by measuring the spectrum of a Xe lamp, which has well-defined spectral peaks at known wavelengths over the spectral range of interest (see Figure 4.4). The spectral dispersion over the O_2/CO_2 side is obtained from the two contiguous peaks at 492.3 and 491.7 nm. The dispersion over the N_2/CO side is obtained using the Xe peaks at 473.4 and 469.7 nm. The Xe peak at 469.7 nm (not shown in Figure 4.4) is about 311 pixels to the right of the 473.4 nm peak. The separation distance between the 469.7 nm Xe spectral peak and that at 473.4 nm was measured experimentally by slightly tilting the spectrometer grating to image these peaks over the IPDA. After this measurement was performed, the grating was tilted back to the operating configuration in which the 469.7 nm Xe peak is outside the IPDA range.

The next step was to express the spectral dispersion in terms of the Raman shift in wavenumbers, cm^{-1}, the units used in the CARS interpreting codes. The Raman shift calculated for each pixel is the difference between the frequency corresponding to the wavelength detected by a given pixel (ω_3 from the CARS signal) and the frequency of the pump beams (ω_1). Because $w = c/l$, where c is the speed of light, the Raman shift for each pixel over the IPDA was calculated in terms of the wavelength the pixel detects as follows:

$$\Delta w_{R,i} = (1/l_i - 1/532) * 10^7 \qquad \textbf{(4.10)}$$

where $\Delta w_{R,i}$ is the Raman Shift in cm^{-1} at the ith pixel and 532 is the frequency of the pump beams in nm.

4.2.1.2 Instrument Function

The other spectrometer dependency that needs to be accounted for is the instrument function, which quantifies how the spectrometer records light at each wavelength. To illustrate, suppose that a source of monochromatic light of frequency ω_0 is available. Ideally, a spectrometer would measure this monochromatic light as having an intensity value Iw_0 only at the frequency ω_0,, i.e., an infinitely narrow line. However, because of the wavelength nature of light, any spectrometer will record the monochromatic light as having a distribution of intensities around ω_0, with the maximum intensity value Iw_0. If the spectrometer instrument function were a symmetric Gaussian type, the spectrometer would broaden the line of the monochromatic light, giving it a "line shape" that would look like that in Figure 4.5.

In the field of spectroscopy, it is customary to characterize any symmetric line shape

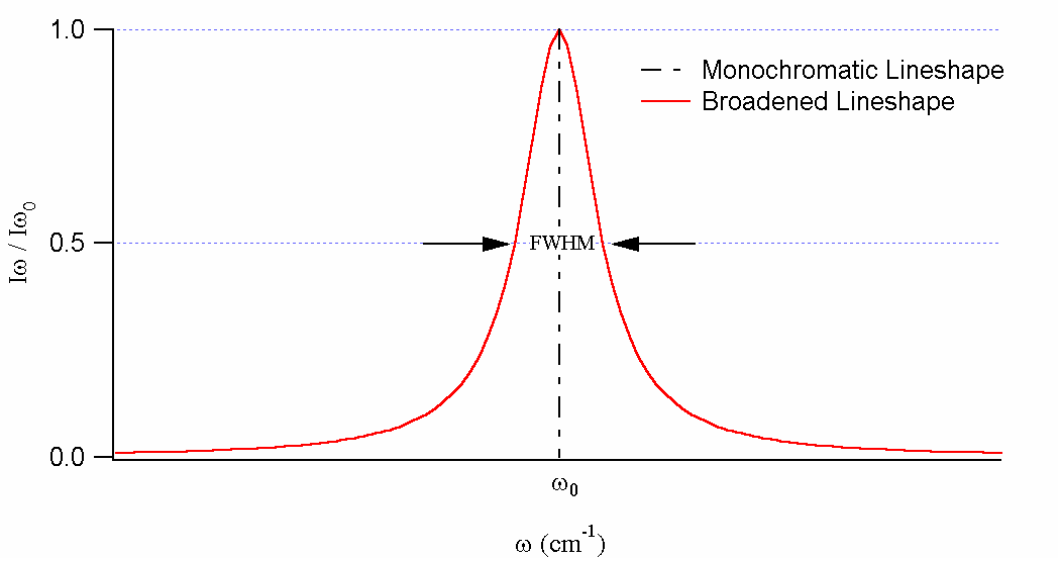

Figure 4.5. Broadening of a monochromatic line by a spectrometer having a symmetric Gaussian instrument function.

of intensity by its FWHM ("Full Width at Half Maximum"), i.e., the total width of the line shape at half the value of the maximum intensity. FWHM is usually expressed in units of cm^{-1}, obtained by dividing the frequency by the value of the speed of light. It should be noted that a spectrometer would broaden in the same way light at any other frequency near ω_0. In general, this line broadening will be different for different spectrometers, hence, the term "instrument function".

The instrument function of a spectrometer depends on several factors, such as diffraction effects, alignment of the spectrometer's optical components and any image distortions originating from manufacturing quality. For the spectrometer used in this research, additional factors affecting the instrument function include the diameter of the fiber optic inside the spectrometer, the width and location of each pixel of the IPDA. In this case, the instrument function can be assumed constant only within a relatively narrow spectral range, such as the range in which the CARS signature of one species is found.

Therefore, the spectrometer used in this work requires four different instrument functions—one each for N_2, CO, CO_2 and O_2.

The instrument function could be measured using monochromatic light, such as from a laser possessing a very narrow spectral width. This procedure would require using four monochromatic lights—each light within the wavelength range of a given species. However, this was not a practical alternative in this research because not even one such light source was readily available. Instead, all instrument functions were calculated based on the following approximation to the Voigt function developed by Whiting (1968):

$$\begin{aligned}\frac{Iw}{Iw_0} = {} & \left(1-\Delta w_l/\Delta w_v\right)*e^{-2.772*\left(\frac{w-w_0}{\Delta w_v}\right)^2} \\ & + \quad \left(\Delta w_l/\Delta w_v\right)*\frac{1}{1+4*\left(w-w_0/\Delta w_v\right)^2} \\ & + \quad 0.016*\left(1-\Delta w_l/\Delta w_v\right)*\left(\Delta w_l/\Delta w_v\right)* \\ & \qquad \left(e^{-0.4*\left|\frac{w-w_0}{\Delta w_v}\right|^{2.25}} - 10\Big/\left(10+\left|\frac{w-w_0}{\Delta w_v}\right|^{2.25}\right)\right)\end{aligned} \qquad \textbf{(4.11)}$$

where Iw_0 is the light intensity at the actual frequency w_0 in cm^{-1} and Iw is the light intensity at the frequency w at either side of w_0. Whiting's approximation uses a weighted average of Gaussian and Lorentzian lineshapes (see the first and second terms, respectively, on the right side of Equation 4.11). The equation has two fitting parameters, which describe the Voigt function of a given spectrometer: 1) the Lorentzian FWHM, Δw_l, 2) and the Voigt FWHM, Δw_v. Thus, a Voigt instrument function is fully specified by the two values, Δw_l and Δw_v, both measured in cm^{-1}.

Figure 4.6 shows the N_2 instrument function for the spectrometer used in this work.

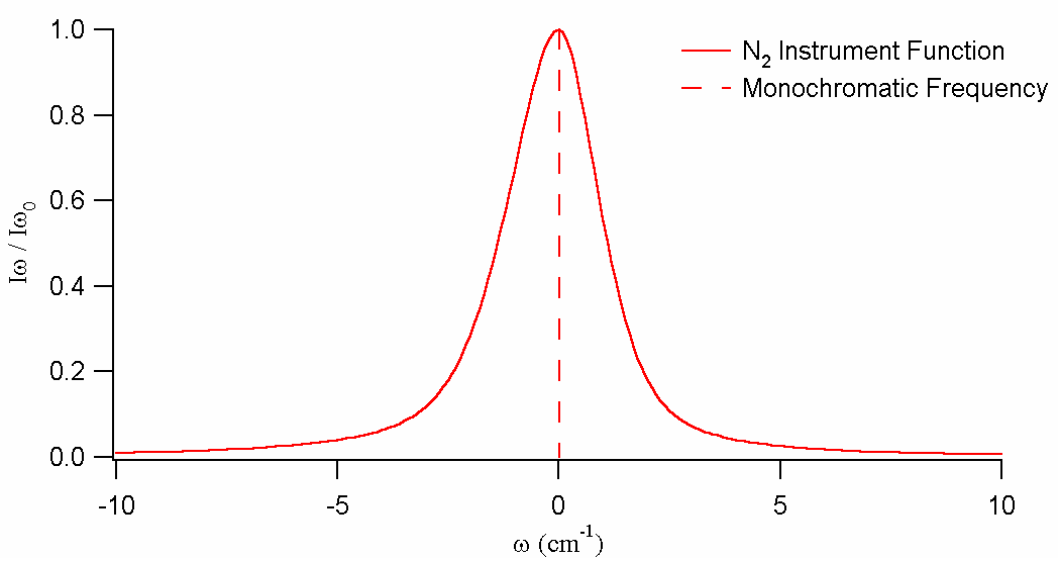

Figure 4.6. The asymmetric N_2 instrument function calculated for the spectrometer used in this research.

This is the predicted line shape and width any monochromatic light would appear to have when measured by the spectrometer of this work in the N_2 CARS spectral range. The frequency in the abscissa is relative to the frequency of interest, i.e., the light at a specific wavelength. The value of w_0 was arbitrarily set equal to zero in the calculations because what is needed is the variation in intensity away from any central frequency since the same instrument function is used throughout the spectral range of the species CARS signature.

The line shape of the N_2 instrument function is slightly asymmetric, and was modeled by using two Voigt functions, one for the left side of the line shape and another for the right side (see Table 4.1). Thus, two different sets of values of Δw_l and Δw_v are required to specify the instrument function of N_2, one set for the left side of the line shape

(i.e., $w < 0$), and the other for the right side (i.e., $w > 0$). The instrument function for the other species is also asymmetric (Boyack, 1990).

Table 4.1 shows the Lorentzian and Voigt widths obtained in this work for N_2, CO_2, and O_2. The instrument function for CO was not calculated because it was not needed for this research. The values in this work differ from those reported by Boyack (see also Table 4.1) because of differences in alignment within the spectrometer introduced by the use of a new grating and fiber optic. Notice the variation in the instrument function across the IPDA; in particular, notice how the CO_2 instrument function is appreciably wider than the rest, as indicated by the value of its right Voigt width. This may be caused by a slight rotational misalignment in the grating of the spectrometer, which was not corrected because of the risk of damaging the grating.

The sets of Lorentzian and Voigt widths were obtained using the program CARSFT (Palmer, 1989) developed at Sandia National Laboratories to fit CARS spectra measured in gas samples of known composition at ambient conditions. This was accomplished by

Table 4.1. Voigt and Lorentzian widths for the asymmetric instrument functions of N_2, O_2 and CO_2 in the spectrograph used in this work

		This Work			**Boyack (1990)**		
Species / **Widths (cm^{-1})**		**N_2**	**O_2**	**CO_2**	**N_2**	**O_2**	**CO_2**
LEFT	Δw_l	1.65	1.55	1.17	1.1	1.0	Not Specified
	Δw_v	2.76	2.15	1.96	1.7	1.0	Not Specified
RIGHT	Δw_l	1.34	1.27	1.48	1.2	1.0	Not Specified
	Δw_v	2.21	1.55	6.46	2.2	2.2	Not Specified

adding the asymmetric Voigt approximation to the set of analytical functions that CARSFT could use in performing such spectral fits. The instrument function was calculated from 0 to 75 cm^{-1} on each side of the line shape, in increments of 0.1 cm^{-1}. The FORTRAN code used in implementing the approximation to the Voigt function is included in Appendix B.

4.2.2 Pump Laser Dependency

The pump laser dependency to be taken into account is the spectral linewidth of the pump laser itself. The light coming out of our Nd:YAG laser is not exactly monochromatic but has an intensity distribution centered at 1064 nm, which results in an intensity distribution centered at 532 nm on the pump laser obtained by frequency doubling in the Harmonic Generators. Boyack (1990) reported a pump laser linewidth, FHWM, of 0.51 ± 0.7 cm^{-1} centered at 532 nm. In this work, the pump laser linewidth has been assumed to be the same reported by Boyack because the same Nd:YAG and harmonic generators were used.

The effect of the pump laser linewidth on the CARS signal can be qualitatively explained by considering the basic requirement to generate a CARS signal for a given molecular transition: the difference between the frequencies of the pump and Stokes lasers, $w_1 - w_2$, must match the Raman shift $\Delta w_{R,i}$ for that transition. Thus, when having a broadband Stokes laser and a pump laser of finite spectral width, the CARS intensity at each transition results from the all the contributions of each combination of pump and dye laser frequencies differing by the same Raman Stokes shift.

Taking into account the effects of both the instrument function and pump laser widths in CARS spectra is not a straightforward matter. The pump laser widths can be

accounted for by using either a single (Yuratich, 1979) or a double convolution method (Teets, 1984; Kataoka, et al., 1982). The latter was the method used in this work. Additional details on this subject can be found in the CARSFT documentation and elsewhere in the literature (Palmer, 1989).

4.3 Fitting Methodology

The software used in this work to interpret the CARS spectra is based on a model proposed by Hall and Boedeker (1984) to fit a theoretical CARS susceptibility $c_{CARS,\ theory}$ to its experimental counterpart c_{CARS} by using temperature and mole fractions as fitting parameters. The model assumes that the resonant components of $c_{CARS,\ theory}$ (Eckbreth, 1996) are dependent on temperature only, and that its total nonresonant susceptibility component, c_{NR}, depends only on the mole fractions x_i of the mixture components. Thus, the modulus squared of $c_{CARS,\ theory}$ for species i can be expressed as follows:

$$\left|c_{CARS,\ theory}\right|^2 \propto \left[\left(\frac{x_i}{c_{NR}}\right)^2 \cdot g(w_{CARS},T) + 2\cdot\left(\frac{x_i}{c_{NR}}\right)\cdot f(w_{CARS},T) + e(w_{CARS})\right] \qquad \textbf{(4.12)}$$

where the functions g and f are convolution functions of the resonant components of $c_{CARS,\ theory}$ that include the effects of pump laser spectral width and the instrument function. For broadband Stokes lasers, as is the case in this work, $e(w_{CARS})$ is equal to 1 (Hall and Boedeker, 1984).

Equation 4.12 indicates that experimental CARS spectra can be interpreted by fitting two parameters, namely, the gas temperature T and the ratio (x_i / c_{NR}). The only requirement is to preprocess the experimental CARS spectra as previously indicated (see Equations 3.1 through 3.8). The g and f curves are calculated just once for several temperature values and stored as a set of fitting libraries in a computer hard drive. These fitting libraries are then used to calculate the theoretical CARS spectra by interpolation during the fitting process to interpret the experimental CARS spectra. This method is various orders of magnitude faster to process experimental CARS spectra than the method of using the detailed CARS spectra calculations (Hall and Boedeker, 1984). The accuracy of the interpolated functions depends on the interpolation scheme, the proximity of the temperature values of the g and f curves used for the interpolation, and the mole fraction values of the species of interest in the sample.

It is important to note that the Sandia developers implemented Hall and Baedeker's method in a manner that their library fitting code, FTCARS, uses (c_{NR} / x_i), i.e., the inverse of the parameter shown in Equation 4.12. In this work, the program CARSFT was used to calculate the libraries used by FTCARS for the temperature range of 250 to 2050 K and in increments of 50 K for N_2, O_2, and CO_2. The upper temperature limit was intentionally set just above the highest adiabatic temperature of the combustion conditions to be studied. Thus, it is ensured that the CARS fitting methodology was not bound artificially to only give "reasonable" temperature values.

The instrument functions for each species shown in Table 4.1 were used to generate their corresponding libraries. These libraries were used to reduce all the data acquired in this research because the instrument function was found to have remained practically

constant throughout the data acquisition period (about three months). This was verified by using CARS measurements taken on calibration samples for each day that combustion experiments were performed. The instrument functions were calculated for each daily sample, showing minor variations. This was particularly true for N_2, as confirmed by the fact that the CARS temperatures obtained using the libraries just mentioned were, within experimental error, equal to the known temperature values of the daily calibration samples. Appendix D shows the listing of the input parameters used to calculate the libraries using CARSFT.

The CARS spectra curve-fitting procedure used in this work is that of the program FTCARS from Sandia National Laboratories (see more details below). The temperature and the ratio (c_{NR}/x_i) are the main fitting parameters in a heuristic curve-fitting methodology to minimize the least squares between the $c_{CARS,\ theory}$ (obtained by linear interpolation of the g and f curves) and its experimental counterpart c_{CARS} (obtained by pre-processing the experimental CARS measurement).

4.3.1 Computation of Concentrations and Temperature

In principle, the same temperature value should be calculated independently from N_2, O_2, and CO_2 (Eckbreth, 1996). However, in practice, the accuracy of the temperature value depends on the accuracy of the CARS spectral characteristics, such as transition frequency and line width, for any given species. Among the species under consideration, N_2 is the best source of temperature measurements because its spectral characteristics are very well established. In addition, N_2 is the most abundant species in the combustion

experiments carried out in this work (more than 70 mol-%). Therefore, the gas temperature for each multi-species CARS sample was taken from the N_2 CARS signal.

As mentioned previously, the CARS interpreting technique calculates the ratio (c_{NR}/x_i). If the CARS measurement includes all species in a mixture, the mole fractions can be calculated from the (c_{NR}/x_i) ratios and the relationship $\sum_i x_i = 1$. Otherwise, it is necessary to know either the mole fraction of one of the species or the value of the total nonresonant susceptibility of the mixture c_{NR}, which is a mole-fraction weighted average of the per-molecule nonresonant susceptibilities of the individual mixture components $c_{NR,i}$, as follows:

$$c_{NR} = \sum_i \left(x_i * c_{NR,i}\right) \qquad \textbf{(4.13)}$$

For the combustion experiments carried out in this work, the abundant quantities of N_2 could provide a simple method of calculating c_{NR}. Mass balances show that the mole fraction of N_2 remains practically constant from unreacted mixture through total fuel depletion for the combustion conditions of interest in this work—approximately at 74 mol-% for ϕ of 0.80 and at 73 mol-% for ϕ of 0.65. The concentrations of CO and nitrogen oxides were neglected in the mass balances because they occur in the ppm range for the combustion conditions in this work (e.g., see Nguyen, et al., 1995; Nandula, et al., 1996; Cannon, et al., 1999). Therefore, c_{NR} can be calculated from the N_2 CARS mole fraction and the ratio (x_{N2}/c_{NR}) obtained from the N_2 CARS spectra. The CO_2 and O_2 mole fractions follow immediately from the (x_{O2}/c_{NR}) and (x_{CO2}/c_{NR}) ratios obtained from their respective CARS spectra.

4.4 Software Developed in This Work

The CARS spectra interpretation procedure is complex and is compounded even further when large amounts of data are involved. In this research project, more than one million multi-species CARS spectra were taken throughout several locations in the LSGTC for varying combustion conditions, making it essential to devise a means to order and structure the information.

In this work, a data management system was devised that simplified, automated, and ensured the proper processing of CARS data through the stages of data acquisition, interpretation and recording of temperature and species concentrations, and statistical analysis. The data management system, detailed in Appendix D, starts being implemented through Igor (Wavemetrics, Inc.) macros programmed to automatically name the data files stored by the CARS instrument computer in a way that identified the combustion condition and sampling location where the data were taken.

In addition, a program to Fit Multiple-species Cars Spectra (FMCARS) was written and used to interpret the spectra taken in this work. FMCARS uses the CARS spectra interpretation subroutines of the FTCARS program, which accompanies CARSFT (Palmer, 1989), from Sandia National Laboratories. The FTCARS program was not used in this research because its interface was not suitable for processing the large number of acquired measurements. Based on benchmark studies using Hewlett-Packard 780/J-282 UNIX workstations, it would have taken a few years of computer time to process all the data, plus the time required to prepare the spectra for interpretation by FTCARS and obtain the desired mole fraction values from the output of FTCARS. On the other hand, FMCARS can process all the data acquired in this research and output desired parameter

values in less than 90 hours of computer time. This considerable reduction in time requirements was achieved mainly because of an automated and more efficient processing scheme built into FMCARS.

FMCARS is compatible with the CARS data management system devised in this work. Appendix B shows a complete listing of the FMCARS code written in this work. The listing does not include the supporting subroutines used by FTCARS to handle graphics output and certain mathematical calculations such as interpolation, array sorting, etc. The FMCARS interface is designed to efficiently process several data files of multi-species (N_2, O_2 and CO_2) CARS spectra specified by the user through a text file. FMCARS is also designed to take appropriate actions upon encountering error conditions of various kinds to ensure continued processing of the specified data files. In the case of the combustion experiments, each file contains all the samples taken at a combustor location under a given combustion condition. For each file, FMCARS reads each multi-species CARS sample in the data files, other required information, handles all preprocessing and CARS spectra interpretation for each species, and outputs a text file containing a tabulation of several measurement parameters on a sample-by-sample basis. The tabulated format facilitates further statistical analysis of the measurement parameters while properly identifying the location and combustion conditions associated with the computed statistics. The parameters of each output file are the temperature, non-resonant susceptibility, O_2 and CO_2 mole fractions, as well as measurements of curve-fit "goodness" and spectrum peak detector counts for each species.

In conclusion, the process of extracting temperatures and concentrations from measured CARS spectra is complex. However, the new software developed in this work

facilitated the analysis of the large numbers of experimental samples collected in this research, while minimizing the risk of human error and making it feasible to reduce all data within a reasonable amount of time. A summary of the data reduction process as implemented in the software developed in this work is found in Figure 4.7.

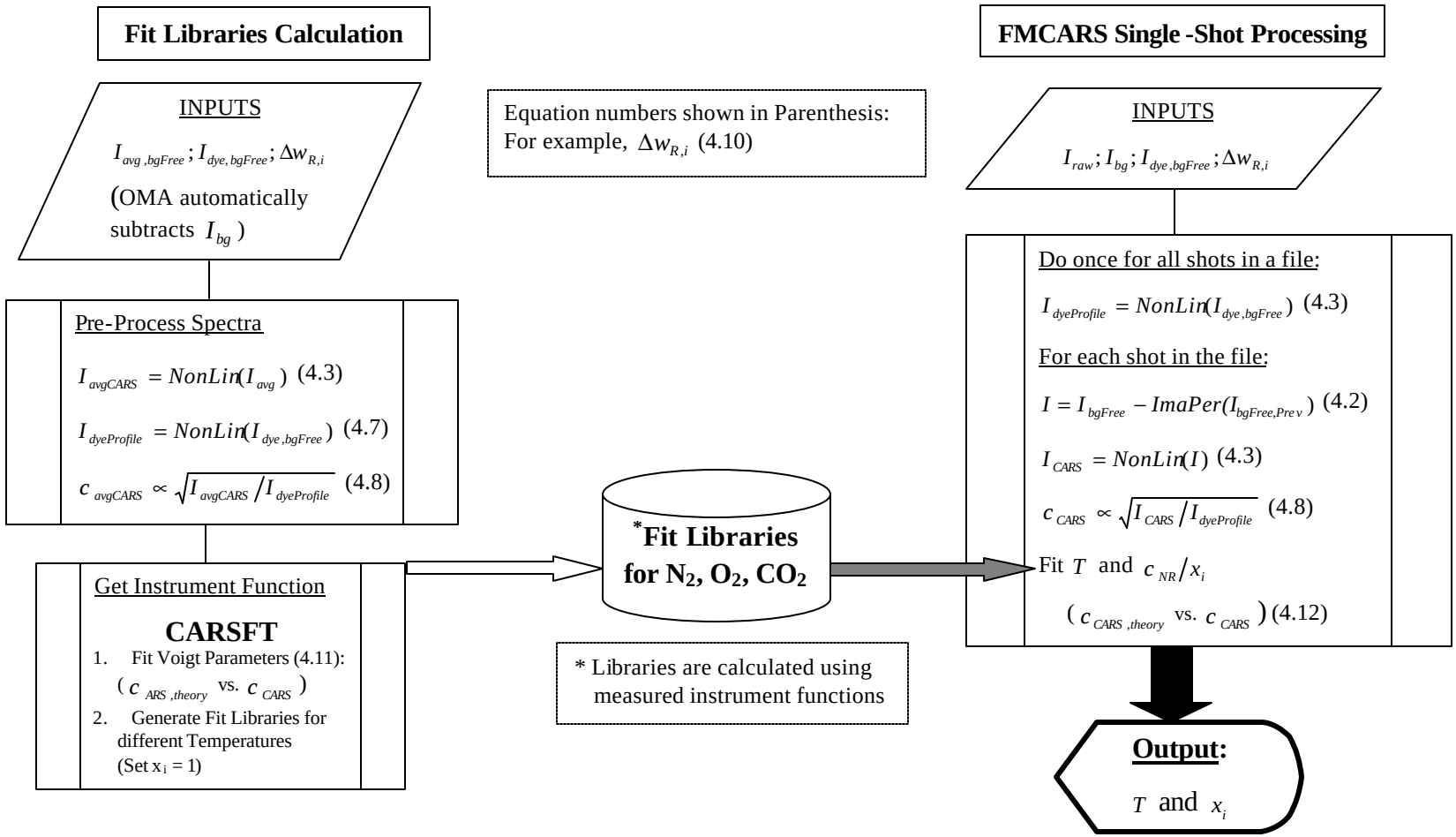

Figure 4.7. Algorithm to calculate temperatures and mole fractions from measured CARS spectra

5. ACCURACY AND PRECISION OF THE BYU SINGLE-STOKES DUAL DYE CARS INSTRUMENT

This chapter describes how the accuracy and precision were estimated for the measurements obtained using the dual dye single-Stokes CARS instrument. This treatment is only presented for the temperatures, and the concentrations of O_2 and CO_2. The accuracy and precision for the CO concentrations was not pursued because the CARS instrument did not detect CO during the combustion experiments due to the CO concentrations being too small to be detected.

5.1 Temperature

The accuracy and precision of the temperatures measured by the single-Stokes CARS instrument was estimated by collecting CARS measurements of air at atmospheric pressure at 12 different temperatures in the range of 294 to 1428 K. For each temperature condition, 1000 CARS samples were collected. The temperature variation was obtained by using an electrically heated tube furnace from Thermodyne (Type 21100). The furnace consisted of a cylindrical cavity two inches in diameter and 14 5/8 inches tall, open to the ambient atmosphere. The furnace temperature readings were obtained using a type K thermocouple, placed in the middle of the cavity and connected to a digital reader (Model DP900) from Omega.

Because the furnace was open to the atmosphere, care was taken to keep any laboratory air streams from entering the furnace during the experiments. In addition, the

CARS measurements were taken only when the furnace temperature reading remained stable for at least two minutes.

As these CARS spectra were reduced, a set of sieving criteria was devised in order to discard those measurements that were definitely bad, i.e., spectra whose signals were severely distorted by noise. These sieving criteria were obtained after careful examination of several CARS spectra. During the examination process, a parameter to indicate the "goodness" of the fit of theory to experiment was found to be useful for sieving out bad data. This parameter is the value of the ratio of the area under the theoretical curve divided by the area under the experimental data curve: $A_{theory}/A_{experim}$. This ratio has the advantage that good fits have $A_{theory}/A_{experim}$ ratios close to unity.

During the statistical analysis of the data, the following constraints were implemented.

1. Discard N_2 measurements where the $A_{theory}/A_{experim}$ ratio was less than 0.98 or greater than 1.2. The upper limit of 1.2 was chosen because some spectra with appreciable experimental noise yielded reasonable temperature values while having a $A_{theory}/A_{experim}$ ratio of 1.2. It should be mentioned, however, that most $A_{theory}/A_{experim}$ values were very close to 1 (see data in the accompanying CD).
2. Discard N_2 measurements where the temperatures were less than 250 K or greater than 2050 K. It should be mentioned that none of the CARS measurements in this validation study had temperature values higher than approximately 1500 K.

3. Discard those spectra whose temperature values were more than four times the standard deviation on either side of the mean CARS temperature.

All the statistical data presented in this work were calculated using only those measurements that passed the aforementioned sieving criteria.

Table 5.1 shows a comparative analysis between the temperatures measured by the furnace thermocouple ($T_{Furnace}$) and the temperatures measured using the BYU single-Stokes dual-dye CARS instrument. The statistics calculated on the CARS measurements include the average temperature ($<T_{CARS}>$) and the standard deviation (σ_{Tcars}) of approximately 900 samples at each temperature. The mean CARS temperatures from this dataset are about 4.6% on average higher than the temperatures obtained by the furnace thermocouple. The fact that all the CARS average temperatures are higher than their thermocouple counterparts may indicate the presence of a small systematic error in either the thermocouple or the CARS measurements.

In order to quantify the precision of the CARS instrument, it was decided to define the instrument error to be twice the value of the standard deviation. The average error from the CARS-measured temperatures was ±15.6% in the temperature range from 294 to 1023 K. On the other hand, the error for the higher temperature range from 1175 to 1428 K was 28.2%, about twice as much as from the lower temperature range.

Figure 5.1 shows an alternate presentation of the data contained in Table 5.1. The empty circles represent the point defined by corresponding pairs of $T_{Furnace}$ and $<T_{CARS}>$. The error bars are $\pm 2*\sigma_{Tcars}$. The dashed line has a slope of one, and therefore represents the line where all ($<T_{CARS}>$) would lay on if they were exactly equal to $T_{Furnace}$. The data discussed herein suggests that the temperature accuracy of the BYU dual dye single

Table 5.1. Comparison CARS temperature measurements and thermocouple readings in a calibration tube furnace.

	CARS-Measured Temperatures (K)			
	AVERAGE		STD. DEVIATION	
$T_{Furnace}$ (K)	$\langle T_{CARS} \rangle$	% Error from $\langle T_{Furnace} \rangle$	σ_{Tcars}	% Uncertainty in $\langle T_{CARS} \rangle$ as $2*\sigma_{Tcars}$
294	310	5.3	25	16.2
473	514	8.6	48	18.8
593	642	8.3	53	16.5
723	759	5.0	51	13.5
873	891	2.0	53	11.8
1023	1022	-0.1	84	16.5
1175	1206	2.6	176	29.3
1323	1419	7.3	218	30.7
1428	1463	2.5	181	24.7

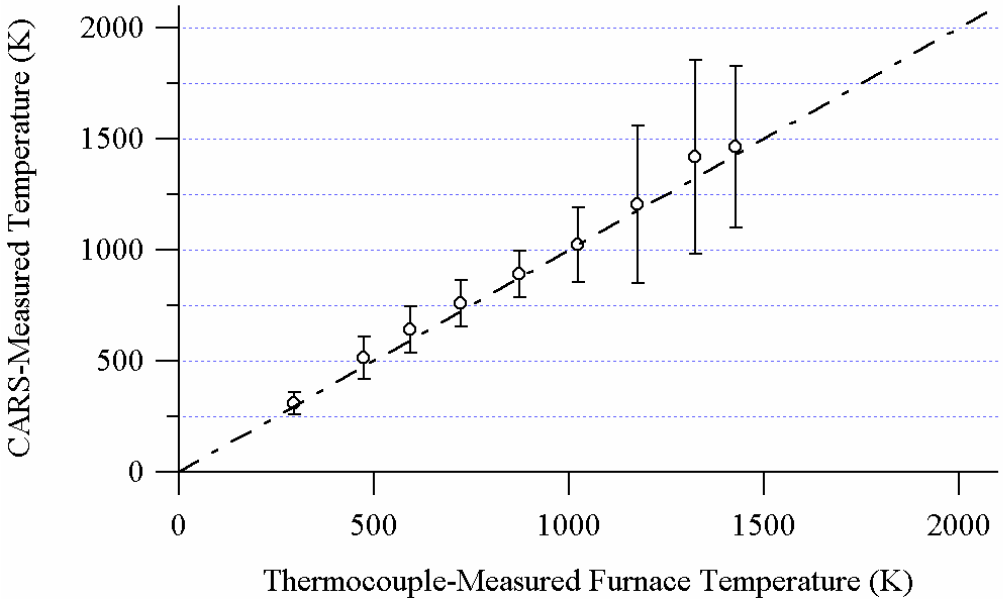

Figure 5.1. CARS-Measured Temperatures vs. Thermocouple values in a calibration tube furnace.

Stokes CARS instrument is good any where between 300 and 1428 K. The data also suggest that the instrument's precision for temperature is acceptable, particularly below 1200 K. For temperatures higher than 1200 K, the data seem to suggest that the instrument's precision is only fair. However, the analysis that follows supports the possibility that the data for the three highest temperature conditions in the furnace are suspect, not due to instrumental limitations, but due to experimental difficulties encountered only in these calibration experiments.

Figure 5.1 shows the probability density function (or PDF) for each of the temperature conditions measured in the furnace. Each PDF was calculated after sieving the corresponding 1000 CARS samples, as specified previously. The temperature value found in the legend box inside each graph is the thermocouple temperature, $T_{Furnace}$. Note that the temperature distribution at 294 K is almost a straight line, showing that variations from the mean are not very significant at this condition. For the temperatures between 473 and 1023 K, the probability density functions of temperature follow a normal distribution. However, the probability density functions for 1175, 1323, and 1428 K do not follow a normal distribution. Instead, their distributions consistently follow the same pattern, having a stretched tail down to lower temperatures.

It is possible that the lower temperature values resulted from "faint" CARS samples, i.e., those with very low detector counts. In those cases, a CARS spectrum could be significantly distorted, or even worse, not detected at all, resulting in lower temperatures than actually measured. In order to substantiate this idea, the FMCARS output files for the three temperature conditions in question were analyzed. The analysis focused on the following values obtained from each individual N_2 spectrum: 1) the fitted temperature

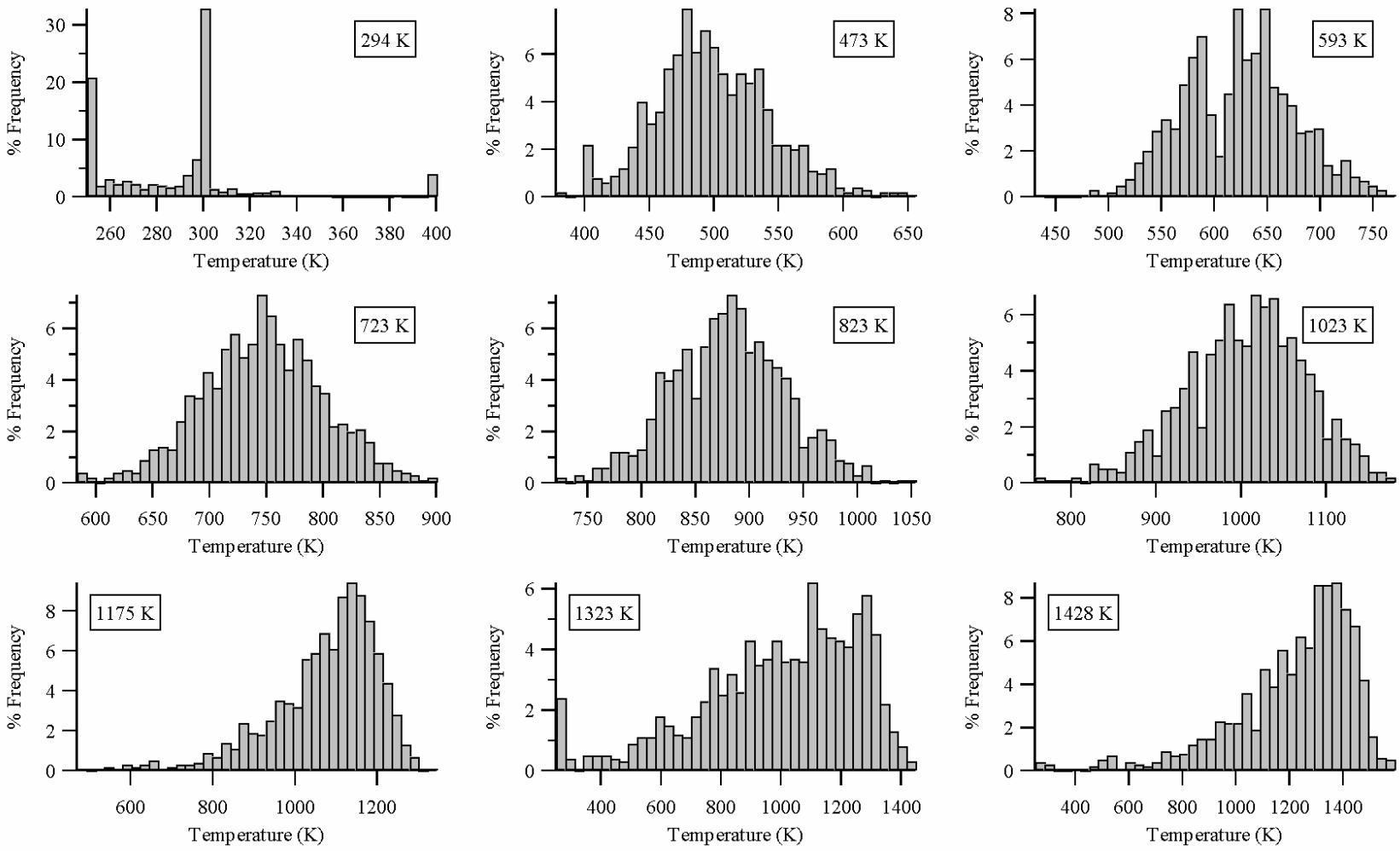

Figure 5.2. PDFs of gas temperature (K) measured in air using the BYU single Stokes instrument.

value, and 2) the "peak detector counts", i.e., the value of the maximum number of counts recorded by the detector for the given spectrum. Using Microsoft Excel, new average and standard deviations were calculated by including only those spectra with peak detector counts greater than or equal to 80. This number was empirically chosen after visual inspection of several FMCARS fits of CARS N_2 spectra having a wide range of peak detector counts.

Table 5.2 shows the $<T_{CARS}>$ and σ_{Tcars} obtained when discarding all N_2 spectra with peak counts less than 80. The average temperatures did not change significantly. On the other hand, the standard deviations were reduced by about a third from the values reported in Table 5.1 resulting in an average error of 13.8% for the three temperature conditions. Note that a significant number of CARS samples had peak counts less than 80, for example, 60% of the samples taken at 1428 K were discarded based on this criterion.

This analysis provides evidence that supports the idea that large errors reported at temperatures greater than 1200 K do not necessarily reflect the precision of the instrument, but rather may be caused by experimental difficulties in obtaining strong

Table 5.2. Empirically corrected CARS temperature measurements vs. thermocouple readings in a calibration tube furnace.

	CARS-Measured Temperatures (K)				
	AVERAGE		**STD. DEVIATION**		**# of Kept Shots**
$T_{Furnace}$ (K)	$<T_{CARS}>$	% Error from $<T_{Furnace}>$	σ_{Tcars}	% Uncertainty in $<T_{CARS}>$ as $2*\sigma_{Tcars}$	
1175	1118	-4.8	88	15.0	728
1323	1249	-5.6	93	14.0	237
1428	1373	-3.9	89	12.5	400

enough CARS signals. Possible sources of these experimental difficulties include, but may not be limited to, the following: (1) loss in dye laser power due to random intensity and dye profile variations, and (2) misalignment of the pump and dye lasers due to the intense heat originating from the tube furnace that introduced slight expansion in the focusing lenses. It is believed that the latter was the most important factor because the focusing lenses were not shielded during these experiments due to the tube furnace size, and because the lasers had to be realigned every time the CARS sampling was started for each of the high temperature cases due to loss of CARS signal intensity.

The aforementioned analysis raises the question whether the CARS spectra whose peak counts are less than 80 should be discarded during the analysis of the combustion cases investigated in this work. However, this approach was decided against because of its potential negative impact in the analysis of samples taken in flame regions with very large temperature variations. For example, several valid samples might be discarded in regions where intense turbulent mixing of hot and cold gases with large temperature differences occurs—a situation that was observed in several locations for all combustion cases during the experiments. In these cases, the CARS instrument power had to be low enough to not ionize the cold gases, yet high enough to detect the hotter ones. Thus, hot gases may end up yielding lower-count spectra that are still of good quality and can give valid information.

Based on the preceding analysis, it is postulated that the actual uncertainty in the temperature data collected in the combustion experiments of this research is about ±15%, throughout all the temperature range, because the CARS instrument optics were adequately shielded from the heat released by the combustion system under study.

5.2 O_2 Concentrations

The accuracy and precision of the O_2 measurements for the new BYU CARS instrument were studied using the data collected in the same experiments used for the temperature analysis. These O_2 spectra were also sieved according to the following criteria:

1. Discard O_2 spectra whose companion N_2 spectra were discarded in the temperature analysis.
2. Discard the O_2 measurements where the ratio $A_{theory}/A_{experim}$ was less than 0.98 or greater than 1.2. The upper limit was chosen to be consistent with the N_2 sieving criteria.
3. Discard those spectra whose O_2 mole fractions were more than four times the standard deviation at either side of the mean.
4. Any N_2 spectrum meeting the sieving criteria described in section 1 of this chapter was kept even if its companion O_2 spectrum was discarded because the temperature value from the N_2 spectrum is still valid.

The temperature value for each O_2 spectrum was set to be the temperature value of its companion N_2 spectrum. In addition, FMCARS was modified to output the concentrations ratio x_{O2}/x_{N2} from the companion fit parameters x_{O2}/c_{NR} and x_{N2}/c_{NR} for each CARS sample. Thus, the N_2 and O_2 mole fractions can be calculated directly in these validation experiments by neglecting the other minor components in ambient air, i.e., assuming that $x_{O2} + x_{N2} = 1$.

Table 5.3 shows the average and standard deviations obtained for the sieved O_2 CARS calibration samples at each temperature condition. Also shown are the % error

Table 5.3. CARS O_2 concentration measurements in a calibration tube furnace. Air was used in the furnace; therefore, the actual O_2 mole fraction was 0.21.

	CARS-Measured O_2 mole fractions			
	AVERAGE		STD. DEVIATION	
$T_{Furnace}$ (K)	$<X_{O2}>$	% Error from 0.21 (X_{O2} in air)	σ_{XO2}	% Uncertainty as $2*\sigma_{XO2}$
294	0.207	-1.6	0.033	32.3
473	0.201	-4.4	0.026	25.5
593	0.192	-8.6	0.026	26.8
723	0.184	-12.6	0.025	27.2
873	0.178	-15.1	0.023	26.0
1023	0.178	-15.3	0.028	31.9
1175	0.194	-7.9	0.046	47.7
1323	0.261	24.3	0.081	62.1
1428	0.235	12.0	0.074	62.7

and the % uncertainty. The % error is a measure of the accuracy of the CARS instrument and was defined as the % difference between the measured average mole, $<X_{O2}>$, and 0.21, the mole fraction of O_2 in air. From 294 to 1023 K, the $<X_{O2}>$ values are slightly lower than the actual O_2 concentration. In this temperature range, the % error increased with temperature from 1.6% at 294 K to about 15% at 1023 K. For the three highest temperatures, there is no apparent trend in the variation of % error. However, with the exception of the data at 1323 K, the % error is still within 15%.

The % uncertainty (shown in Table 5.3) is a measure of the precision of the BYU single-Stokes CARS instrument and was defined as ± two times the standard deviation of $<X_{O2}>$ expressed as a percent error. From 294 to 1023 K, the uncertainty in the concentration is about 30% higher or lower than the measured value. For the three highest temperatures, the uncertainty is even higher—about 60%. The calibration measurements show that the lowest uncertainty is ± 0.05 mole fraction, a total error bar

of 0.1 mole fraction. The uncertainty encompasses about two-thirds of the range of O_2 concentrations expected in the combustor (0.19 down to 0.05). It should be pointed out that the uncertainties are expected to increase for lower O_2 mole fraction due to the interference of the resonant components of other species present in the mixture. In conclusion, the uncertainty in O_2 concentrations is large enough to say that this implementation is not well suited for the combustor.

Two potential sources have been identified to explain the large concentration uncertainties, and possible solutions are proposed. The verification and implementation of these solutions are beyond the scope of this work, but they are thought to be worthy of pursuit in future research.

The foremost potential source of uncertainty in O_2 concentrations is an inherent limitation in the approximate CARS interpretation method of Hall and Boedeker. This method has been shown to give large errors in the mole fractions in mixtures where there are large concentrations of species other than the one being measured (Palmer, 1989; Hall and Boedeker, 1984), as is the case in both (a) these O_2 measurements and (b) in the combustion experiments, where N_2 accounts for more than 70% of the mixture.

These problems could be avoided by analyzing the CARS spectra using the complete numerical computations found in CARSFT. If it can be shown that there is significant improvement in the concentration values when using CARSFT, one could modify FMCARS to use the CARSFT subroutines instead of the library-based procedure of FTCARS, which uses Hall and Baedeker's method. This would be a very involved and potentially time consuming effort. In addition, the resulting code is expected to be very computationally intensive. Its application to reducing the large amount of experimental

data obtained in this work may be prohibitive with current computer technology. Another alternative to consider is developing another simplification to the CARS computations that is fit for multi-species concentration measurements. Again, both approaches to enhancing the accuracy of obtaining species concentrations from the CARS measurements are beyond the scope of this work.

The second potential source of the large concentration uncertainty is the random variations in the dye profile of the BYU single-Stokes CARS instrument. The dye profile variations arise naturally as part of the dye laser generation process and their effects in single-pulse precision are very complicated to quantify (Eckbreth, 1996). It should be noted that the FTCARS algorithm already includes a correction procedure suggested by Snelling (1987) applicable when using an averaged dye profile. This limitation is inherent to the instrument and can only be addressed by finding either new dyes or dye laser generation methods with more repeatable laser output.

In conclusion, the large uncertainty of the measurements in the controlled tube furnace environment raise questions as to the suitability of the new BYU CARS instrument to measure the O_2 concentrations in the turbulent environment of the combustion cases studied in this work. Because the uncertainties are so large and are expected to increase for low concentration ranges of O_2, it would not be clear whether any observed variations of O_2 concentrations were caused by the flame turbulence or were an artifact of either the reduction method or the instrument itself. Thus, the analysis of the O_2 concentrations of the combustion cases has been deferred to future work.

5.3 CO_2 Concentrations

Separate experiments were carried out to determine the BYU CARS instrument accuracy and precision for the CO_2 measurements. A vendor-prepared mixture of 10 mol-%, CO_2, 15mol-% CO and 75 mol-% N_2 was flowed through a custom-made cell with optical access for the CARS lasers. The cell was made of clear plastic pipe with an internal diameter of nearly 6 cm and a length of about 15 cm. Quartz windows were attached to either end of the pipe and sealed. Two fittings were attached in holes drilled on the pipe at either end. One fitting was used to attach tubing coming from the mixture tank, while the other fitting let the mixture flow out of the cell and into the ventilation hood above the cell. Care was taken to establish the lowest possible flow that would flush the cell without pressurizing it. The cell was considered flushed, and therefore filled with the CO_2/CO/N_2 mixture, when the CARS instrument did not detect any O_2. One thousand samples were taken at room temperature in this experiment.

The 1000 samples were reduced using FMCARS and subsequently sieved using the same criteria applied for O_2. The average measured CO_2 mole fraction was 0.49 (as opposed to 0.1) with a standard deviation of 0.30. Once again, by defining the uncertainty as two times the standard deviation, the CO_2 mole fraction thus obtained could be anywhere in the range of –0.11 and 1.09, which values are physically impossible. This leads to the conclusion that the CARS measured CO_2 mole fractions are not reliable.

Further investigation of CO_2 CARS spectra reduction revealed that FMCARS fits resulted in several widely different mole concentrations depending on the initial guess. For example, when working with the average CO_2 spectrum from all the experimental

samples, FMCARS predicted concentration values that varied from 0.02 to 0.69 mole fraction. This average spectrum was the one used in CARSFT to obtain the CO_2 instrument functions and generate the FMCARS fit libraries. Figure 5.3 shows the FMCARS fits that resulted in concentrations of a) 0.69 and b) 0.1. Notice that although the fitted concentrations are widely different, their corresponding spectra closely follow the experimental curve. Thus, it is concluded that the problem lies in two limitations of the fit methodology: (1) the numerical challenge presented by local minima found during the fit process; and (2) the approximation used for obtaining the fits.

It has been suggested (Hedman, 2001) that this behavior may be confined to low-temperature spectra where the CO_2 molecule only displays one vibrational band, i.e., the one peak showed in the spectrum. Limited studies on high-temperature spectra collected in this work from lean premixed combustion cases appear to support that claim—no dependence on initial guess was found. However, a more rigorous experimental study would be required to properly ascertain the capabilities of the new BYU CARS instrument to measure CO_2 concentrations as well as O_2 concentrations.

For future research, it is recommended to obtain CARS measurements on different mixtures whose compositions fall within the expected range and combination of concentrations to be encountered in the combustion cases of interest. Thus, one could account for the effect of a species concentration level on the accuracy and precision of the instrument. In addition, a heated cell with pressure control and optical access could be used to vary the temperatures for each of the mixtures. Such endeavor is outside of the scope of this work, and therefore only the CARS temperature measurements were used in the analysis of the combustion cases to be presented in Chapter 7.

a) Fit resulting in a value x_{CO2} = 0.69 mole fraction

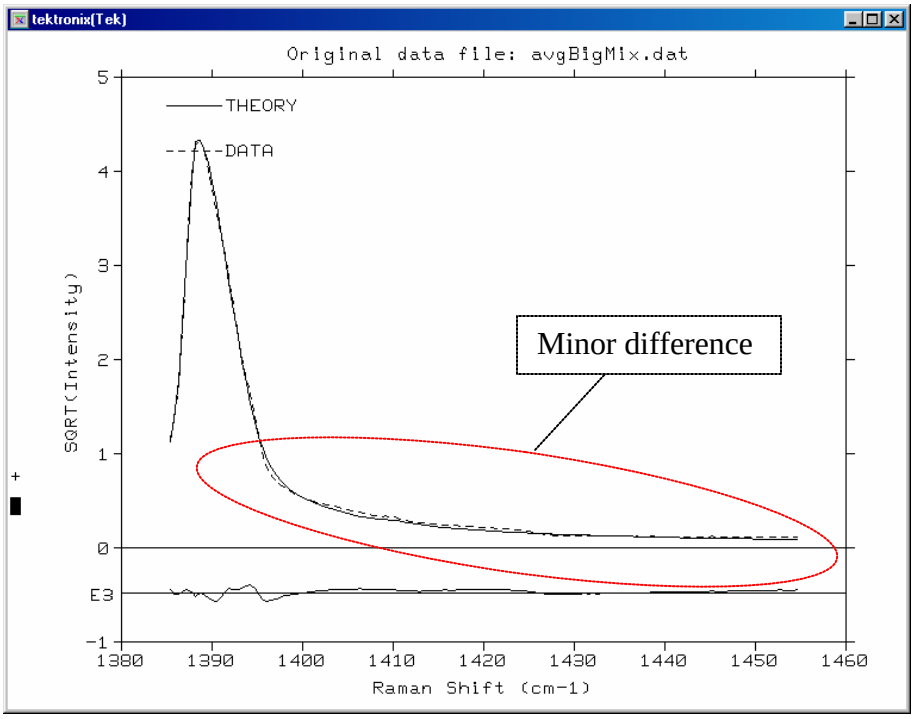

b) Fit resulting in a value x_{CO2} = 0.1 mole fraction

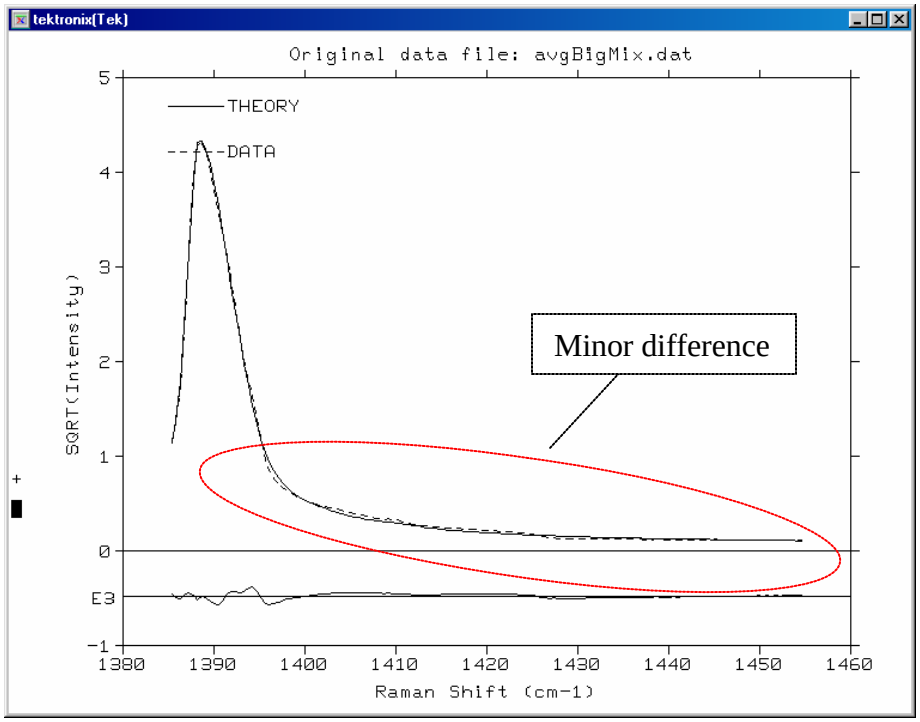

Figure 5.3. Examples of two different CO_2 FMCARS fits on the same experimental CO_2 spectrum. The reference gas contained a mole fraction of 0.1 CO_2. The different fits were obtained by using different initial guess value.

6. EXPERIMENTAL PROGRAM

The experimental measurements were obtained in the Laboratory-Scale Gas Turbine Combustor (LSGTC) at BYU (see Figure 6.1) which has the capability to run both premixed and non-premixed flames. The LSGTC was originally built at the U. S. Wright-Patterson Air Force Base and donated to BYU to study simple and complex diffusion flames near lean blow-out (Pyper, 1994). The LSGTC offers optical access for laser diagnostics and can be translated in three mutually perpendicular directions. The LSGTC is operated using a robust flow rate control system (Murray, 1998; Schmidt and Hedman, 1995). Pyper (1994) reported maximum operational uncertainties to be 3.5% on air flow rate, 3.2 % on fuel flow rate, and 0.3% on equivalence ratio.

The combustion chamber of the LSGTC operates at atmospheric pressure and was built after the design engineered by Sturgess, et al. (1992). Their main objective was to design a research combustor that closely simulated the reacting flow featured by modern annular gas turbine combustors, while being simple enough for modeling purposes.

Sturgess and co-workers used data obtained from literature as well as from computational fluid dynamics calculations to accomplish their objectives. The resulting configuration is an axisymmetric arrangement where the reactants are fed through a 22 mm ID orifice and past a 65 mm step expansion. The sudden expansion creates recirculation patterns similar to those found near the injectors in commercial gas turbine combustors. The combustion chamber consists of a square cross-section (152 mm on

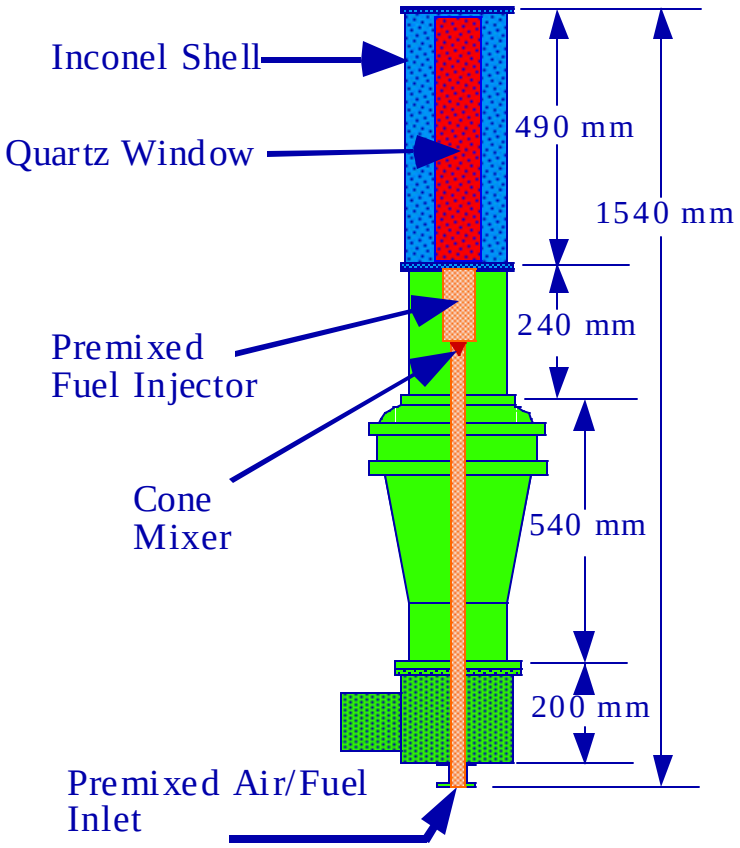

Figure 6.1. Schematic of the LSGTC at BYU.

each side) with rounded fillets at the corners to minimize vorticity that otherwise would be caused by sharp corners. A restriction, 92 mm ID, placed at the end of the chamber, introduces back-pressure effects that are meant to simulate those found on practical combustors.

Back-pressure effects arise in practical combustors because they are operated at high-pressures with secondary air injection downstream. Optical access for laser-based techniques and video recording is provided by three fused-quartz windows centered on their respective sides. The windows are 457 mm high and 76 mm wide allowing a full view of the flame, including the injection point at the sudden expansion. The fourth side

has a metal wall with an orifice that can be opened to introduce an ignition source and then closed to operate the burner.

Two studies using laser diagnostics on diffusion flames have been performed previously on the LSGTC. The first study (Warren, 1994) used a commercial turbojet engine injector from Pratt & Whitney operating with gaseous propane and air. Measurements of CARS temperatures, LDA velocities and OH PLIF images were taken which provided the basis for an analysis described briefly in the literature review (Hedman, et al., 1995; Warren and Hedman, 1995). The second study (Philips, 1998) used an injector from an actual military aircraft engine operating with liquid ethanol and air. Only LDA measurements were taken as part of that study.

Premixed combustion can be carried out in the LSGTC by feeding both the air and fuel at the bottom inlet (see Figure 6.1). Full mixing of fuel and air is ensured as the flow passes through a cone mixer, right before the injection tube (Schmidt, 1995). In the injection tube (see Figure 6.2a), the flow is straightened by means of a honeycombed brass insert that also acts as a flame arrestor. Swirling motion is then imparted to the mixture by a brass swirler near the end of the injection tube where the flow is dumped into the combustion chamber. The degree of swirl imparted to the premixed flow depends on the angle of the swirler vanes. Three brass swirl blocks (see Figure 6.2b) were made, each providing an arbitrarily chosen swirl level (Hedman, 1998): 1) low swirl (SN = 0.43), 2) medium swirl (SN = 0.74) and 3) high swirl (SN = 1.29). The swirl number, SN, is the ratio of the tangential momentum to the axial momentum and was calculated using the following equation (Gupta, et al., 1984):

$$SN = \frac{2}{3}\left[\frac{1-(d_h/d)^3}{1-(d_h/d)^2}\right]\tan\theta \qquad \textbf{(6.1)}$$

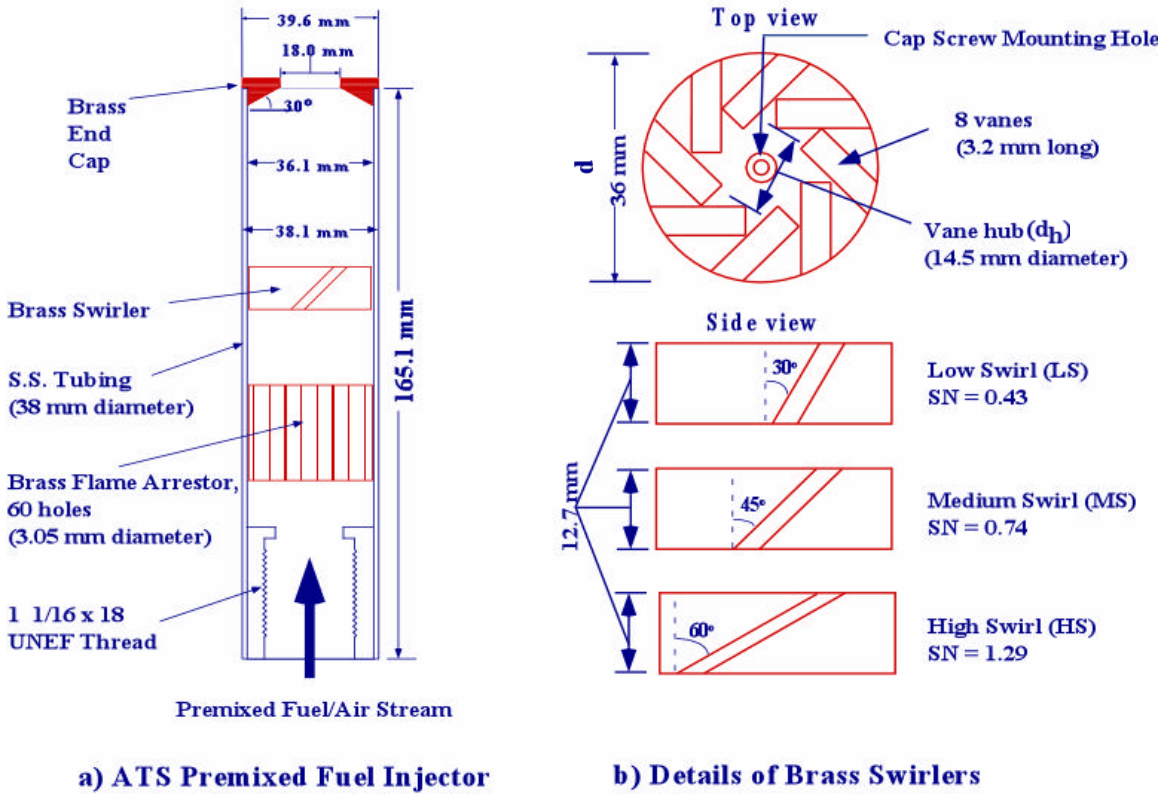

Figure 6.2. Schematics of a) premixer and b) swirl blocks on the LSGTC.

where d and d_h are the diameters of the nozzle and vane hubs respectively, and θ is the vane angle measured from the vertical axis. The dimensions of d and d_h are 36.1 mm and 14.5 mm respectively, for all three swirl blocks.

Three studies on turbulent combustion of natural gas premixed with air have been performed using the LSGTC prior to this work. A set of preliminary LDA measurements was taken by Schmidt (1995). For the same experimental conditions on the LSGTC used in this work, Murray (1998) performed LDA measurements followed by Hedman and co-workers (2002b) performing OH PLIF measurements. The CARS measurements collected on the LSGTC in this work were intended to be companion sets with those of

Table 6.1. Chemical composition of the natural gas available for the LSGTC experiments.

Compound	Mole % for August 1996	Mole % for March 1997	Mole % for July-September, 2000
CH_4	90.45-93.04	92.12-94.66	97.55 - 99.12
C_2H_6	3.41-5.37	2.66-4.01	.14 - .51
C_3H_8	0.22-1.13	0.22-0.95	.01 - .24
iso-C_4H_{10}	0.01-0.23	0.02-0.16	.00 - .03
n-C_4H_{10}	0.01-0.23	0.02-0.18	.00 - .03
iso-C_5H_{12}	0.00-0.06	0.00-0.06	.00 - .01
n-C_5H_{12}	0.00-0.04	0.00-0.04	.00 - .01
C_6+	0.00-0.03	0.00-0.05	.00 - .01
N_2	2.21-4.07	1.6-2.73	.22 - .25
CO_2	0.18-0.40	0.17-0.78	.44 - 1.38

Murray, and Hedman and co-workers. However, the composition of the natural gas to be used in this work is not exactly the same as that used by Murray in his experiments (1997), as the natural gas used on the LSGTC came from the city lines (Questar Co., formerly Mountain Fuel Supply Co.) about 3 years later. The natural gas used in this work is richer in methane, about 98 mol-% as opposed to approximately 93 mol-% for Murray's experiments as shown in Table 6.1.

No composition data was reported for the PLIF research of Hedman and co-workers. The difference in composition may or may not be of great concern, since the combustion conditions investigated were of lean stoichiometry. In fact, mass balance computations

show that the mole fraction of N_2 in the combustion cases of interest is between 0.73 and 0.74 for all cases, regardless of which natural gas composition is used. However, it is recommended that any future work account for the variation in natural gas composition in any joint analysis of the CARS, LDA, and PLIF data.

6.1 Combustion Conditions

As stated earlier, this research examines the turbulent combustion of natural gas premixed with air at atmospheric pressure in the LSGTC. However, to completely specify a combustion condition, the stoichiometry, the inlet swirl level and the air flow rate must be specified. Four combustion conditions (see Table 6.2) were selected at the beginning of the ATS experimental program (Hedman, 1998), based on applicability to industrial conditions as well as on combustion stability and operational limitations of the facilities. These same conditions are the ones investigated in this work since these are the only conditions for which LDA data are available (Murray, 1998).

Fuel lean conditions were chosen because that is how most modern industrial gas turbines operate in order to avoid the emission of unburned fuel and to minimize NO_x production. Two equivalence ratios (ϕ) were selected (see Table 6.2). These values were determined based on the Lean Blow-Out (LBO) limit of the LSGTC (ϕ about 0.56). At this equivalence ratio, no sustainable combustion is achieved regardless of the inlet swirl. The lowest value of ϕ at which stable combustion is obtained is 0.65. An intermediate lean stoichiometry of 0.80 was chosen as a second value to include the effects of stoichiometry in this study.

Three swirl levels are available for use in the LSGTC. However, preliminary runs on the LSGTC showed that the combustion for the selected lean stoichiometries was too

Table 6.2. Operating conditions investigated using the LSGTC. Flow rates are given in standard liters per minute (slpm) at 70 ºF and 14.7 psia.

	Combustion Condition			
	MS65	**HS65**	**MS80**	**HS80**
Equivalence Ratio (ϕ)	0.65	0.65	0.8	0.8
Swirl Number	0.74	1.29	0.74	1.29
Air Flow Rate (slpm)	500	500	500	500

unstable when using the lowest swirl condition. Thus, only the medium and high swirl levels were chosen (see Table 6.2). It should be mentioned that there is a noticeable stable oscillation in the flame shape when the LSGTC is operating at a medium swirl and $\phi = 0.65$, suggesting changes in combustion modes. Such flame shape oscillations are not apparent in the other three combustion conditions studied. This shows that experimental conditions investigated approach the physical limits of stable lean combustion in the LSGTC. For convenience, labels will be used from here on when referring to a particular combustion condition. For example, HS80 refers to the High Swirl case and $\phi = 0.80$ as shown in Table 6.2.

The LSGTC can handle flow rates between 350 and 2600 slpm for a wide range of equivalence ratios (Hedman, 1998). The upper limit is about one third of the flow rate values found in low-capacity practical gas turbine combustors (Sturgess, et al., 1992). Thus, it would seem appropriate to run the LSGTC at the upper limit of air flow rate. However, the air flow and fuel supply systems at the optics laboratory could not sustain such rates long enough to perform the laser diagnostics at the time the ACERC's ATS experimental program was started (Hedman, 1998). Thus it was decided to run at 500

slpm based on a temperature of 70 ºF and 14.7 psia of pressure. This is not thought to be of major concern because experiments performed on the LSGTC by Hedman (1998) showed that the dynamics of the flow (e.g., flame shape) did not change significantly with total flow rates, as long as the stoichiometry was held constant. The flows were measured and controlled by using the flow-metering system described by earlier researchers (Murray, 1998; Pyper, 1994).

6.2 CARS Data Acquisition

The CARS data were collected on a vertical plane of the LSGTC's combustion chamber. This plane is parallel to and halfway between the two opposing quartz windows for laser diagnostics in the LSGTC. In order to capture most details of the flame, it is necessary to have a good spatial grid resolution as well as a sufficient number of samples at each location for statistically reliable values of mean and standard deviations. Results from preliminary CARS data sets obtained with the same spatial grid reported by Murray (see Figure 6.3a) showed the need for more samples per location in a finer grid in both the axial and radial directions. In this research, a spatial grid of 278 points (Figure 6.2b) that included the 126 LDA sampling locations used by Murray was used. The exact number of locations sampled varied slightly for each combustion case (see Appendix C). At each location, 1000 CARS samples were collected.

It should be noted that the combustion conditions that were studied involved the reaction of the hydrocarbons in the natural gas (e.g., CH_4) with the O_2 in the air. Reaction intermediates that promote the combustion, such as OH (e.g., Mallampalli, et al., 1998), are generated during the reaction process culminating in the production H_2O and CO_2. In this research, it was not possible to obtain CARS measurements of H_2O,

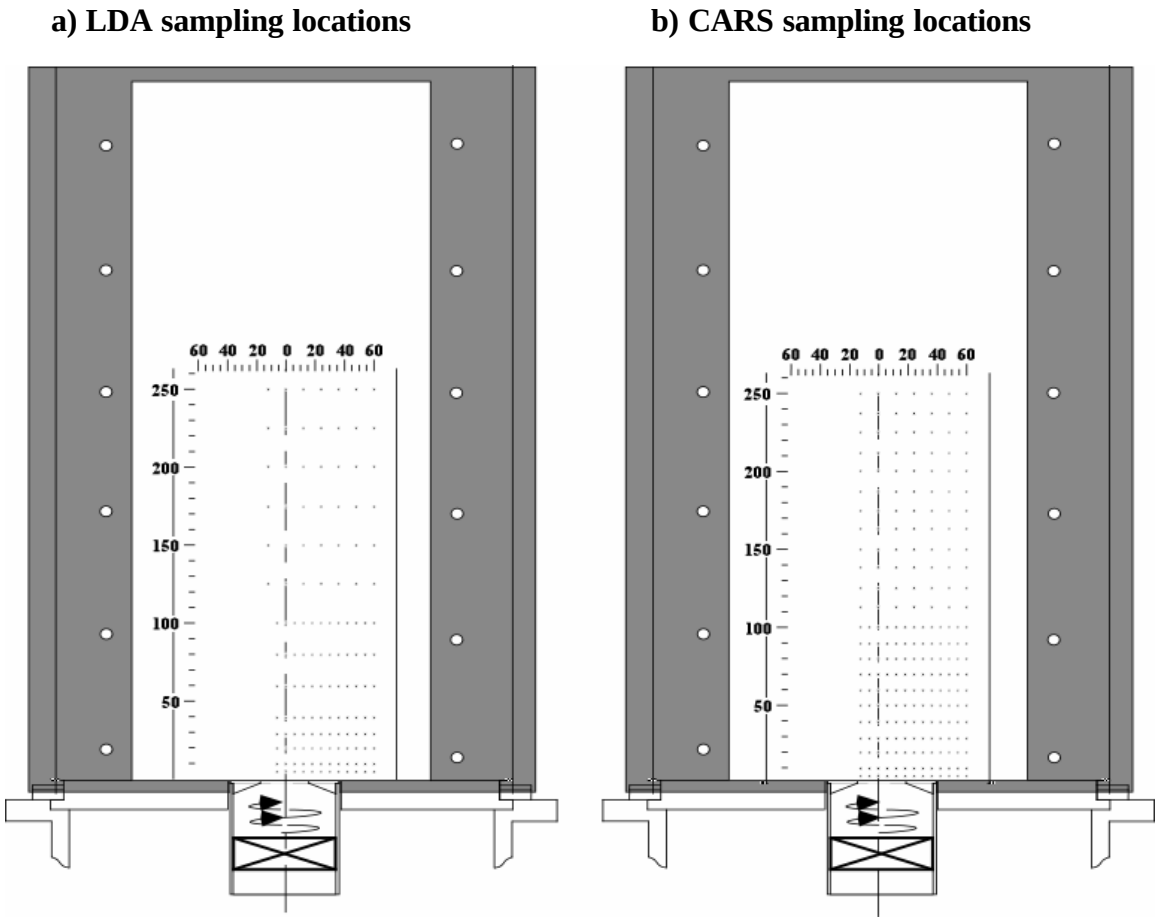

Figure 6.3. Spatial grids for data acquisition on the LSGTC combustor a) grid used by Murray, et al (1998) and b) grid used in this work.

CH_4 and the other hydrocarbons, and reaction intermediates because their respective Raman Stokes frequencies are outside the wavelength range of the dual dye laser used.

7. RESULTS AND DISCUSSION

This chapter presents the results of the CARS temperature measurements, followed by a discussion based on the following statistical values obtained from the instantaneous temperature measurements: 1) averaged temperatures, 2) normalized standard deviations, and 3) probability density functions of the instantaneous measurements. In addition, an analysis is presented for one combustion case based on combined CARS, LDA (Hedman, et al., 2002b) and PLIF OH (Hedman, et al., 2002a) measurements.

For brevity, only select plots of CARS temperature data are presented in this chapter; however, additional plots are located in Appendix C. The complete set of instantaneous temperature data at every sampling location of each combustion case are found in the CD included in this dissertation.

7.1 CARS Temperature Contours

All contour plots to be presented were generated from the experimental CARS temperature measurements using the software called "Transform" (version 3.4 from Research Systems, Inc). Each contour was based on an interpolated spatial mesh produced by interpolating between the experimental data using the Kriging method—the most accurate interpolation method according to the software documentation—with Transform's default parameters. The actual experimental data values were kept at their original locations in the interpolated mesh, which ranged as follows: (1) in the radial direction from -6 to 32 mm in increments of 0.5 mm; and (2) in the axial direction from 5

to 250 mm in increments of 2.5 mm. In addition, a copy of the interpolated mesh was flipped horizontally and aligned in order to extend the radial range from -32 mm to +32 mm and test the symmetry of the flame. All contour images show a vertical line at r = -6 mm. The horizontally flipped copy of the interpolated mesh is found to the left of this vertical line.

7.1.1 Average Gas Temperature

Iso-contour maps of the averaged gas temperatures, <T>, were produced for each of the experimental conditions investigated in this work, namely Figure 7.1 for MS65, Figure 7.2 for MS80, Figure 7.3 for HS65, and Figure 7.4 for HS80. For every sampling location in each combustion condition, the averaged temperatures were obtained from the 1000 single-shot N_2 CARS spectra following the sieving criteria outlined in chapter 5, section 5.1. The iso-contours were then produced using the procedure outlined above. The data for all combustion conditions show a high level of spatial symmetry about the centerline, as expected from the LSGTC design (Sturgess, et al., 1992).

The minimum values of <T> in the sampling grid were somewhat higher than the inlet temperatures, 350-400 K as opposed to 300 K. This indicates that even the gases just 5 mm above the inlet were already experiencing a significant amount of heating. On the other hand, the maximum values of <T> were appreciably lower than the adiabatic temperatures predicted for both stoichiometries, apparently due to heat losses. For the ϕ = 0.80 cases, the maximum average temperatures, $<T>_{max}$, are about 1600 K, roughly 400 K below the theoretical adiabatic temperature (T_{adiab}) of 2000 K predicted by the Nasa-Lewis METC program (Nicoletti, 1986). For the ϕ = 0.65 cases, the $<T>_{max}$ values are about 1500 K, roughly 250 K below the, T_{adiab} value of 1750 K. The exact reason why

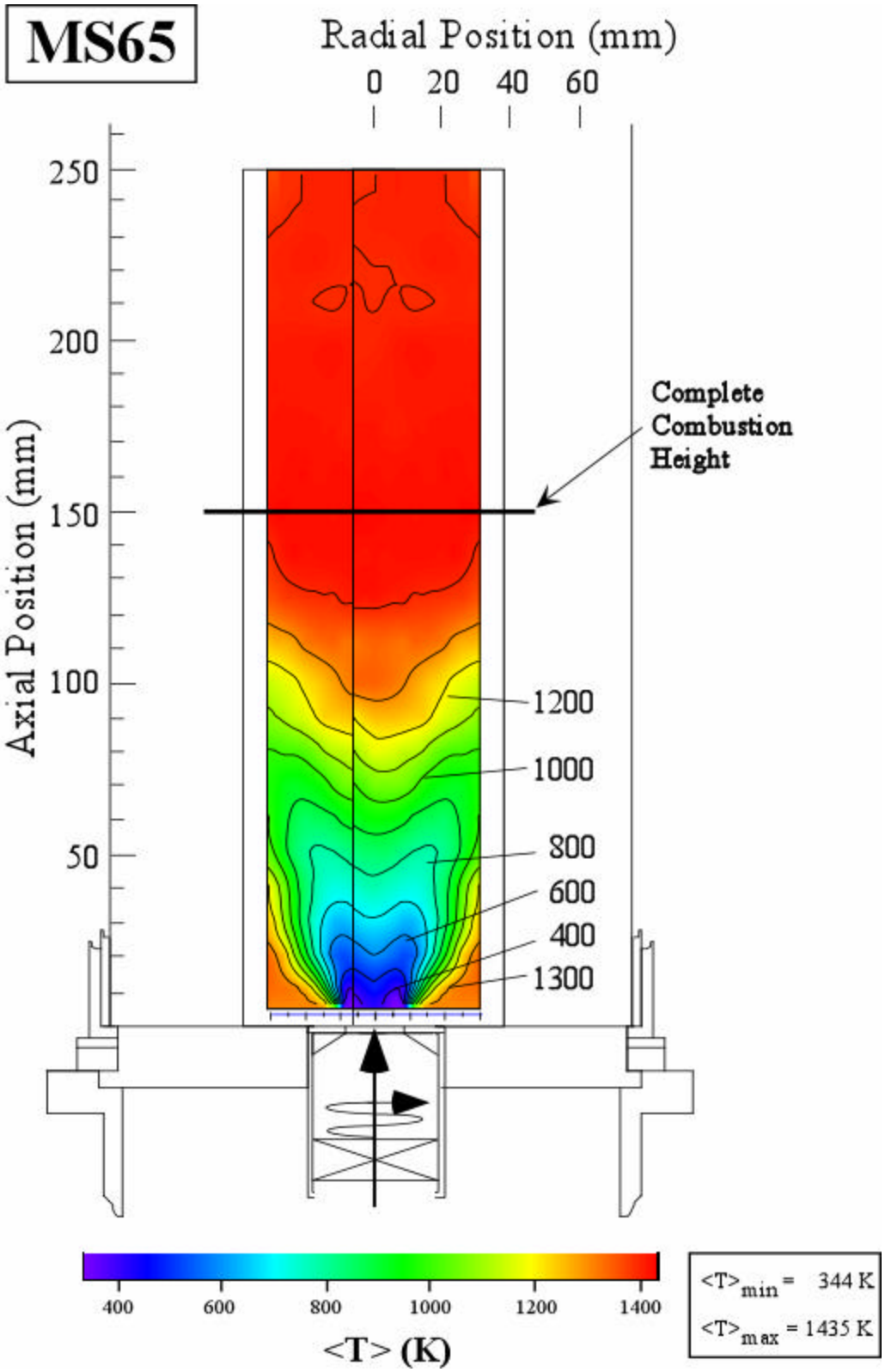

Figure 7.1. Contour maps of mean gas temperatures for the MS65 case.

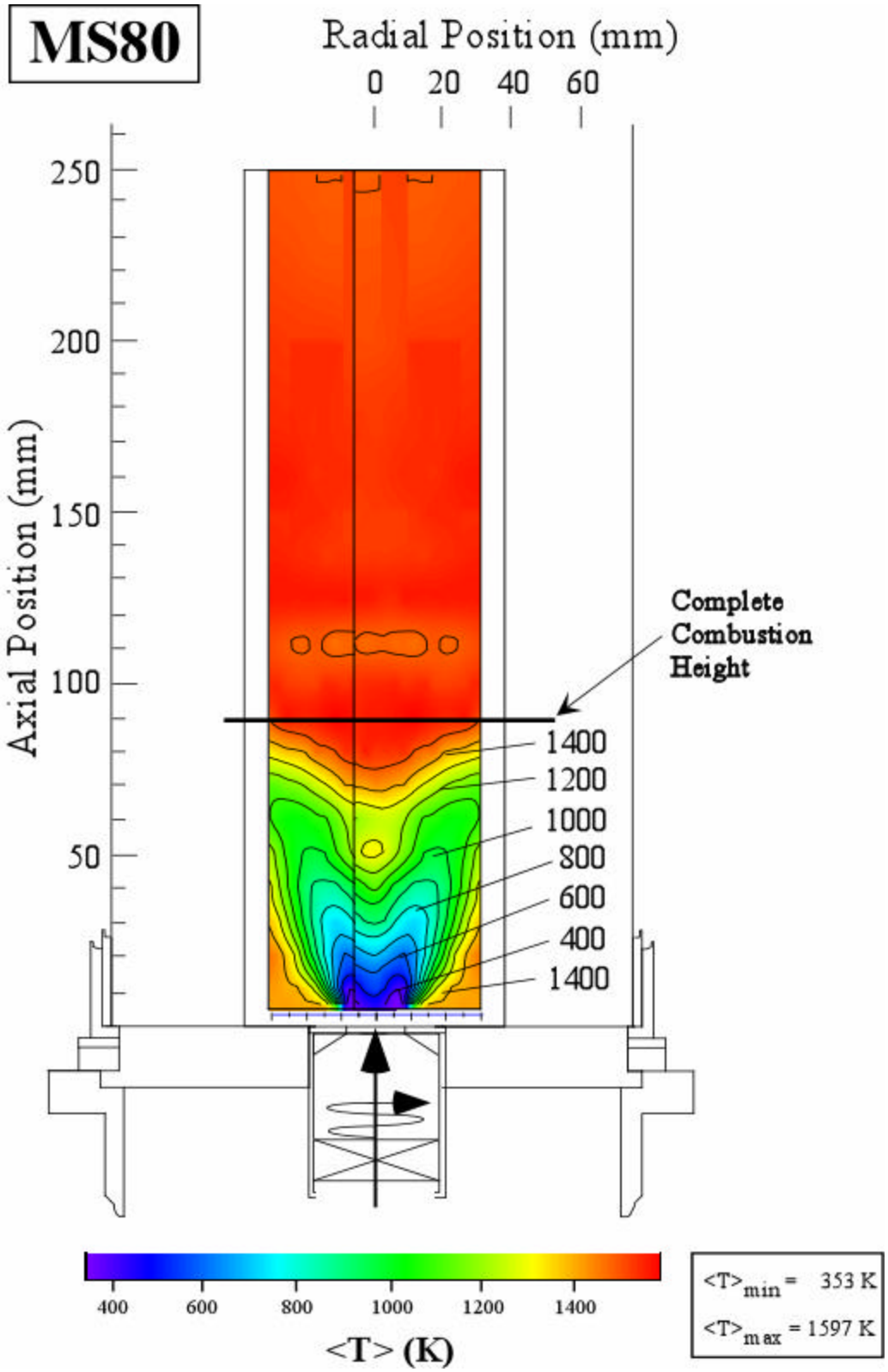

Figure 7.2. Contour maps of mean gas temperatures for the MS80 case.

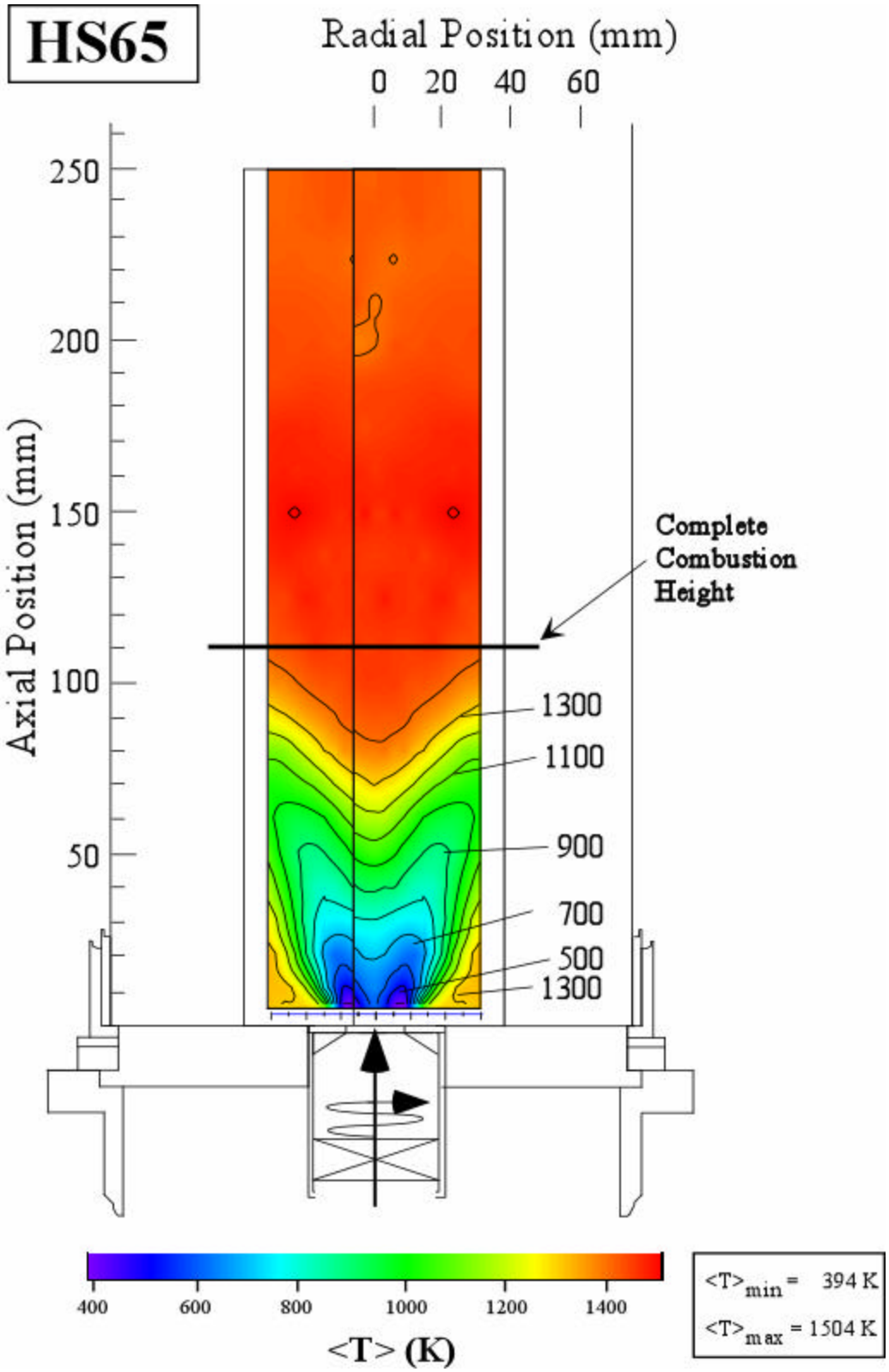

Figure 7.3. Contour maps of mean gas temperatures for the HS65 case.

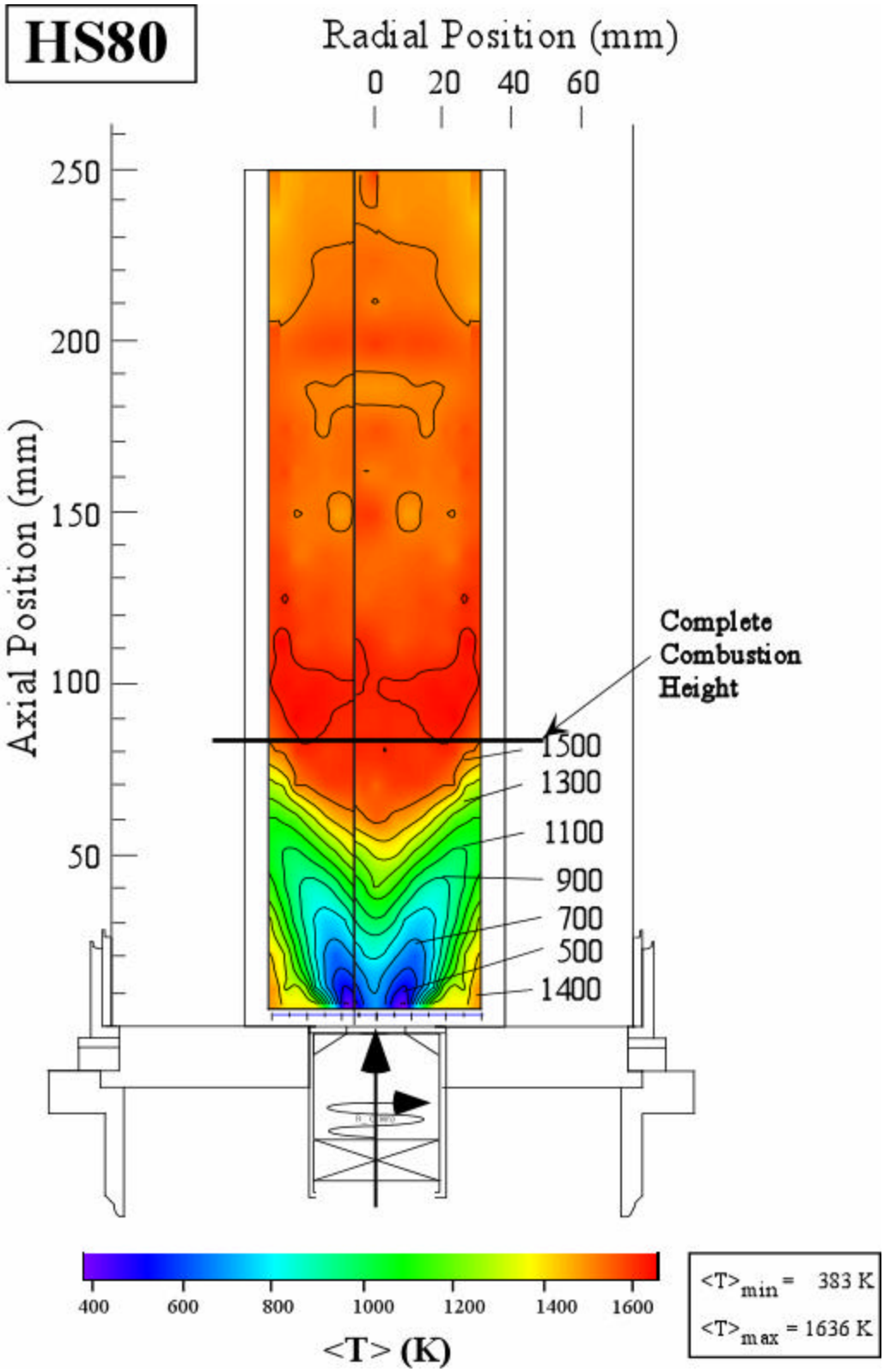

Figure 7.4. Contour maps of mean gas temperatures for the HS80 case.

the $\phi = 0.80$ cases showed a larger difference between T_{adiab} and $<T>_{max}$ than the $\phi = 0.65$ cases is not known but may be related to greater radiative heat losses.

A good level of confidence in the measurements is supported by the fact that they show (a) the expected flame symmetry, (b) maximum average temperatures below the adiabatic values, and (c) minimum average temperatures slightly above the inlet values.

The contours of average gas temperatures also show flame features that are common to all four experimental conditions. The shapes of the contour maps of all the combustion cases are strikingly similar, exhibiting a low temperature trough near the inlet, which roughly follows a diagonal direction determined by the swirl angle. Temperature then increases as the gases move radially and axially away from the inlet. This general pattern is exhibited in all four cases and is described in more detail in the following paragraphs.

The shape of the axial profiles of <T> varies in two ways. For the axial profiles along the centerline and at r = 9 mm (see Figure 7.5), <T> increases with height until it reaches an approximately constant value. The other combustion cases show the same behavior (see Appendix C), except for the MS80 case, which had a minor initial drop in <T> followed by an immediate increase in <T> at a height of about 50 mm. Axial <T> profiles at r = 21 mm and 30 mm (see Figure 7.5), show an initial decrease of a few hundred of degrees at z = 5 mm. At approximately z = 50 mm, the values of <T> begin to rise until a relatively constant temperature is achieved at about z = 100 mm.

The <T> profiles in the radial direction are somewhat more complex, depending on the combustion condition. All combustion cases have a particular height where the radial <T> profiles are almost constant (for example, see Figure 7.6, z = 80 mm, and 100 mm), possibly indicating that the combustion is complete. The “complete combustion” heights

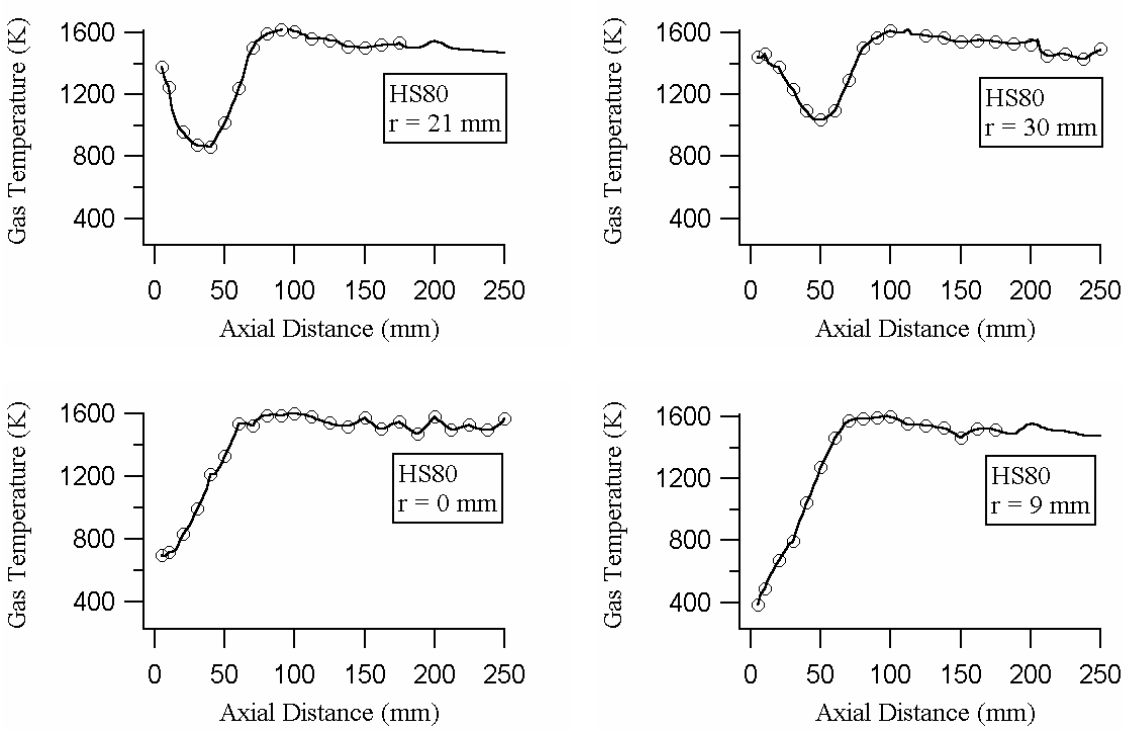

Figure 7.5. Axial temperature profiles at selected radial positions for the HS80 case

for each case are approximately as follows: (1) 150 mm for the MS65 case, (2) 90 mm for the MS80 case, (3) 110 mm for the HS65 case, and (4) 90 mm for the HS80 case.

At the earliest axial position (z =5 mm) in Figure 7.6, a small peak in the <T> radial profile is seen at the centerline (the peak is more apparent when the profiles are reflected about the symmetry axis). A small trough in the shape of this temperature profile is observed at r = 8 mm. The radial <T> values rise rapidly between r = 10 and 17 mm, and then become nearly flat towards the wall. This shape of the radial <T> profile persists at higher axial positions (see Figure 7.6), except that the radial location of the trough is farther away from the centerline and the centerline peak becomes less noticeable.

For all combustion conditions, the magnitudes of the radial <T> gradients are most severe near the inlet, specifically, at a height of 5 mm and a radial position of 9 mm.

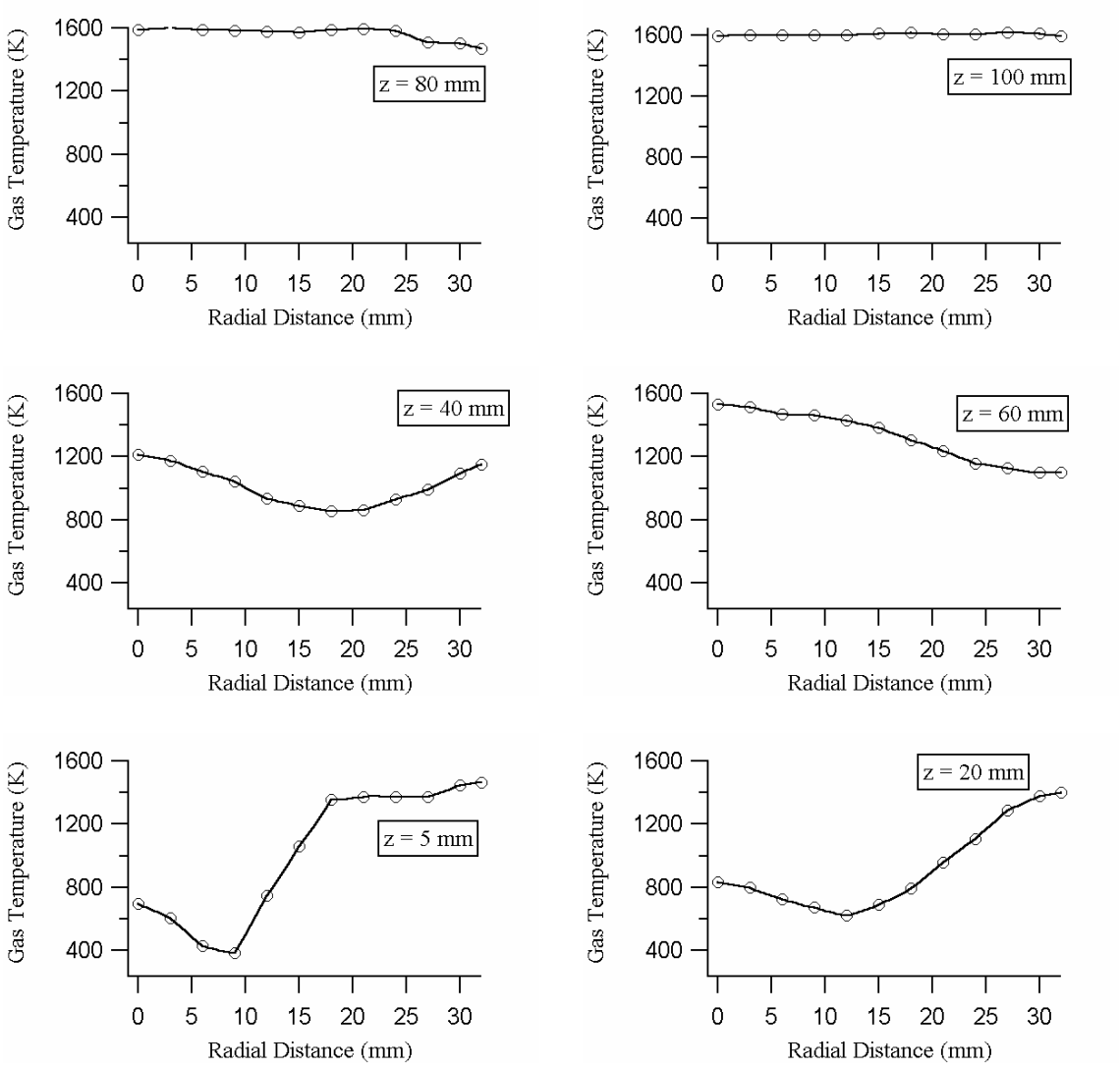

Figure 7.6. Radial temperature profiles at selected heights for the HS80 case.

<T> increases from about 400 K to about 1300 K occur over a radial distance of (1) 6 mm for the medium swirl cases, and (2) 9 mm for the high swirl cases. It should be noted that the relative size of these radial distances is consistent with the fact that at a higher swirl number the cold inlet mixture is injected at an angle that moves the flow closer to the bottom plate. In this way, larger amounts of cold gas flow in the radial direction than

for lower swirl conditions; therefore, it takes longer to heat up the inlet gases at high swirl conditions.

7.1.1.1 Flame Stability Observations

Variations in the flame stability of the combustion conditions were observed visually during these experiments. Flame stability was determined subjectively in this work from (a) the self-sustainability of the flame upon ignition with an external source, (b) the time required to achieve steady state conditions, and (c) the degree of large-scale oscillations in the flame shape. Less stable combustion conditions were difficult to light and tended to self-extinguish unless exposed to the external ignition source for sufficient time. For example, when lighting the MS65 condition, the external source needed to remain in the flame for a period of 2-3 minutes before the flame could sustain itself. On the other hand, when lighting the HS80 case, the flame sustained itself without the external ignition source almost immediately after ignition.

Based on the flame stability observed during burner ignition, the combustion cases were ranked according to decreasing degree of stability as follows: (1) HS80 (the most stable case); (2) MS80; (3) HS65 (very similar to MS80); and (4) MS65 (the least stable). Similar observations on flame stability were reported in previous studies for these cases (Hedman, et al., 2002b; Murray, 1998).

There appears to be a direct relationship between the height of complete combustion and the observations on flame stability just mentioned in the preceding paragraph: the lower the height of completion, the higher the stability of the flame. The effect of ϕ on flame stability is seen by the effect of ϕ on the height of completion (see Figure 7.1 and Figure 7.2, or Figure 7.3 and Figure 7.4). It appears that the increased heat release due to

higher fuel equivalence ratio (0.80 versus 0.65) had the effect of increasing flame stability by bringing the flame closer to the injector inlet as shown by the lower heights of complete combustion for $\phi = 0.8$. On the other hand, the effect of the swirl condition on flame stability can be seen by the effect of swirl on the heights of complete combustion (see Figure 7.1 and Figure 7.3, or Figure 7.2 and Figure 7.4). In the higher swirl cases, the heights of complete combustion are lower for the same ϕ, meaning that the flame is closer to the injector. In addition, the fact that the maximum gas temperatures are higher for the higher swirl and same ϕ (1435 K versus 1504 K for the $\phi = 0.65$ cases, and 1597 K versus 1636 K for the $\phi = 0.80$ cases) indicates that the higher swirl tends to burn the gases with less heat losses. This could mean that the higher swirl enhances flame stability by making the heat released from combustion more readily available to the inlet stream.

The MS65 case was particularly unstable and very near the point of extinction. As mentioned previously, in order to start burner operation for this case, it was required to keep the ignition source on for a couple of minutes until the LSGTC chamber became hot enough to stabilize the flame. In addition, during operation, the visible flame of the MS65 case oscillated between being spread throughout the length of the combustor and collapsing into a flame sustained in the middle of the combustor. The mean temperature map for the MS65 case does not readily show this behavior (Figure 7.1) because of the averaging involved. However, the average temperature contours do show that, when compared to the other cases, the MS65 case: 1) has the highest "complete combustion" heights in the combustion chamber; and 2) that its maximum average flame temperature (1435 K versus 1636 K) is the lowest among all four cases.

7.1.2 Turbulent Fluctuations in the Gas Temperature: Standard Deviations

Standard deviations (σ) in the gas temperature were calculated from the 1000 single-shot N_2 CARS samples obtained at each location. In order to compare the turbulent fluctuations in the gas temperature for the four combustion cases, the local standard deviations were divided by their corresponding local average temperatures (<T>) and expressed on a percent basis, $\sigma/<T>$ %. This approach is parallel with the way turbulent intensities of velocity are treated in the turbulent flow literature (e.g., Gupta, 1984). Figures 7.7 through 7.10 show the iso-contour maps of the normalized standard deviations for the four combustion conditions investigated in this work. The maximum and minimum normalized standard deviation values for each case are listed for convenience. Consistent with the average gas temperature contours, the normalized standard deviation plots reflect the axisymmetric nature of the flame.

For all the combustion conditions, there is a height above which all $\sigma/<T>$ % values are 10% or less—which means that the temperature values are constant given that the instrument uncertainty (defined in chapter 5, section 1) is about 15%. The heights where the temperature turbulent fluctuations cease are 60 mm for HS80, 80 mm for both HS65 and MS80, and 110 mm for MS65 (see Table 7.1).

Figure 7.11 shows an alternate representation of these data and reveals several features. First, for the $\phi = 0.80$ cases, the characteristic height where temperature fluctuations cease is equal to the height where combustion appears to cease for each swirl condition. For the $\phi = 0.65$ cases, the characteristic height where temperature fluctuations cease are lower than the height where combustion appears to cease for both swirl conditions. Second, regardless of ϕ value, the cessation-of-fluctuation heights are

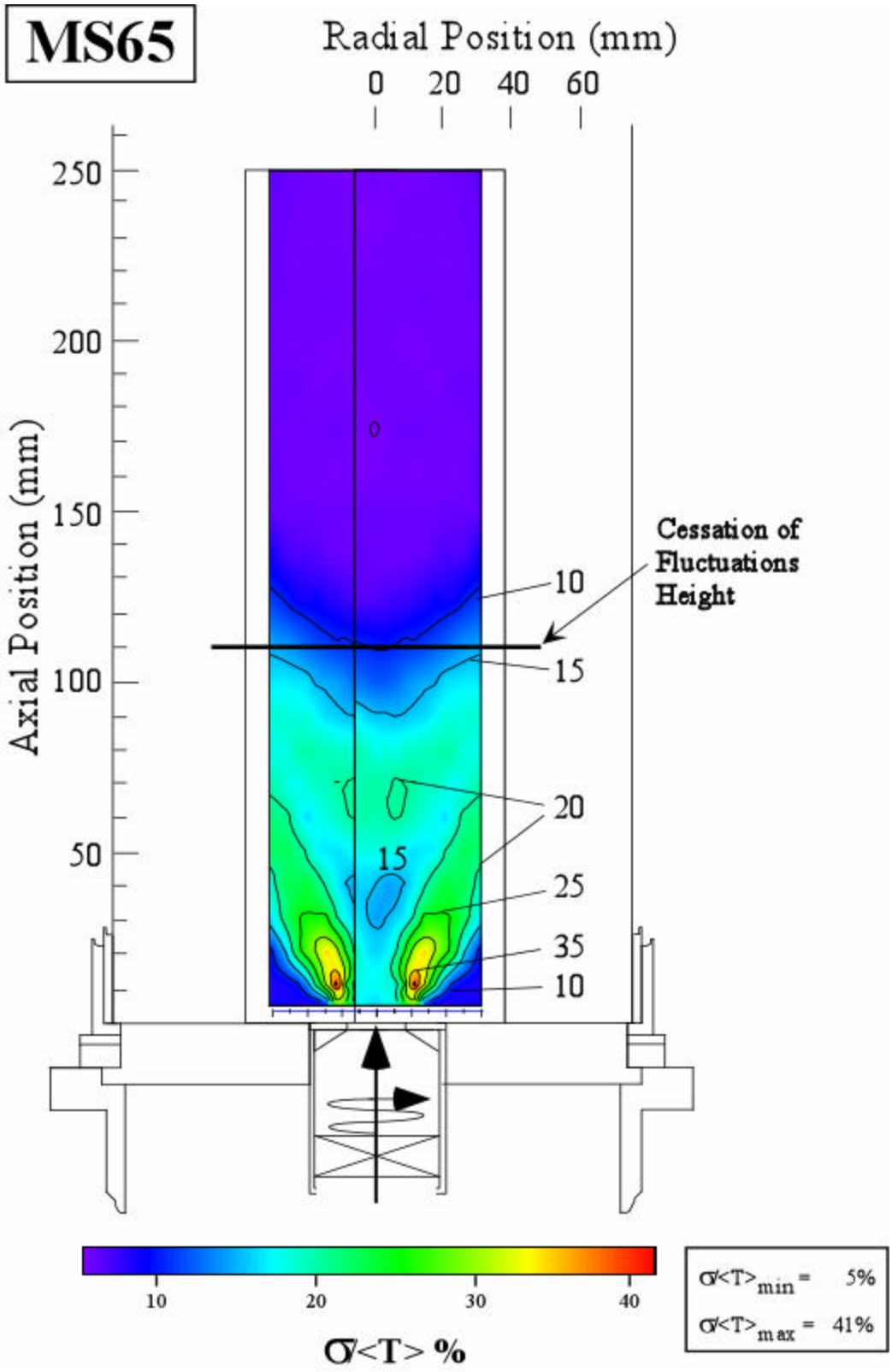

Figure 7.7. Contour maps of normalized standard deviation gas temperature for the MS65 case.

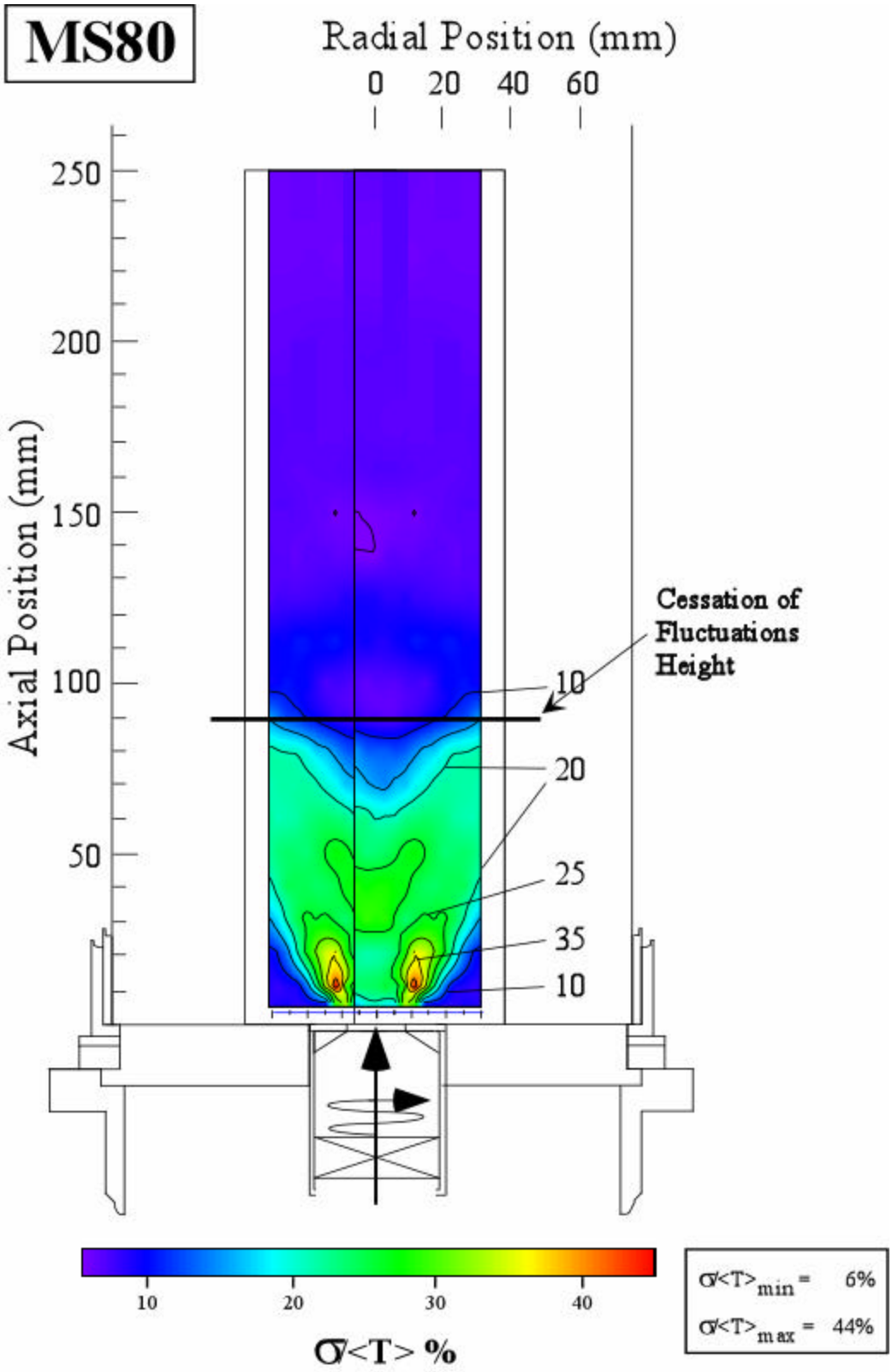

Figure 7.8. Contour maps of normalized standard deviation gas temperature for the MS80 case.

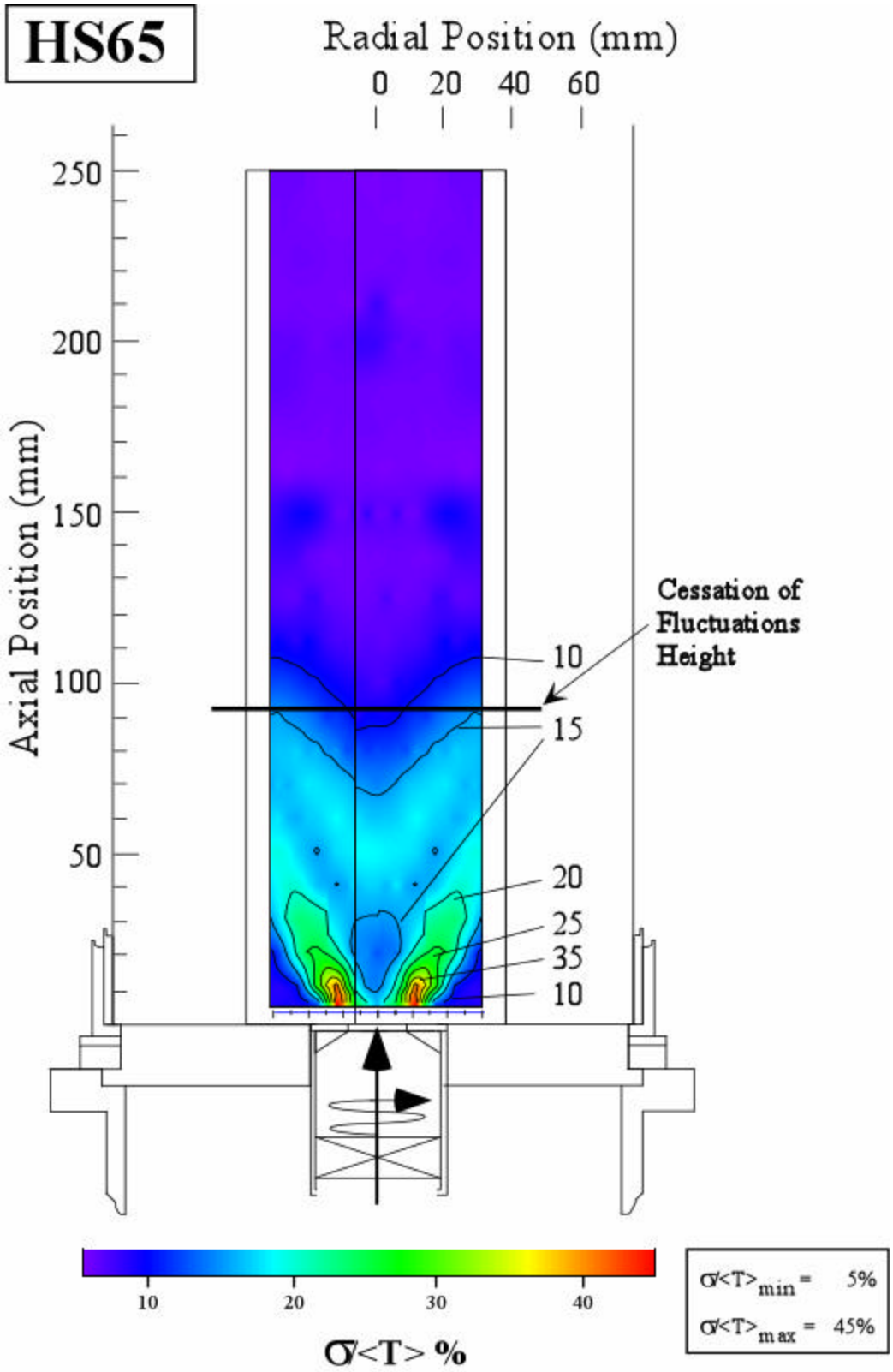

Figure 7.9. Contour maps of normalized standard deviation gas temperature for the HS65 case.

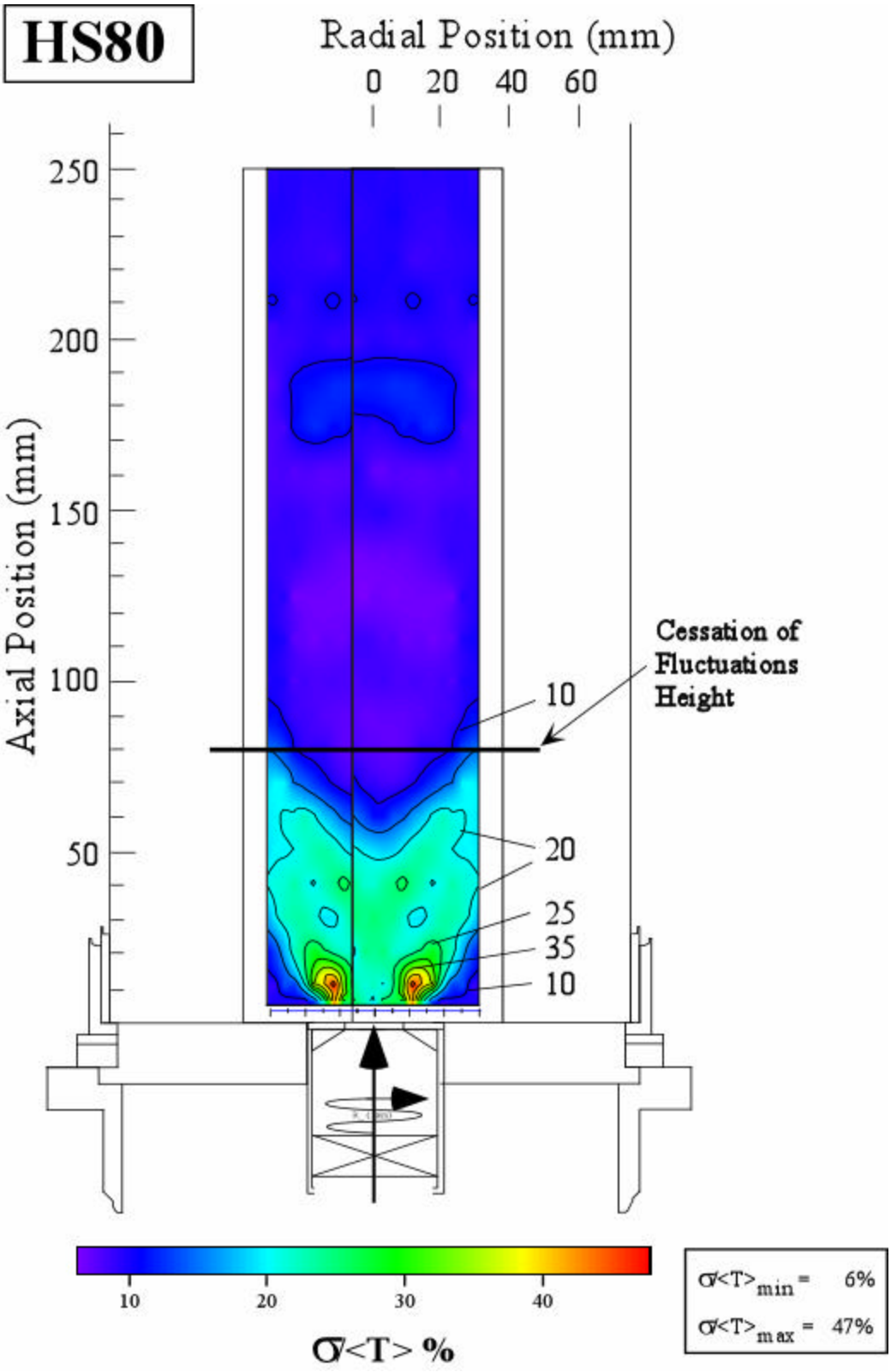

Figure 7.10. Contour maps of normalized standard deviation gas temperature for the HS80 case.

Table 7.1. Characteristic flame heights and range of normalized standard deviations for each combustion case.

	Characteristic Heights in mm		Range of values for Normalized s	
Combustion Case	**Complete Combustion**	**Cessation of Fluctuation**	**% s /T_{min}**	**% s /T_{max}**
HS80	80	80	6	47
MS80	90	90	5	44
HS65	110	90	5	45
MS65	150	110	5	41

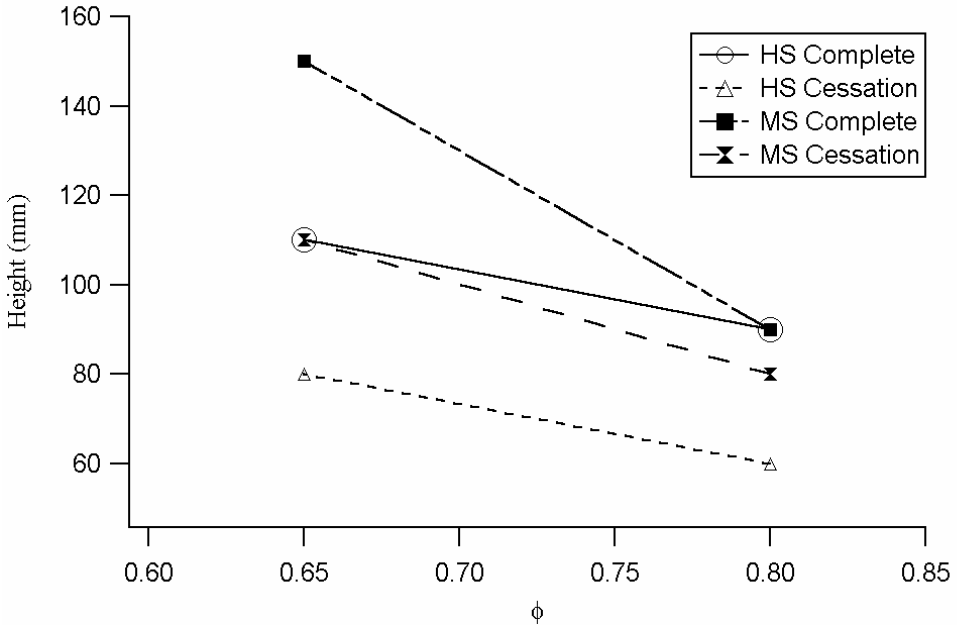

Figure 7.11. Characteristic heights of complete combustion and cessation of fluctuation, plotted as a function of f.

the lowest for the HS cases, while the heights of complete combustion are the highest for the MS cases. Third, the cessation-of-fluctuation heights for the MS cases are only slightly higher than the complete-combustion heights for the HS cases. These data show that higher swirl tends to bring the reacting portion of the flame closer to the inlet, more so than higher fuel content. It is well known that attached flames are generally more stable than freestanding flames (Lewis and von Elbe, 1987). Based on visual observations, profiles of <T>, and profiles of $\sigma/<T>$, it is therefore concluded that, for the cases studied, the swirl level has a larger influence in bringing the flame closer to the inlet than ϕ.

Figures 7.7 through 7.10 also show several common features for all cases. First, the peak temperature fluctuations (σ/T % about 40%) are located in an area between 10 and 20 mm of height and between 15 and 20 mm of radius—just above the outer diameter of the inlet. Second, all cases show temperature fluctuations (, i.e., $\sigma/<T>$ % greater than 15%) throughout the combustor region below the heights of cessation of temperature fluctuations with the exception of the bottom corners. Third, the temperature fluctuation contours spread out diagonally upward from the inlet, decreasing in value but still comparable to the temperature fluctuations along the centerline and below the height of cessation of temperature fluctuations.

The temperature fluctuations data thus outlined in this section indicate that there is mixing of cooler inlet gases with hot gases throughout the flame. However, the most intense mixing of cold and hot gases exists very close to the inlet. It is possible that this intense mixing near the inlet at least contributes to the ignition of the fresh inlet stream and may even be the very source of ignition.

7.1.3 Gas Temperature Turbulent Fluctuations: Probability Density Functions

Probability density functions (PDFs) were obtained for every sampling location throughout the combustor for each of the four combustion conditions. The PDFs were obtained from histograms of the nearly 1000 instantaneous gas temperature measurements at each location of interest in the spatial grid.

Four types of PDF distributions were found to exist in all combustion conditions (see Figure 7.12): delta, beta, normal, and bimodal distributions. PDF plots were generated for all radial positions away from the centerline at various axial positions: Figure 7.13 for z = 10 mm; Figure 7.14 for z = 50 mm; Figure 7.15 for z = 70 mm; and Figure 7.16 for z = 90 mm. Each figure consists of four columns of plots, one for each combustion condition (i.e., MS65, MS80, HS65 and HS80). Appendix C contains similar figures for additional heights. The PDF data give significant insights into the way hot and cold gases are mixed at a specific location.

Each PDF has a "breadth" which is defined by the difference between the lowest- and highest-temperature bins, i.e., the total width of the base of the PDF from the beginning of the left wing to the end of the right one. Table 7.2 shows the relative occurrence for each PDF expressed as the percent of the PDFs generated (z = 90 mm and below). In general, beta distributions were the most frequent while the delta occurred the least.

The shape of each PDF distribution has a physical significance giving insights into the nature of the temperature fluctuations at a given location. The PDF distributions can be interpreted in the following ways:

1. A delta distribution implies a constant temperature because most of the temperature measurements fall within one bin in the histogram. These

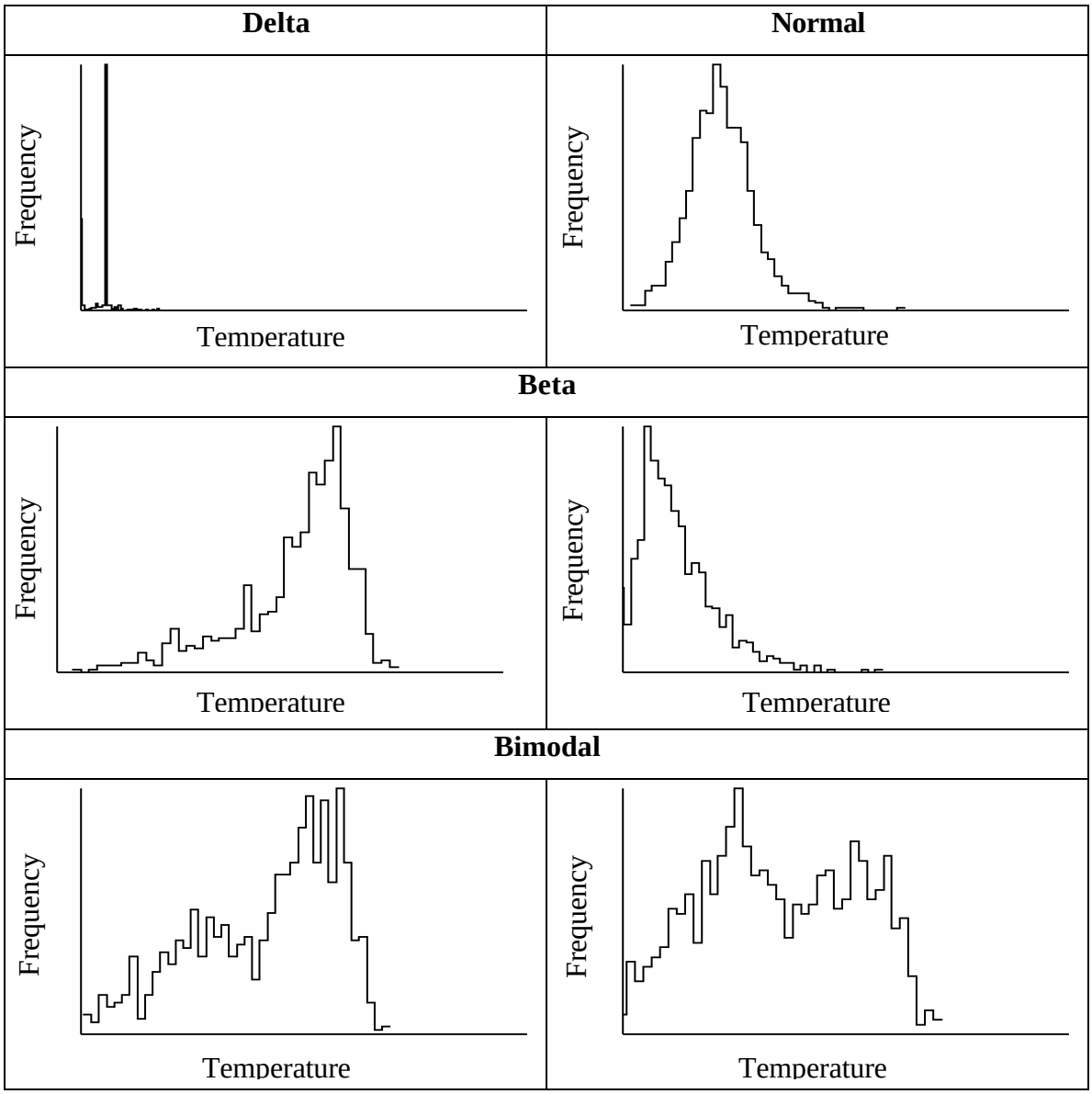

Figure 7.12. Types of PDF distributions in the combustion experiments.

distributions were found only at about 400 K. For the MS65 and MS80 cases, they were found at the 5 and 10 mm heights and at radial distances up to 9 mm away from the centerline. Delta distributions were also observed in the HS80 case, but only at the height of 5 mm and at two radial locations (6 and 9 mm). No delta distributions were observed in the HS65 samples.

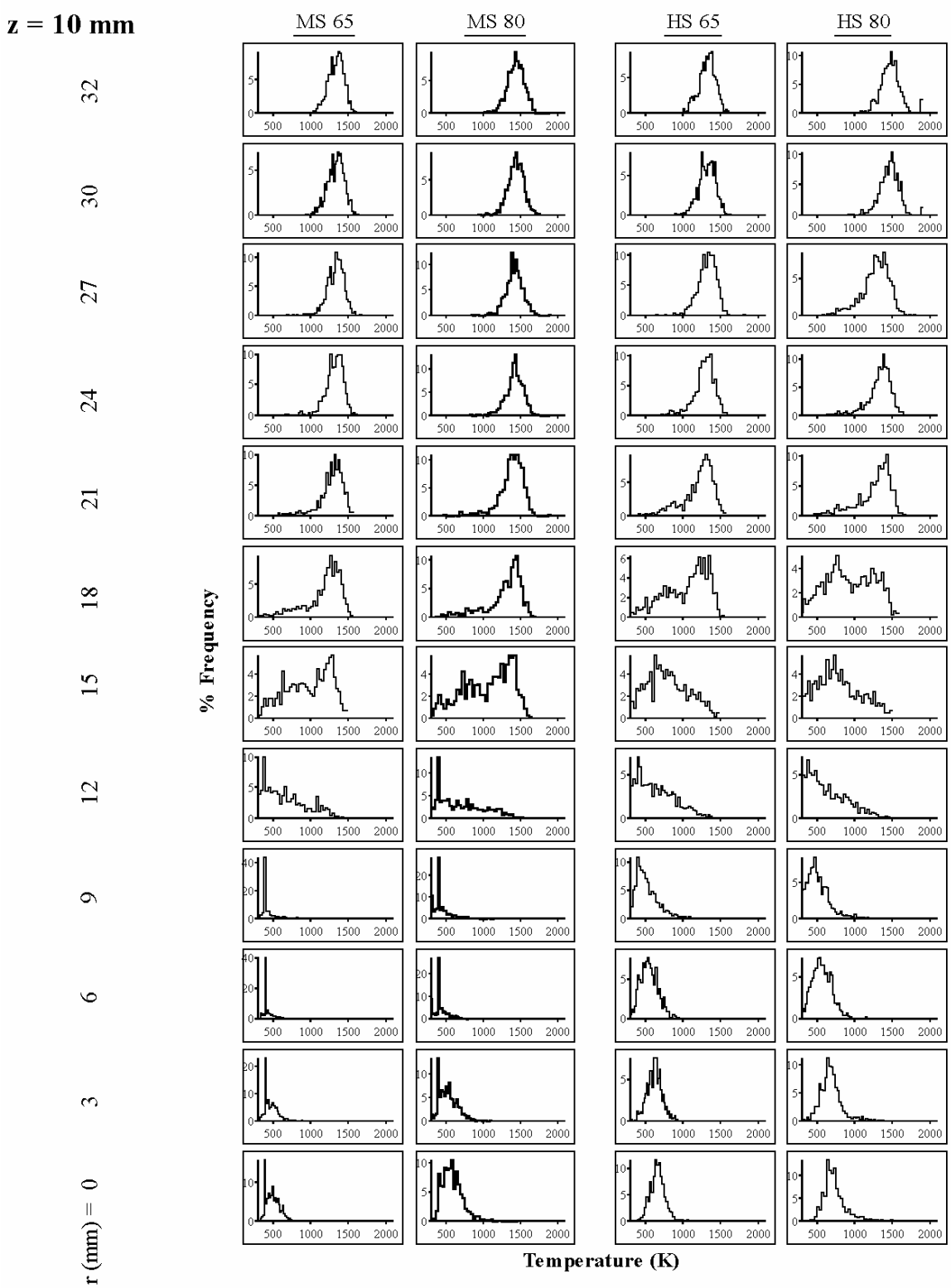

Figure 7.13. Gas temperature PDFs as a function of radial position for z = 10 mm.

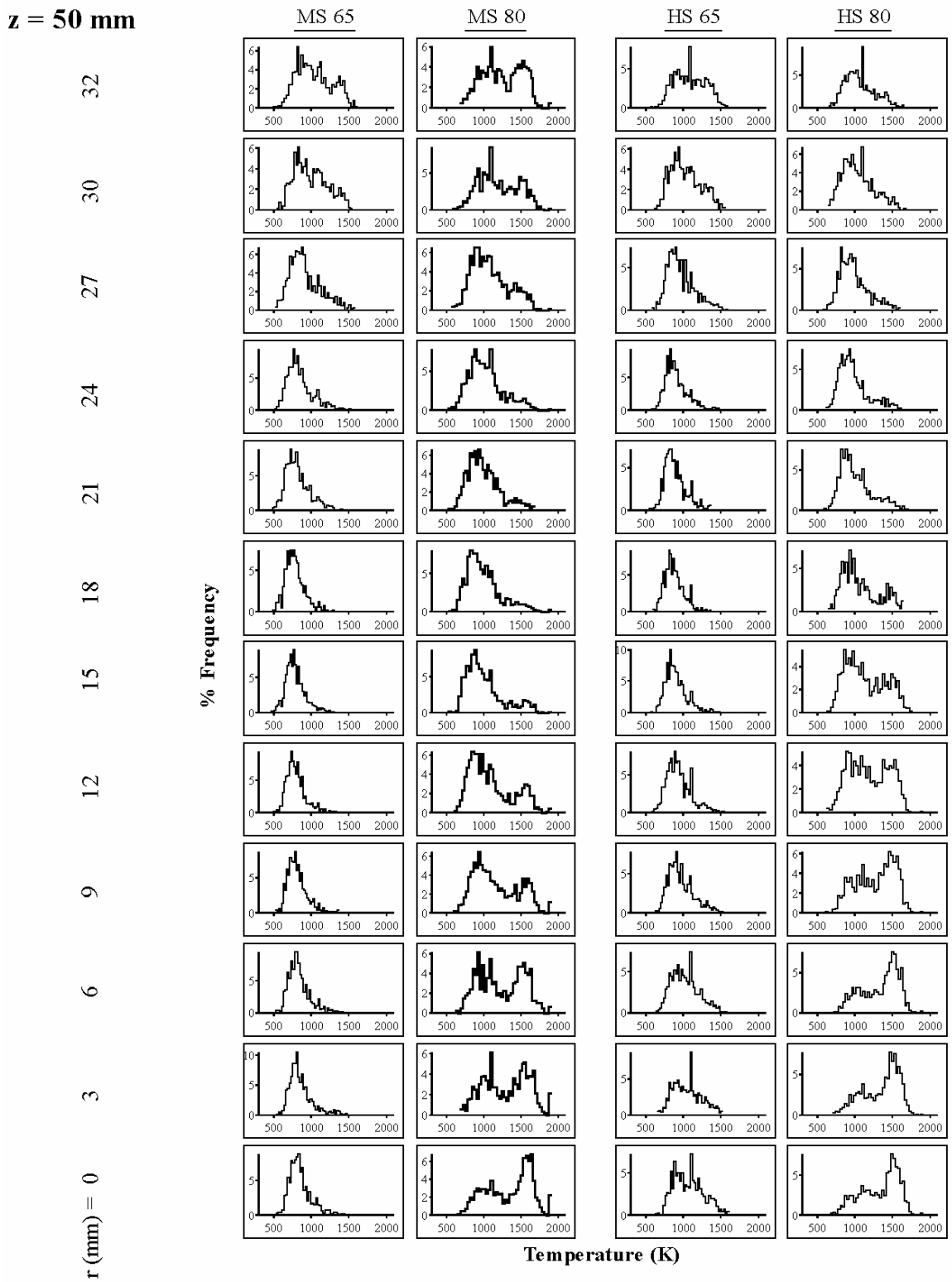

Figure 7.14. Gas temperature PDFs as a function of radial position for z = 50 mm.

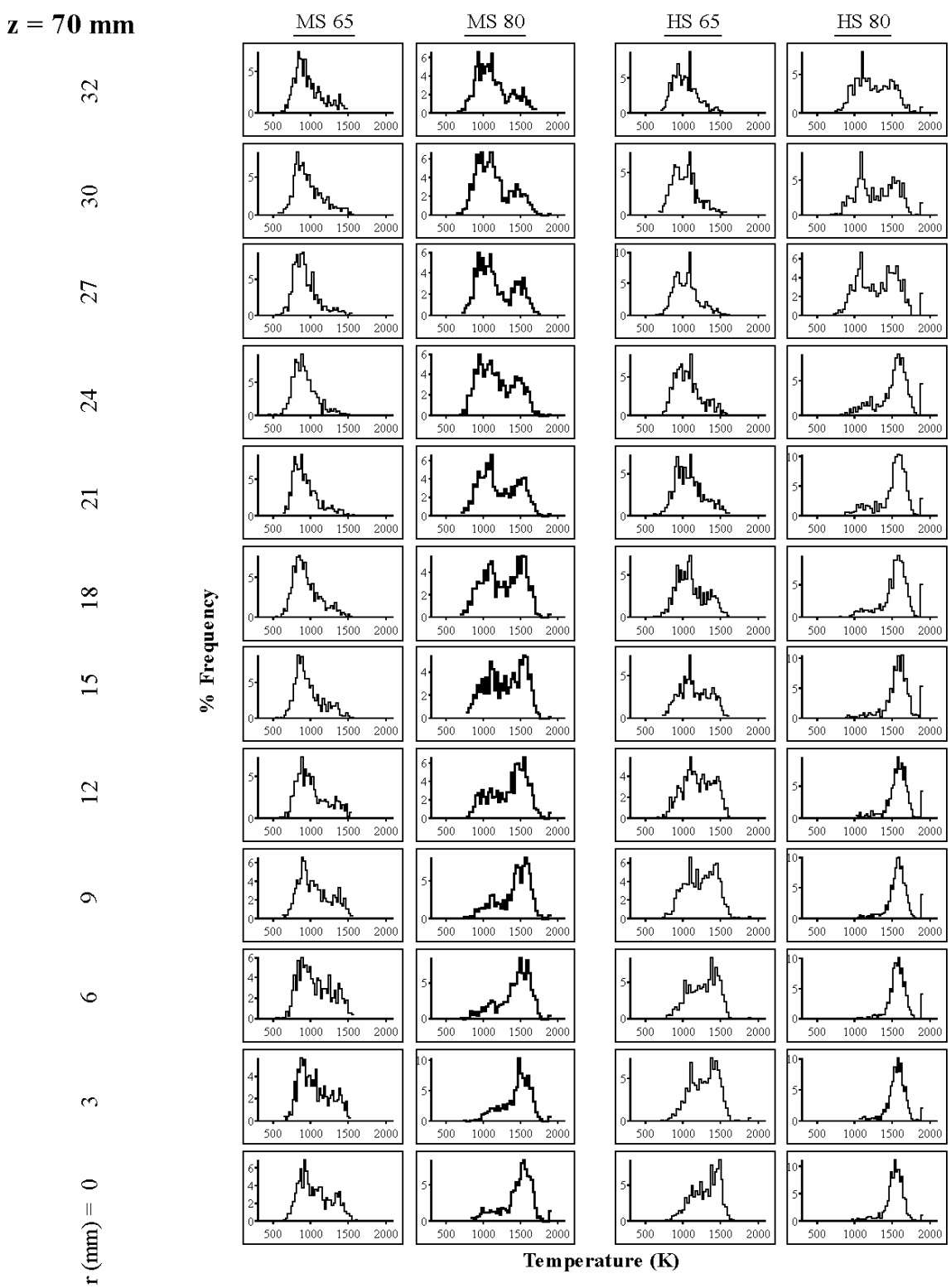

Figure 7.15. Gas temperature PDFs as a function of radial position for z = 70 mm.

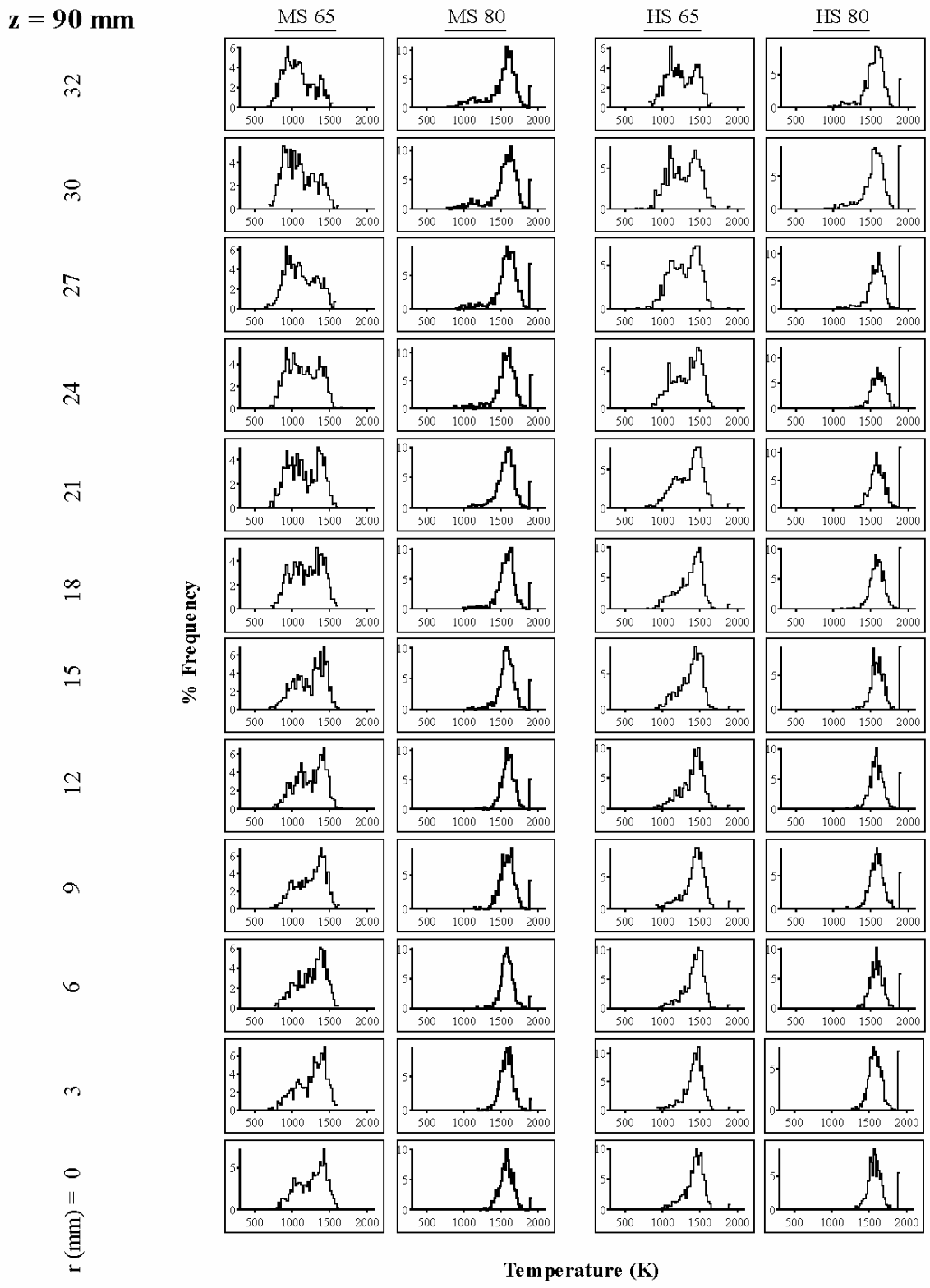

Figure 7.16. Gas temperature PDFs as a function of radial position for z = 90 mm.

Table 7.2. Relative occurrence (%) of PDF shapes for each combustion case.

	PDF shape			
Combustion Case	**Delta**	**Beta**	**Normal**	**Bimodal**
MS65	1	85	5	9
HS65	0	87	5	8
MS80	1	82	6	11
HS80	<1	82	9	8

2. A beta distribution implies a predominance of a temperature value around the peak of the distribution, with significant contributions of either higher (one wing extended to the right) or lower temperature (one wing extended to the left) gases. Most beta distributions had a breadth of about 1000 K. Examples for each combustion case at z = 10 mm include: 1) MS65 at r = 18 mm; 2) MS80 at r = 18 mm; 3) HS65 at r = 9 mm; and 4) HS80 at r = 9 mm.
3. A normal distribution implies either that the gas mixture is not reacting at the given location and therefore has constant temperature, or that there is an even contribution of both hot and cold gases centered about a given temperature. The typical breadth of these distributions was about 500 K. Examples for each combustion case at z = 10 mm include: 1) MS65 at r = 18 mm; 2) MS80 at r = 18 mm; 3) HS65 at r = 9 mm; and 4) HS80 at r = 9 mm.
4. Bimodal distributions imply the existence, at different times, of two gas streams whose temperatures vary widely and are centered at either one of the contiguous peaks. Typically, the two peaks in the distributions were separated by as much as 500 K, and their breadth was as much as 1000 K. Examples for each combustion case at z = 10 mm include: 1) MS65 at r = 18 mm; 2) MS80 at r = 18 mm; 3) HS65 at r = 9 mm; and 4) HS80 at r = 9 mm. Bimodal

distributions would be expected in a shear layer created by a mixing interface of fresh, unreacted inlet gases with fully reacted gases. This interaction would result in eddies of hot and cold gases existing at different times at the same location. It must also be mentioned that there were a few distributions as wide as the bimodal distributions but with no definite peaks. It is believed that these are special cases of a bimodal distribution where there is a more or less continuous distribution of the gas temperatures.

Additional insights regarding the flame behavior were obtained by examining the spatial variation in the shape of the PDFs for all the combustion conditions. First, the maximum and mean temperatures of the PDFs for the $\phi = 0.80$ cases were generally higher than for the $\phi = 0.65$ cases. This makes sense because more heat is released by the combustion of more fuel at the higher equivalence ratio, which also agrees with the trend in the adiabatic flame temperature.

Second, although the shapes of the PDFs varied both axially and radially for all cases, it is interesting to examine the general location where similar trends in the PDF shapes were observed:

1. For heights below 40 mm, (e.g., z = 10 mm in Figure 7.13), the shapes of the PDFs for the MS65 and MS80 were essentially the same for the same radial position, just shifted towards higher temperatures for the MS80 case. A similar situation was also observed between the HS65 and HS80 cases. However, the PDF shapes were significantly different for cases of different swirl number and same ϕ. This seems to indicate that near the inlet, the

nature of the temperature fluctuations (and thus the cold/hot gas mixing) is predominantly determined by the swirl level.

2. Close to the centerline and at heights of 40, 50, and 60 mm, the variation of the shape of the PDFs was also a function of the radial position (e.g., z = 50 mm, see Figure 7.14). The observed shapes differed noticeably from case to case suggesting that in this region the combined effects of both swirl and equivalence ratios have significant impact.
3. At heights between 40 and 60 mm, the shapes of the PDFs were very similar between combustion cases of the same equivalence ratio past a given radial distance, which varied with height (e.g., r = 9 mm at z = 40, r = 18 mm at z = 50). This suggests that in this region the equivalence ratio controls the nature of the PDFs more than the swirl level does.
4. At heights above 70 mm, the radial profiles of PDF shapes differed from case to case as well (see Figures 7.13 and 7.14) suggesting that in this region the combined effects of both swirl and equivalence ratio have significant impact.

Figure 7.17 shows the location of the bimodal distributions for the four combustion cases. On the centerline, the bimodal distributions occur at the lowest height (50 mm) in the 3 most stable cases, and at 60 mm for the least stable case (MS65). The bimodal distributions occur along a diagonal from the bottom of the burner and outward radially, possibly following a mixing layer along the inlet stream. The lowest heights where bimodal distributions are observed appear to be a function of the inlet swirl number. The two most stable cases, HS65 and HS80, show bimodal distributions at a height of 5 mm, whereas the bimodal distributions are not observed below 10 mm for the MS cases. The

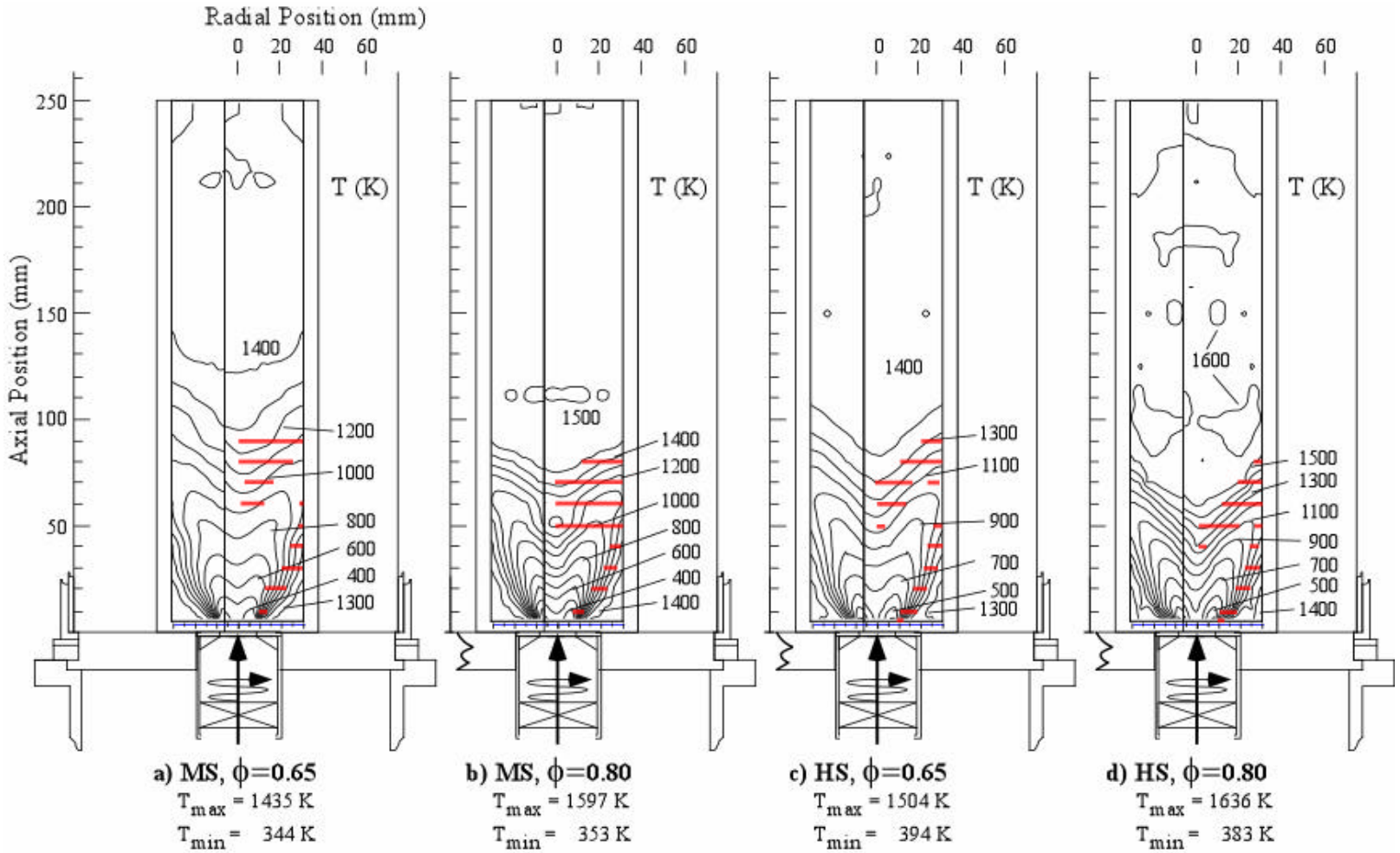

Figure 7.17. Location of the bimodal distribution PDFs for all combustion cases. Red line highlights locations where the bimodal distributions occur. PDFs were generated only from the centerline to the wall

highest height with bimodal distributions seems to be a function of ϕ, occurring at 90 mm for the MS65 and HS65 cases, while occurring at 80 mm for the MS80 and HS80 cases. It is interesting that the MS80 case is the only condition showing bimodal distributions across the whole radius between z= 50 and 70 mm.

These observations indicate that bimodal distributions appear at lower heights in more stable flames, both in the central recirculation zone and in the side recirculation zone (recall Figure 2.5 in chapter 2, section 6). This is consistent with the idea that the earlier (i.e., lower in height) the hot gases mix with the fresh stream, the more stable the flame will be.

In conclusion, the study of the gas temperature PDFs has revealed certain patterns in the complex nature of the mixing and reaction processes that take place in the LSGTC. It is expected that this information will serve as the basis for future modeling studies in order to explain the turbulent behavior of premixed combustion in systems similar to the LSGTC. For a modeling theory to be successful, it should be able to identify both the factors and mechanisms that determine what type of statistical variation will be found at a given location in the combustor.

7.2 Comparison of CARS, PLIF and LDA data

The data collected in this work, together with Murray's LDA data (1998) and Hedman and co-worker's PLIF OH data (2000a) present a great potential for fertile research. LDA data show how the gas velocity varies throughout the combustor, giving insights on how the inlet and reacted gases are transported into different areas of the flame. PLIF OH data show qualitative concentrations of OH radical which is an important intermediate during the combustion of natural gas. PLIF OH data also give

insights on whether the combustion has yet to start, has proceeded partially, or has been completed at different locations throughout the flame.

In this section, an analysis is made by comparing CARS, LDA and PLIF OH data for the most stable combustion case in this research, namely HS80, based solely on experimental data. It must be remembered that these data were collected at different occasions (about two years apart) and therefore the compositions of the natural gas used in each experiment differed slightly. Ideally, it would be better to collect all three sets of data simultaneously, or, if not possible, at least during the same time frame. A more detailed analysis of the four data sets is beyond the scope of this dissertation.

The analysis to be presented below on the combined CARS, LDA and PLIF OH data will rely on the LSGTC flow features described by Hedman, and co-workers (2002b). Specifically, reference will be made to the flame vortex and the central and side recirculation zones (CRZ and SRZ, respectively), as described in chapter 2, section 6 (see Figure 2.5).

Figure 7.18 presents the false color image of the mean temperature data for the HS80 case found in Figure 7.4. A vector plot of the average axial and radial velocities from Murray's LDA data (Murray, 1998) is superimposed over the CARS gas temperature data. The velocity vectors show:

1. The axial/radial velocity components of the vortex described by the strong inlet flow moving diagonally upwards (tangential component not shown).
2. The CRZ (the flow inside the vortex center moving down towards the inlet).
3. The SRZ (the flow outside the vortex at the bottom corners moving towards the centerline).

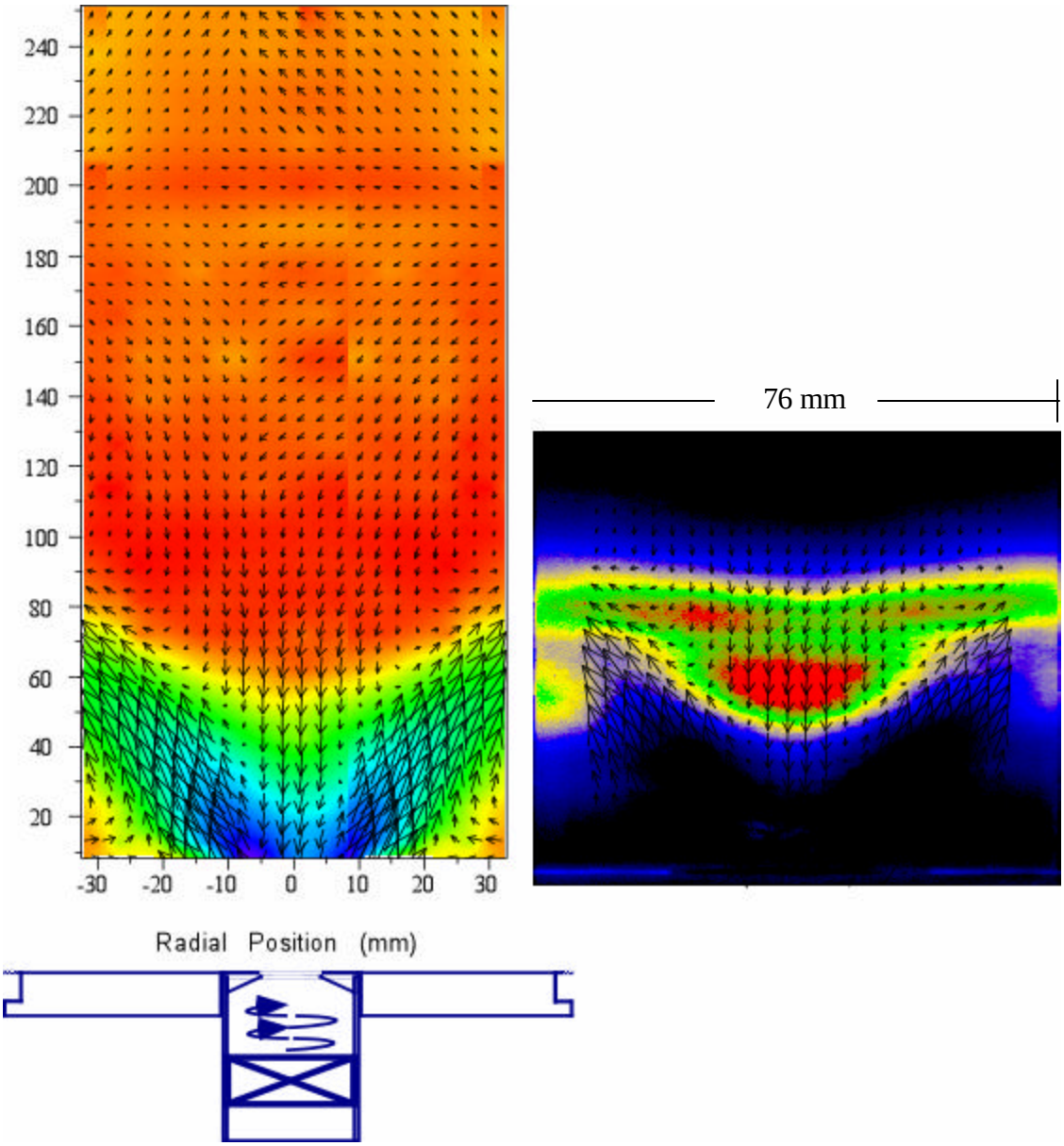

Figure 7.18. Averaged axial/radial velocity vector plot superimposed on the averaged CARS gas temperature map (left) and the average PLIF OH intensity image (right) for the HS80 case. The images are in the same scale and are aligned in height.

On the right side of Figure 7.18, a false color image of mean OH intensity for the same combustion case is also included, as measured by Hedman, et al. (2002a). The PLIF OH measurements are qualitative, with the red color representing the highest OH

concentrations, the blue color the lowest OH concentrations, and the black color no existence of OH. The velocity vectors are superimposed on the map of mean OH intensity as well. The size of the vector arrows indicates the relative value of the velocity—the larger the arrow, the larger the velocity.

The PLIF measurements did not yield quantitative values of OH concentration; however, the intensity is nearly proportional to concentration, with the red color denoting high concentration. The peak OH intensity is observed in the CRZ at a location centered at about z = 60 mm. The OH structure shows "side arms" right next to the wall, which seem to be curled down and pointing towards the center.

Another important feature of the OH map is the blue "halo", i.e., the low concentration region that surrounds the structure. These low concentration regions could be interpreted in two different ways: either the OH is almost consumed, or it is beginning to be formed. Determining what is actually happening at the top and bottom parts of the halo in this regard warrants further research. It seems reasonable to assume that the top halo is due to extinction of OH, while the bottom halo is due to the ignition started by the mixing of the fresh inlet stream with the hot gases from both the central and the side recirculation zones. In addition, the combined LDA and PLIF data appear to show that the central recirculation zone is transporting the intermediate species such as the OH radical down into the core of the flame vortex.

The idea that the bottom halo is an indicator of ignition seems to be supported by data from the CARS, LDA and OH measurements. Figure 7.19 shows four instantaneous OH images. The A-008 image is very similar to the averaged image (Figure 7.18), while image B-126 shows an instance when the highest intensities occurred throughout the

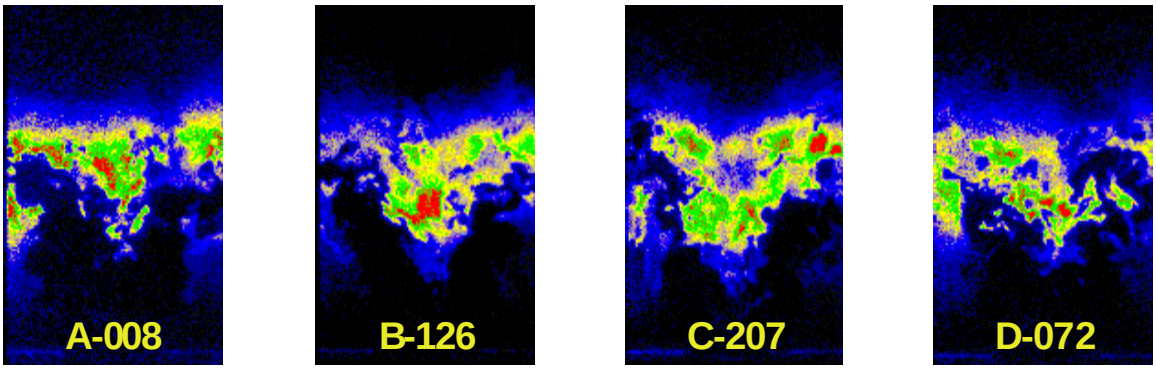

Figure 7.19. Samples of instantaneous OH PLIF images for the HS80 case (adapted from Hedman, et al., 2002a).

flame. C-207 shows an instance when the lowest intensities occurred throughout the flame, and D-072 was a rarely observed shape. Comparison of the averaged and instantaneous images once more reveals the loss of detail due to averaging. The averaged OH picture shows no signs of OH below the vortex center in places where temperatures are already 900 K. However, instantaneous PLIF OH images do show that at times OH is actually found in these areas, albeit in lower concentrations and not as frequently as in the center and arms of the vortex.

The combined CARS and LDA data show that the low temperature trough occurs in the region of strong inlet velocities. The temperature increase in the main flow direction in this trough is the result of the combined effect of the convergence of hot, reacted gases with the fresh inlet stream and the ensuing combustion. In addition, the measurements of CARS temperature fluctuations showed the most intense fluctuations near the inlet at the bottom of the combustor (see Figures 7.7 through 7.10), which would contribute to igniting the fresh inlet mixture.

Another interesting observation based on Figure 7.18 is that the hot gases in the central recirculation zone seem to cool down as they travel down the center of the vortex while generating OH over a short distance. This may seem odd at first, but a plausible explanation is proposed based on the following facts:

1. The temperature PDFs show a strong bimodal character in the vortex center in the neighborhood of the 50 mm height near the centerline (e.g. PDFs A and B in Figure 7.20, see Appendix C for more heights). This indicates that the gases arriving at this region at different times have a wide bimodal variation of temperature: one mode being centered at 900 K, with temperatures as low as approximately 600 K, while the other mode being centered at 1500 K with temperatures as high as approximately 1700 K.
2. The OH is found in the largest amounts in the vortex center at the 50 mm height. This is shown by Figure 7.21 where several OH PDFs are shown at various locations marked on the averaged OH image (same as Figure 7.18). Note that the PDFs labeled B, C and D (at 50, 60 and 70 mm height on the centerline, respectively) show the largest breadth of detector counts. Thus, there is a wide variation with time at these locations in the OH content from negligible to very high.
3. Although, on the average, the flow along the centerline goes downwards, there is evidence that at times the flow does go upwards and from "side to side" significantly (see discussion below).

The PDFs of the axial velocity component at three different radial positions at a height of 80 mm are shown in Figure 7.22. The vertical red line indicates where the axial

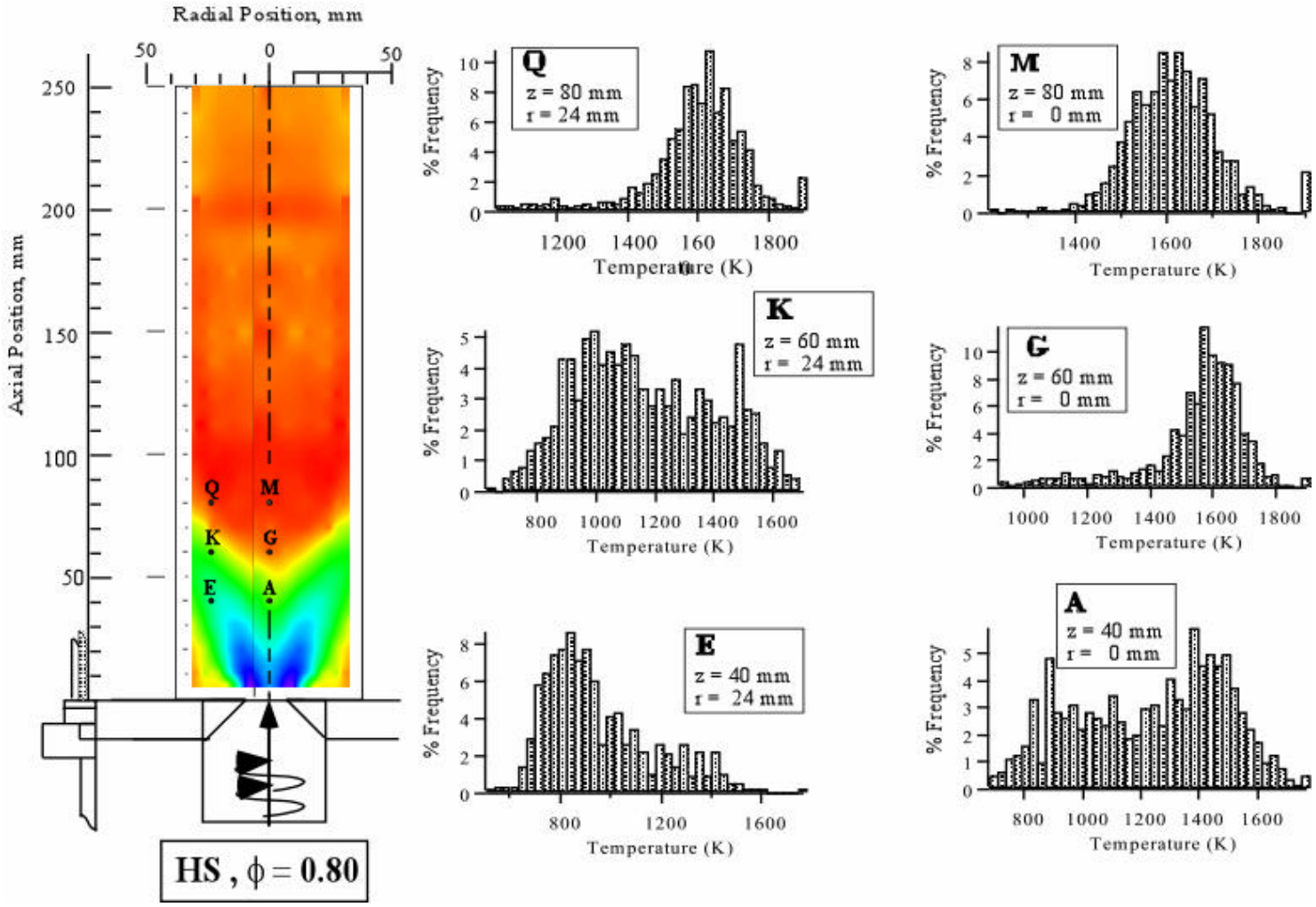

Figure 7.20. Example temperature PDFs for the HS80 case (adapted from Hedman, et al., 2002c).

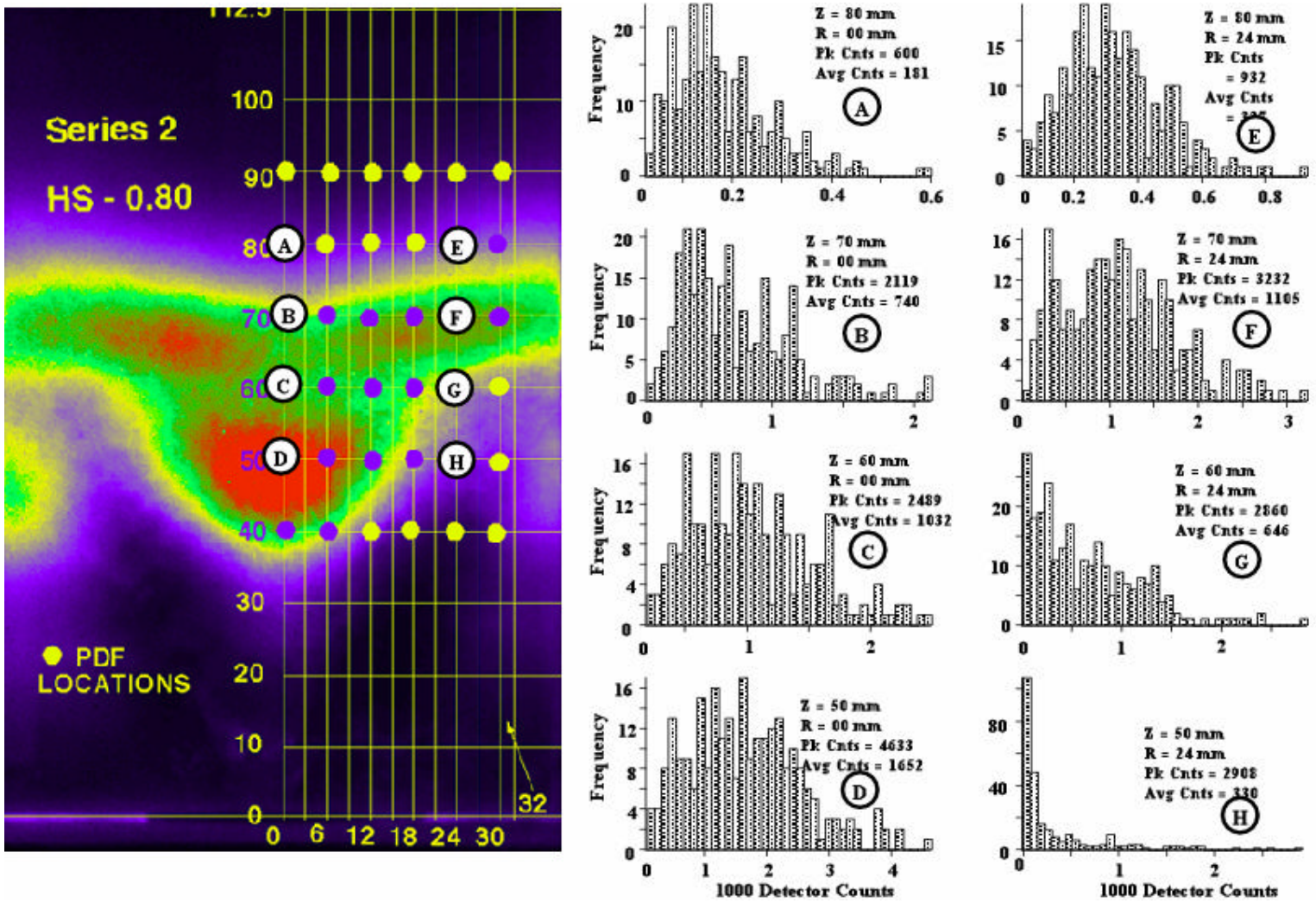

Figure 7.21. Example PDFs from OH-PLIF images for the HS80 case (adapted from Hedman, et al., 2002a).

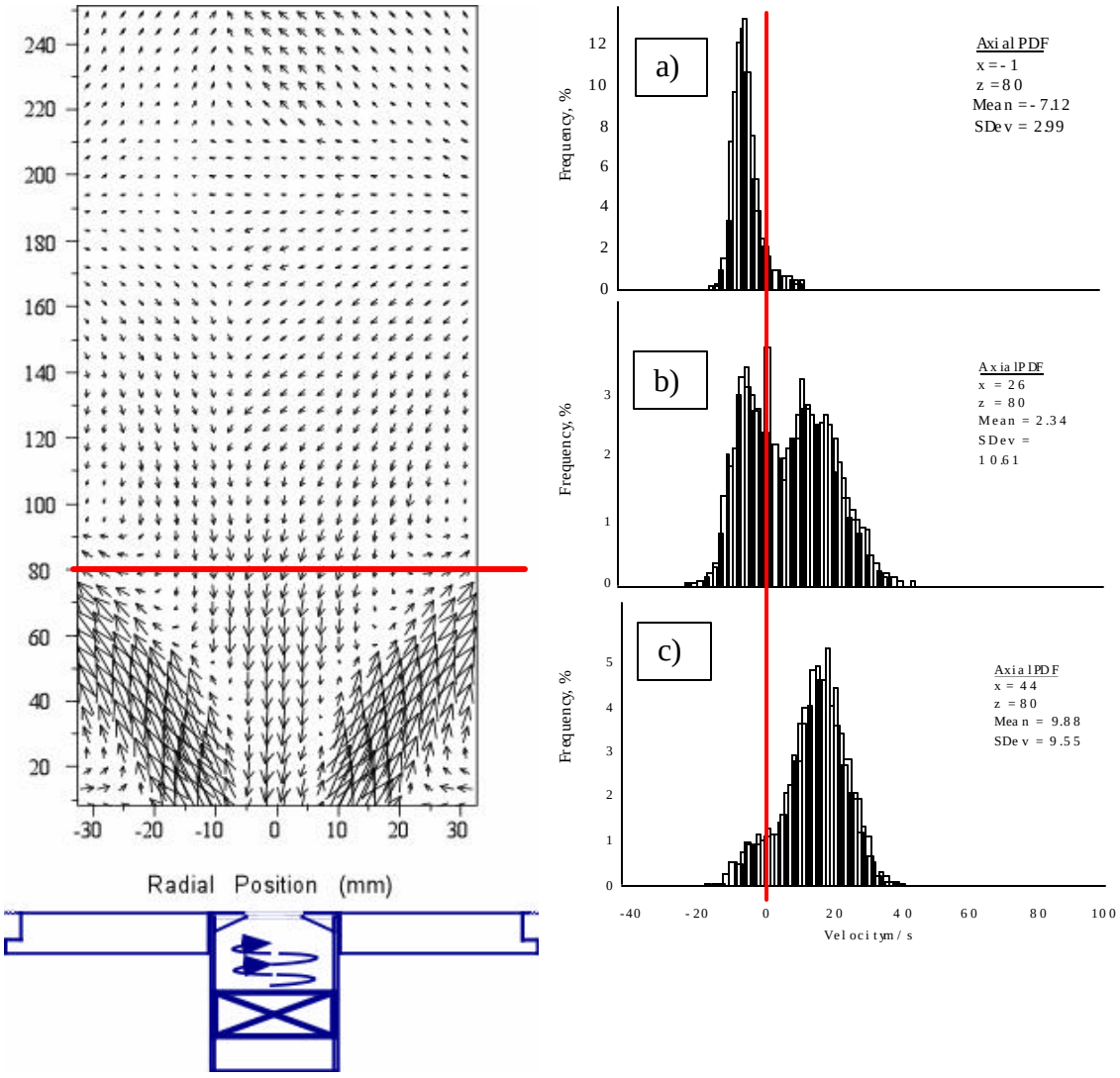

Figure 7.22. Sample PDFs of the axial velocity components for the HS80 case. LDA measurements taken from Murray (1998).

velocity equals zero for all three cases. The averaged vector plot of the combined axial and radial components is also included to visualize the location of the PDFs in question (see horizontal red line). PDF a) shows that most of the axial velocities measured at (80, -1) point towards the centerline. PDF b) shows that, of the total number of axial velocities measured at (80, 44), about two-thirds point towards the wall while the other

Table 7.3. Example LDA velocity data statistics at various locations for the HS80 case reported by Murray (1998, Appendix A, pp A-21 - 30)

		Velocity Component (m/s)					
Burner Location		**[1]Axial, v_z**		**Radial, v_r**		**[2]Tangential, v_q**	
z (mm)	r (mm)	μ	σ	μ	σ	μ	σ
10	7	-0.21	20.54	3.22	8.52	29.19	13.1
10	13	46.06	10.54	20.74	16.84	29.72	8.47
10	31	-.58	3.93	-8.66	2.84	11.19	3.71
30	2	-11.61	9.77	-0.87	7.02	(-2) 3.02	8.32
30	17	30.11	14.54	11.75	11.70	(16) 19.81	9.69
30	29	7.06	6.80	2.42	10.01	(16) 12.68	6.10
60	4	-10.33	4.45	-0.40	4.95	1.43	5.10
60	16	-1.38	10.69	2.00	6.10	5.05	6.76
60	31	17.32	10.64	12.60	7.83	11.61	6.94
80	1	-6.70	2.99	-1.70	4.07	(2) 2.85	4.05
80	16	-4.91	5.72	-0.47	4.45	(17) 3.41	4.58
80	28	3.05	9.79	5.38	5.53	(29) 5.05	5.97

1. μ is the mean, and σ is the standard deviation. Axial velocity taken from the axial/radial measurements
2. Numbers in parenthesis to the left of tangential m values are their actual radial locations

one-third point towards the centerline. PDF c) shows that most of the axial velocities measured at (80, 44) point towards the wall.

The LDA data just presented show evidence of local flow reversal at z = 80 mm, which would not have been possible to detect based on the averaged values alone. Unfortunately, LDA PDFs were reported only for the height of 80 mm. However, further evidence of local flow reversal at other flame locations can be obtained from the average and standard deviation values reported by Murray for the HS80 case (1998). Table 7.3 shows the mean and standard deviations of the three velocity components at various locations. The locations were selected around the centerline, on the inlet stream, and to the right of the inlet stream. For convenience, the coordinate pair notation (r, z) will be used. For example, (0, 50) means the location at r = 0 and z = 50.

The data along the inlet stream (e.g., (13,10) and (29, 30)) have standard deviations that are only a fraction of the size of their respective average values (e.g., 2/3 and 1/5). This means that the averaged velocities along the inlet stream are a fair representation of the direction of the flow. At either side of the inlet stream, however, the standard deviations are equal to or greater than their corresponding average value. In these cases, the average velocities do not represent the general direction of the flow since there is not really one direction for the flow.

In fact, assuming that $\pm 2*\sigma$ represents the range of values of the measured velocities, it can be concluded that the averaged velocities are hiding a large variation in the direction of the flow. For example, at (10, 7), the axial velocities are -0.21 ± 20.54 m/s. Thus, the axial velocity varied between +41 m/s (going upward) and – 41 m/s (going downwards). In the case of the radial velocity at (10, 7) the component is $+3.22 \pm 8.52$ m/s, thus the radial velocity varied between + 20 m/s (going towards the wall) and – 16 m/s (going towards the centerline). The velocity fluctuations in the tangential components also show large variations.

Thus, all the velocity components outside the inlet stream and below the complete combustion height flip their direction from time to time, as if there is a local reversal of the flow. Using the $\pm 2*\sigma$ criterion, the data show that local flow reversal also exists in the inlet stream, although not as noticeably as on its sides because here the σ values are less than their corresponding averages. The flow reversals in all the velocity components are a very strong indication of the existence of eddies in this region. Note that similar situations were found in all the LDA data throughout the flame.

The facts just listed above may indicate that the gases present at the locations in and around the vortex center have different extents of reaction at different times—sometimes closer to ignition, and at other times almost fully reacted. This would explain why the gas temperatures seem to cool off as the CRZ carries the flow down the centerline, as gases closer to the inlet would be cooler than those at higher positions would. It is proposed that this happens because the flow is carrying eddies into the center of the vortex, sometimes from the top of the flame by the CRZ and at other times from the strong inlet stream, possibly due to mixing with the SRZ. Moreover, it is possible that the greater stability displayed by the HS80 case (compared to the other cases in this work) is due to greater contributions of hot gases from the SRZ into the fresh inlet stream.

7.3 Suggestions for Future Research

The preliminary analysis of combined LDA, PLIF and CARS for the HS80 case presented in this work should be extended to the other three combustion conditions. The combined analysis may make it possible to identify a potential zone of ignition sustained by the mixing with the hot gases from both the central and side recirculation zones. Again, the differences in the composition of the natural gas used throughout the LDA, PLIF and CARS experiments should be factored in; otherwise, it would be preferable to obtain new data simultaneously or at least in the same time frame.

Modeling studies, using advanced codes (e.g., Cannon, et al., 1999), should be compared to the LDA, PLIF and CARS experiments in order to explain the turbulent behavior of the premixed combustion in systems similar to the LSGTC. A successful model should be able to identify both the factors and mechanisms that determine the type

and magnitude of the statistical variation throughout the combustor, matching as closely as possible what experiments have shown. The model should also be able to explain the roles that the central and side recirculation zones play in stabilizing the flame.

It would be interesting to pursue a chemical kinetic analysis using Lagrangian pathlines (Warren and Hedman, 1995) generated from the mean values of LDA velocities reported by Murray (1998) in conjunction with the temperature data collected in this work. These pathlines represent the trajectory followed by a hypothetical packet of premixed fuel and air. The Lagrangian path could be coupled with the CARS mean temperature data to give the temperature history of the packet. The thermal history and initial composition of the packet could then be used as input to 1-D chemical kinetic models (e.g., the Premixed code by Kee, et al., 1992a). The chemical reactions can be modeled using the CHEMKIN (Kee, et al., 1992b) subroutines with reduced kinetic mechanisms for natural gas combustion (Mallampalli, et al., 1998) developed as part of the ATS program at the Advanced Combustion Engineering Center of BYU. If further work on the CARS instrument makes it possible to extract reliable values of O_2 and CO_2 concentrations, these experimental values could be compared with modeling predictions.

It is recognized that the turbulent effects would not be explicitly included in the proposed Lagrangian analysis. This raises the following question: How closely can turbulent premixed combustion be modeled using a temperature history from averaged CARS and LDA data in a 1-D laminar premixed code? The answer either may help to create new, simple models or may warrant the use of more sophisticated ones. The outcome of this proposed analysis and the new knowledge derived from the CARS and

LDA joint analysis described above should be valuable information for both modelers and designers.

8. CONCLUSIONS AND RECOMMEDATIONS

8.1 Conclusions

The CARS instrument development from this work resulted in the following unique contributions:

1. An existing CARS instrument was modified to use a new single Stokes dual dye laser that produces simultaneously CARS spectra of N_2, CO, CO_2, and O_2. These CARS spectra yield simultaneous values for the gas temperature, derived from N_2 measurements, and concentrations of CO, CO_2, and O_2. The modified instrument requires less optical elements than dual Stokes CARS systems and may therefore be advantageous to use in circumstances where space availability is an issue.
2. New proportions of the pyromethene 650 and 597 dyes were used in order to control the power and spectral characteristics of the Stokes dye laser used to make the CARS instrument.
3. New software was developed to make it feasible to analyze the large quantities of data acquired in this work in a reasonable amount of time. A data management system was designed and implemented to automate the data acquisition and reduction process. The data management system was coupled with FMCARS, a CARS data reduction program developed in this work that uses a CARS data reduction algorithm from Sandia National Laboratories.

4. Calibration studies in a tube furnace showed that the single Stokes CARS instrument has good accuracy and acceptable precision for gas temperature measurements. The average of the CARS measured values of gas temperatures was within 5% of the thermocouple values of the tube furnace, while the variability of the CARS measurements was within ±15% of the tube furnace values.
5. Further calibration studies showed that the single Stokes instrument had limited capabilities in measuring the concentrations of O_2 and CO_2 in the concentration ranges of interest in this work.
    a. Average O_2 concentrations were about 15% less than the calibration value, but the uncertainty on the measurements was at least 30%, covering about two-thirds of the range of expected concentrations in the combustion cases of interest.
    b. Room temperature experiments showed that the instrument was simply not reliable in obtaining CO_2 concentrations.

    It is possible that these limitations of the single Stokes instrument are due to the approximations involved in the specific CARS reduction algorithm used in this work.
6. The dual dye single Stokes CARS instrument was used to obtain instantaneous gas temperature measurements for four combustion conditions in a Laboratory Scale Gas Turbine combustor (LSGTC).

The following unique contributions were made while studying the gas temperature CARS measurements obtained in the LSGTC:

1. Gas temperature measurements were obtained for four lean combustion conditions of premixed natural gas and air. Two equivalence ratios, 0.65 and 0.80, were investigated at two different swirl levels.
2. Iso-contour plots of averaged and normalized standard deviations of gas temperatures were produced based on the experimental data obtained in this work. In addition, Probability Density Function (PDF) plots were also produced based on the 1000 instantaneous measurements obtained at each sampling location.
3. It was found that flame stability in these combustion conditions increased with increasing equivalence ratio and swirl level, which brought the flame vortex closer to the inlet. The flame stability behavior observed in this work agrees with prior research. The MS65 case, having the lowest equivalence ratio and inlet swirl level, was the least stable case. On the other hand, the HS80 case, having the highest equivalence ratio and inlet swirl level, was the most stable case.
4. Although the iso-contour plots of $<T>$ and $\sigma/<T>$ vary with combustion conditions, the general shapes of the contours showed many similarities.
5. All cases exhibited a particular height where the radial temperature profiles are almost constant and the normalized standard deviations are 5% or less, possibly indicating that the combustion is complete. These data show that higher swirl tends to bring the reacting portion of the flame closer to the inlet, more so than higher fuel content.
6. Based on visual observations, profiles of $<T>$, and profiles of $\sigma/<T>$, it is therefore concluded that, for the cases studied, the swirl level has a larger influence in the stability of the flame than ϕ.

7. The normalized standard deviation plots and PDFs showed large variations in the center of the vortex of each flame, supporting the assertion made by Hedman and co-workers that the hot gases flowing down the centerline help stabilize the flame.
8. The normalized standard deviation plots also showed that the highest temperature variations are found in a region just above the injector inlet. This feature lends support to the idea that the side recirculation zone plays an important role stabilizing the flame by helping to heat up and ignite the fresh inlet stream. However, further research is recommended in order to assess to what extent the turbulent mixing from the side recirculation contributes to the stability of the flames.
9. Four types of PDF distributions were found to exist in all combustion conditions: delta, beta, normal and bimodal distributions. Beta distributions were the most prevalent in each combustion case. The locations of the bimodal distributions seem to indicate that, for the more stable flames, the bimodal distributions occur at the lowest heights in both the central recirculation zone and in the side recirculation zone. This could mean that the earlier (i.e., lower in height) the hot gases mix with the fresh stream, the more stable the flame will be. The study of the gas temperature PDFs revealed the complex nature of the mixing and reaction processes that take place in the LSGTC.
10. Additional insights regarding the flame behavior were obtained by examining the spatial variation in the shape of the PDFs for all the combustion conditions. At lower heights, near the bottom of the combustor, the swirl level seems to be the dominant factor determining the nature of the turbulent fluctuations, whereas near

the wall and around z = 50 mm, the equivalence ratio appears to dominate. For the rest of the flame, the combined effect of the equivalence ratio and swirl level seems to determine the nature of the temperature fluctuations.

11. A preliminary analysis of combined LDA, PLIF, and CARS data for the HS80 case was presented. The combined analysis made it possible to identify a potential zone of ignition, sustained by the mixing of inlet gases with the hot gases from both the central and the side recirculation zones.

8.2 Recommendations

It is recommended that a comprehensive analyses comparing CARS, LDA and PLIF OH data be performed for all combustion conditions in more detail. The differences in the composition of the natural gas used throughout the LDA, PLIF and CARS experiments should be accounted for; otherwise, it would be preferable to obtain new data simultaneously or at least in the same time frame.

Future modeling studies should accompany the experiments in order to explain the turbulent behavior of the premixed combustion in systems similar to the LSGTC. A successful model should be able to identify both the factors and mechanisms that determine the type and magnitude of the statistical variation throughout the combustor, matching as closely as possible what experimentation has shown. The model should also be able to explain the roles that the central and side recirculation zones play in stabilizing the flame.

The following recommendations are made regarding the single Stokes dual dye CARS instrument:

1. Investigate the possibility of using other dyes that would distribute the laser power in the dye profile to minimize the power wasted in spectral regions of no interest.
2. Compare the performance of the dual dye single Stokes CARS instrument with the performance of the dual Stokes CARS instrument developed by Boyack (1990).
3. Investigate whether the ability of the dual dye single Stokes CARS instrument to measure O_2 and CO_2 concentrations can be improved by using a reduction method that is more exact.

REFERENCES

Anand, M. S. and F. C. Gouldin, "Combustion Efficiency of a Premixed Continuous Flow Combustor," *Journal of Engineering for Gas Turbines and Power*, **107**, 695-705 (1985).

Anderson, T. J., G. M. Dobbs and A. C. Eckbreth, "Mobile CARS Instrument for Combustion and Plasma Diagnostics," *Applied Optics*, **25**, 4076-4085 (1986).

Armstrong, J. A., N. Bloembergen, J. Ducuing and P. S. Pershan, "Interaction between Light Waves in a Nonlinear Dielectric," *Physical Review*, **127**, (6) 1918-1939 (1962).

Bedue, R., P. Gastebois, R. Bailly, M. Pealat and J. P. Taran, "CARS Measurements in a Simulated Turbomachine Combustor," *Combustion and Flame*, **57**, 141-153 (1984).

Boyack, K. W., "A Study of Turbulent Nonpremixed Jet Flames of CO/N_2 Using Coherent Anti-Stokes Raman Spectroscopy," Ph. D. Dissertation, Department of Chemical Engineering, Brigham Young University, Provo, UT (1990).

Buschmann, A., F. Dinkelacker, T. Schafer, M. Schafer and J. Wolfrum. Measurement of the Instantaneous Detailed Flame Structure in Turbulent Premixed Combustion. Twenty-Sixth Symposium (International) on Combustion, Univ. of California, Irvine, The Combustion Institute, **6**, 437-445 (1996).

Cannon, S. M., B. S. Brewster and L. D. Smoot, "PDF Modeling of Lean Premixed Combustion Using In Situ Tabulated Chemistry," *Combustion and Flame*, **119**, 233-252 (1999).

Cohen, H., C. F. C. Rogers and H. I. H. Saravanamuttoo. Gas Turbine Theory. Longman Group Limited, London (1996).

Druet, S. A. J. and J. P. E. Taran, "CARS Spectroscopy," *Progress in Quantum Electrodynamics*, **7**, 1-72 (1981).

Eckbreth, A. C. Laser Diagnostics for Combustion Temperature and Species. Gordon and Breach Publishers (1996).

Ecob, D. J., M. B. Bouns and T. I. Mina, *Using Natural Gas in Industrial Gas Turbines*, Using Natural Gas in Engines, London, Mechanical Engineering Publications (1996).

Eesley, G. L. Coherent Raman Spectroscopy. Pergamon Press, New York (1981).

El Banhawy, Y., S. Sivasegaram and J. H. Whitelaw, "Premixed, Turbulent Combustion of a Sudden-Expansion Flow," *Combustion and Flame*, **50**, 153-165 (1983).

Farrow, R., Personal Communication (1995).

Gupta, A. K., D. G. Lilley and N. Syred. Swirl Flows. Abacus Press, Malta (1984).

Hall, R. J. and L. R. Boedeker, "CARS Thermometry in Fuel-rich Combustion Zones," *Applied Optics*, **23**, (9), 1340-1346 (1984).

Haslam, J. K., Personal Communication (1996).

Haslam, J. K. and P. O. Hedman. The Use of Two Pyromethene Dyes in a Single Stokes Dye Laser to Make CARS Temperature and Multiple Species (CO, CO_2, O_2, N_2) Concentration Measurements. Fall Meeting of WSS/CI, 96F-086, Los Angeles, CA (1996).

Hay, N. E., Ed. Guide to New Natural Gas Utilization Technologies, The Fairmont Press, Inc. (1985).

Hedman, P. O., Personal Communication (1998).

Hedman, P. O., Personal Communication (2001).

Hedman, P. O., T. H. Fletcher, S. G. Graham, G. W. Timothy, D. V. Flores and J. K. Haslam. Observations of Flame Behavior in a Laboratory-Scale Pre-Mixed Natural Gas/Air Gas Turbine Combustor from PLIF Measurements of OH. ASME International Gas Turbine and Aeroengine Congress and Exposition, Amsterdam, Netherlands, International Gas Turbine Institute (2002a).

Hedman, P. O., R. L. Murray and T. H. Fletcher. Observations of Flame Behavior in a Laboratory-Scale Pre-mixed Natural Gas/Air Gas Turbine Combustor from LDA Velocity Measurements. ASME International Gas Turbine and Aeroengine Congress and Exposition, Amsterdam, The Netherlands (2002b).

Hedman, P. O., R. L. Murray and T. H. Fletcher. Observations of Flame Behavior in a Laboratory-Scale Pre-mixed Natural Gas/Air Gas Turbine Combustor from CARS Temperature Measurements. ASME International Gas Turbine and Aeroengine Congress and Exposition, Amsterdam, The Netherlands (2002c).

Hedman, P. O., L. D. Smoot, B. S. Brewster and T. H. Fletcher, "Combustion Modeling in Advanced Gas Turbine Systems," *Final Report*, Subcontract No. 93-01-SR014 (1998).

Hedman, P. O., G. J. Sturgess, D. L. Warren, L. P. Goss and D. T. Shouse, "Observations of Flame Behavior from a Practical Fuel Injector Using Gaseous Fuel in a

Technology Combustor," *Journal of Engineering for Gas Turbines and Power*, **117**, 441-452 (1995).

Kataoka, H., S. Maeda and C. Hirose, "Effect of Laser Linewidth on the Coherent Anti-Stokes Raman Spectroscopy Spectral Profile," *Applied Spectroscopy*, **36**, 508-512 (1982).

Kee, R. J., J. F. Grcar, M. D. Smooke and J. A. Miller, "A Fortran Program for Modeling Steady Laminar One-Dimensional Premixed Flames," SAND85-8240.UC-401 (1992a).

Kee, R. J., F. M. Rupley and J. A. Miller, "Chemkin-II: A Fortran Chemical Kinetics Package for the Analysis of Gas-Phase Chemical Kinetics," SAND89-8009B.UC706 (1992b).

Lefebvre, A. W. Gas Turbine Combustion. Hemisphere Publishing Corporation, New York (1983).

Lewis, B. and G. von Elbe, Combustion, flames and Explosions of Gases, Third Edition, Academic Press, San Diego, (1987).

Magre, P., P. Moreau, G. Collin, R. Borghi and M. Pealat, "Further Studies by CARS of Premixed Turbulent Combustion in a High Velocity Flow," *Combustion and Flame*, **71**, 147-168 (1988).

Mallampalli, H. P., T. H. Fletcher and J. Y. Chen, "Evaluation of CH4/NOx Reduced Mechanisms Used for Modeling Lean Premixed Turbulent Combustion of Natural Gas," *ASME Journal of Engineering for Gas Turbines and Power*, **120**, 703-712 (1998).

Melvin, A. Natural Gas: Basic Science and Technology. British Gas, London (1988).

Moya, F., S. A. J. Druet, M. Pealat and J. P. E. Taran, "Gas Spectroscopy and Temperature Measurement by Coherent Raman Anti-Stokes Scattering," *Optics Communications*, **13**, 169-174 (1975).

Murray, R. L., "Laser Doppler Anemometry Measurements in a Turbulent, Premixed, Natural Gas/Air Combustor," M. S. Thesis, Department of Chemical Engineering, Brigham Young University, Provo (1998).

Nandula, S. P., R. W. Pritz, R. S. Barlow and G. J. Fiechtner. Rayleigh/Raman/LIF Measurements in a Turbulent Lean Premixed Combustor. 34th Aerospace Sciences Meeting and Exhibit, Reno, NV, American Institute of Aeronautics and Astronautics (1996).

Nguyen, Q. V., B. L. Edgar, R. W. Dibble and A. Gulati, "Experimental and Numerical Comparison of Extractive and In Situ Laser Measurements of Non-Equilibrium

Carbon Monoxide in Lean-Premixed Natural Gas Combustion," *Combustion and Flame*, **100**, 395-406 (1995).

Nicoletti, P. A., "METCEC - User's Manual," Final Report for DOE Contract No. DE-AC21-85MC21353, Morgantown Energy Technology Center (April, 1986).

Palmer, R. E., "The CARSFT Computer Code for Calculating Coherent Anti-Stokes Raman Spectra: User and Programmer Information," Sandia Report SAND89-8206 (1989).

Pan, J. C. and D. R. Ballal. Chemistry and Turbulence Effects in Bluff-Body Stabilized Flames. 30th Aerospace Sciences Meeting & Exhibit, AIAA 92-0071, Reno, NV, American Institute of Aeronautics and Astronautics (1992).

Philips, C. G., "Laser Doppler Anemometry (LDA) Measurements in a Turbulent Ethanol Flame," M. S. Thesis, Department of Mechanical Engineering, Brigham Young University, Provo (1998).

Pyper, D. K., "The Study of Flame Stability Near Lean Blow Out in Non-Premixed Non-Swirl and Swirl Burners and the Design of a Research Combustor Facility," M. S. Thesis, Department of Mechanical Engineering, Brigham Young University, Provo (1994).

Regnier, P. R., F. Moya and J. P. E. Taran, "Gas Concentration by Coherent Raman Anti-Stokes Scattering," *AIAA J.*, **12**, 826-831 (1974).

Regnier, P. R. and J. P. Taran, "On the Possibility of Measuring Gas Concentrations by Stimulated Anti-Stokes Scattering," *Applied Physics Letters*, **23**, 240-242 (1973).

Roberts, W. L., J. F. Driscoll, M. C. Drake and L. P. Goss, "Images of the Quenching of Flame by a Vortex-To Quantify Regimes of Turbulent Combustion," *Combustion and Flame*, **94**, 58-69 (1993).

Rudd, M. J., "A New Theoretical Model for the Laser Dopplermeter," *Journal of Physics E*, **2**, (55) (1969).

Schmidt, S. E., "Laser Doppler Anemometry (LDA) Measurements in a Turbulent Premixed Natural Gas Flame," M. S. Thesis, Department of Chemical Engineering, Brigham Young University, Provo (1995).

Schmidt, S. E. and P. O. Hedman, "CARS Temperature and LDA Velocity Measurements in a Turbulent Swirling, Premixed Propane/Air Fueled Model Gas Turbine Combustor," 95-GT-64 (1995).

Snelling, D. R., G. G. Smallwood and T. Parameswaran, "Effect of detector nonlinearity and image persistence on CARS derived temperatures," *Applied Optics*, **28**, (15) 3233-3241 (1989).

Snelling, D. R., G. J. Smallwood, R. A. Sawchuk and T. Parameswaran, "Precision of Multiplex CARS Temperatures Using Both Single-Mode and Multimode Pump Lasers," *Applied Optics*, **26**, 99-110 (1987).

Sturgess, G. J., D. G. Sloan, A. L. Lesmerises, S. P. Henneghan and D. R. Ballal, "Design and Development of a Research Combustor for Lean Blow-Out Studies," *ASME Journal of Engineering for Gas Turbines and Power*, **114**, 13-19 (1992).

Switzer, G. L., L. P. Goss, W. M. Roquemore, R. P. Bradley, P. W. Schreiber and W. B. Roh, "Application of CARS to Simulated Practical Combustion Systems," *Journal of Energy*, **4**, 209-215 (1982).

Teets, R. E., "Accurate Convolutions of Coherent Anti-Stokes Raman Spectra," *Optics Letters*, **9**, 226-228 (1984).

Tolles, W. M. and A. B. Harvey, *Introduction to Nonlinear Phenomena*, Chemical Applications of Nonlinear Raman Spectroscopy. A. B. Harvey, Washington, D. C., Academic Press, (1981).

Tolles, W. M., J. W. Nibler, J. R. McDonald and A. B. Harvey, "A Review of the Theory and Application of Coherent Anti-Stokes Raman Spectroscopy (CARS)," *Applied Spectroscopy*, **31**, (4) 253-271 (1977).

Warren, D. L., "Combustion Studies of a Swirled, Non-Premixed Flame Using Advanced Diagnostics," M. S. Thesis, Department of Mechanical Engineering, Brigham Young University, Provo (1994).

Warren, D. L. and P. O. Hedman, "Differential Mass and Energy Balances in the Flame Zone from a Practical Fuel Injector in a Technology Combustor," *Transactions of the ASME, 95-GT112* (1995).

Whiting, E. E., "An Empirical Approximation to the Voigt Profile," *Journal of Quantitative Spectroscopy and Radiative Transfer*, **8**, 1379-1384 (1968).

Yeh, Y. and H. Z. Cummins, "Localized Fluid Flow Measurements with an He-Ne Laser Spectrometer," *Applied Physics Letters*, **4**, 176-178 (1964).

Yuratich, M. A., "Effects of Laser Linewidth on Coherent Anti-Stokes Raman Spectroscopy," *Journal of Molecular Physics*, **38**, 625-655 (1979).

Zhu, J. Y., T. Tsuruda, W. A. Sowa and G. S. Samuelsen, "Coherent Anti-Stokes Raman Scattering (CARS) Thermometry in a Model Gas Turbine Can Combustor," *Journal of Engineering for Gas Turbines and Power*, **115**, 515-521 (1993).